SINGLE FIBER BI-DIRECTIONAL OE LINKS USING 3D STACKED THIN FILM EMITTERS AND DETECTORS

A Thesis
Presented to
The Academic Faculty

by

Demetris Lemarcus Geddis

In Partial Fulfillment
of the Requirements for the Degree
Doctor of Philosophy in Electrical and Computer Engineering

Georgia Institute of Technology
November 2003

Copyright © 2003 by Demetris L. Geddis

SINGLE FIBER BI-DIRECTIONAL OE LINKS USING 3D STACKED THIN FILM EMITTERS AND DETECTORS

Approved by:

Nan M. Jokerst, Chairperson

Gary S. May

Stephen E. Ralph

Gee-Kung Chang

Donald C. O'Shea

Date Approved: 11/3/03

This dissertation is dedicated to God who blessed me with the opportunity, motivation, and perseverance, to my wife who kept encouraging me, and to my parents and grandparents who believed in me.

ACKNOWLEDGEMENTS

I would like to thank my thesis advisor, Dr. Nan Marie Jokerst for her support, guidance, and persistence for excellence throughout my graduate school experience. I would also like to acknowledge Dr. Gary May, Dr. Stephen Ralph, Dr. Gee-Kung Chang, and Dr. Donald O'Shea for serving on my Ph.D. examination committee.

I would like to thank my wife, parents, and Fulfillment hour classmates for their prayers, encouragement, and support during these five years. I would also like to thank my brother and sisters for always believing in me and for keeping me motivated.

I must acknowledge my group members for all of the good times and good discussions. Finally, I would like to thank Dr. Brooke's research group and the MIRC cleanroom staff for their help and support.

TABLE OF CONTENTS

ACKNOWLEDGEMENTS IV

TABLE OF CONTENTS V

LIST OF TABLES VII

LIST OF FIGURES VIII

SUMMARY XI

CHAPTER 1 1

INTRODUCTION 1

1.1 PROBLEM DEFINITION 1
Platform 3
1.2 DISSERTATION OUTLINE 6

CHAPTER 2 8

BACKGROUND 8

2.1 LITERATURE REVIEW 8
2.1.1 Biconical Tapered Coupler 8
2.1.2 Bi-functional LED 9
2.1.3 Two p-n Junction Device 13
2.1.4 Bi-functional Laser 14
2.1.5 Photonic Integrated Circuit 15
2.1.6 Bi-functional VCSEL 19
2.1.7 Co-located Emitter and Detector 21
2.2 3D STACKED DEVICE PHYSICS 23
2.2.1 Junctions 23
2.2.1.1 p-n Junctions 23
2.2.1.2 Metal-Semiconductor Junction 26
2.2.2 Light Emitters 28
2.2.2.1 Light Emitting Diodes 28
2.2.2.2 Vertical Cavity Surface Emitting Lasers 34
2.2.2.3 Resonant Cavity Enhanced Light Emitting Diodes 38
2.2.3 Photodetectors 41
2.2.3.1 PIN Photodetectors 41
2.2.3.2 Metal-Semiconductor-Metal Photodetectors 44
2.3 THIN FILM FABRICATION AND INTEGRATION TECHNIQUES 59
2.3.1 Hybrid Integration Techniques 60
2.3.2 ELO Integration Technique 62
2.3.3 Appliqué Integration Technique 63
2.3.4 Fluidic Assembly Integration Technique 64

CHAPTER 3 65

FABRICATION AND INTEGRATION 65

3.1 SiO_2 COATED SILICON INTEGRATION 65
3.1.1 Thin Film GaAs RCE LED Fabrication and Integration 65
3.1.2 Thin Film I-MSM Photodetector Fabrication and Integration 67
3.2 INTEGRATION ONTO CMOS CIRCUITS 70
3.2.1 Integration of RCE LEDs Onto CMOS Circuits 70
3.2.2 Integration of I-MSM PDs onto CMOS Circuits 72
3.3 3D STACKED THIN FILM INTEGRATION 74
3.3.1 3D Stacked Thin film I-MSM PD/RCE LED on Silicon 74
3.3.2 Measurement Setup For 3D Stacked Device Tests 76
3.3.3 Square 3D Stack Device: GaAs LED on top of GaAs I-MSM PD 79
3.3.4 Circular 3D Stack Device: GaAs LED/GaAs I-MSM PD 82
3.3.5 3D Stacked Device: GaAs LED Stacked on Top of InGaAs I-MSM PD 86
3.4 3D STACKED THIN FILM I-MSM PD/RCE LED ON CMOS CIRCUIT 91
3.4.1 Integration Process for 3D Stacked Emitters/Detectors on CMOS Circuits 95
3.4.2 Stacked Device Circuit Testboard 98
3.4.3 3D Stacked Device Circuit Measurement Setup and Results 100
CHAPTER 4 **106**
THEORETICAL CALCULATIONS OF ALIGNMENT TOLERANCE USING GEOMETRICAL OPTICS **106**
4.1 LED LONGITUDINAL ALIGNMENT TOLERANCE 107
4.2 STACKED I-MSM PD LONGITUDINAL ALIGNMENT TOLERANCE 110
4.3 LED LATERAL ALIGNMENT TOLERANCE 113
4.4 STACKED I-MSM PD LATERAL ALIGNMENT TOLERANCE 118
CHAPTER 5 **123**
THEORY VERSUS EXPERIMENT **123**
CHAPTER 6 **130**
CONCLUSION AND RECOMMENDATIONS **130**

LIST OF TABLES

Table 1: Optical communication in different non-telecommunications platforms [6] 3

Table 2: Integration Methods 61

LIST OF FIGURES

Figure 1: Biconical Coupler [7]. 9
Figure 2: Surface Emitting LED [15]. 10
Figure 3: Burrus LED [15]....... 11
Figure 4: Structure with two PN junctions [11]....... 13
Figure 5: Edge Emitting Laser [18]. 14
Figure 6: Schematic structure of PIC [12]. 16
Figure 7: Monolithically integrated LED-amplifier [13]....... 18
Figure 8: Schematic cross section of a VCSEL [10]. 20
Figure 9: Schematic of bipolar junction phototransistor with integrated LED [14]. 21
Figure 10: 3D stacked thin film device....... 22
Figure 11: (a) Separate p and n type semiconductors and their band diagrams, and (b) formation of depletion region when materials are joined together and corresponding contact potential and energy band diagram [19]. 24
Figure 12: Effects of bias at a p-n junction on depletion width [19]. 25
Figure 13: LED coupling into a step-index multimode fiber [22]. 31
Figure 14: PIN photodetector with energy band diagram [9]. 41
Figure 15: Metal-Semiconductor-Metal Photodetector. 45
Figure 16: Equilibrium band diagram of MSM PD [56]. 45
Figure 17: Band diagram and electric field plot for an MSM PD at (a) reach through voltage, (b) flat band voltage, and (c) over flat band voltage [56]. 46
Figure 18: MSM PD capacitance versus gap size....... 51
Figure 19: PIN PD capacitance versus intrinsic region thickness. 51
Figure 20: Capacitance comparison....... 52
Figure 21: 200 μm diameter MSM PD RC and transit time using a 50 ohm load. 53
Figure 22: 150μm diameter MSM PD RC and transit time using a 50 ohm load. 54
Figure 23: 120 μm diameter MSM PD RC and transit time using a 50 ohm load. 55
Figure 24: Frequency response of photodetectors. 56
Figure 25: LED thin-film integration process....... 66
Figure 26: I-MSM PD thin film integration process....... 68

Figure 27: Thin film GaAs I-MSM PD integrated onto SiO_2 -coated silicon. 69
Figure 28: RCE LED integrated onto a CMOS circuit. 71
Figure 29: LI curve for 50 μm RCE LED. 71
Figure 30: I-MSM PD integrated onto a CMOS circuit. 72
Figure 31: Eye diagram of I-MSM PD receiver operating at 1 Gbps. 73
Figure 32: 3D Stacked thin film process. 75
Figure 33: I-MSM PD DC measurement setup. 77
Figure 34: RCE LED LI measurement setup. 78
Figure 35: Measured currents for a square I-MSM PD. 80
Figure 36: LI curve for a square LED. 80
Figure 37: Top view of a square thin film 3D stacked device. 81
Figure 38: (a) MSM PD, (b) circular thin film 3D stack device, close-up view, and (c) 3D stacked device, showing probe pads. 84
Figure 39: Current measurements for circular 3D stack. 85
Figure 40: LI curve for circular 3D stack. 85
Figure 41: Top view of 3D GaAs/InGaAs stacked structure. 88
Figure 42: Dark current measurements before and after stacking. 88
Figure 43: Photocurrent versus longitudinal displacement of fiber from the 3D LED/PD stack. 89
Figure 44: LI curve of mixed stacked LED. 90
Figure 45: Silicon CMOS transceiver circuit. 92
Figure 46: Structure of receiver and subcomponents [89]. 93
Figure 47: Differential emitter driver [90]. 94
Figure 48: 3D stacked thin film process for silicon CMOS circuit integration. 96
Figure 49: 3D Stacked GaAs RCE LED/InGaAs I-MSM PD on silicon CMOS circuitry. 97
Figure 50: Closer view of RCE LED/PD in Figure 49. 97
Figure 51: a) Picture of circuit testboard and b) schematic. 98
Figure 52: Circuit photo with wirebonding diagram. 99
Figure 53: Integrated circuit photo with wirebonds. 99
Figure 54: I-MSM photoreceiver speed measurement experimental setup. 101

Figure 55: RCE LED optical transmitter speed measurement experimental setup. 102
Figure 56: I-MSM photoreceiver output signal at 1Gbps. 103
Figure 57: I-MSM photoreceiver eye diagram at 1Gbps. 103
Figure 58: RCE LED optical transmitter signal at 40 Mbps. 104
Figure 59: RCE LED optical transmitter eye-diagram at 40 Mbps. 104
Figure 60: RCE LED spectral output. 105
Figure 61: Schematic of RCE LED and fiber 108
Figure 62: Normalized efficiency versus longitudinal displacement. 109
Figure 63: Schematic of LED shadowed I-MSM PD and fiber 110
Figure 64: Top View of LED 112
Figure 65: I-MSM PD photocurrent versus longitudinal displacement. 112
Figure 66: Lateral displacement between LED and fiber. 113
Figure 67: Diagram used to illustrate the area of a sector. 114
Figure 68: Triangle from Figure 66 115
Figure 69: LED normalized coupling efficiency versus lateral displacement 117
Figure 70: I-MSM PD lateral alignment tolerance in a) region 1, b) region 2, c) region 3, d) region 4. 118
Figure 71: I-MSM PD lateral displacement in region 4. 120
Figure 72: I-MSM PD photocurrent versus lateral displacement 122
Figure 73: Fiber output a) without mode scrambler and b) with mode scrambler 124
Figure 74: I-MSM PD longitudinal theory versus experiment 126
Figure 75: I-MSM PD lateral theory versus experiment 126
Figure 76: LED longitudinal theory versus experiment. 128
Figure 77: LED lateral theory versus experiment. 128
Figure 78: Longitudinal theory versus experiment 129

SUMMARY

The demand for higher bandwidth has created a need for fiber optics in a wide variety of commercial, industrial, and military applications, such as Fiber-to-the-Home, In-Flight entertainment systems, and tactical communication systems. For bi-directional communications, some of these fiber optic communication systems have used two optical cables. To simplify the network and reduce costs, it is advantageous to provide bi-directional communications over a single fiber. For example, in military and aerospace applications the reduction in the number of cables would reduce the weight, thereby, reducing the fuel costs.

As the demand for single fiber bi-directional optical communication continues to increase, there will be an increasing demand for affordable optical network units (ONUs). The main component of ONUs is the optoelectronic transceiver, and the cost of the ONU is critical. To better understand the challenges in designing affordable ONUs, this research investigated previous work aimed at building optoelectronic transceivers for short haul bi-directional single fiber optical links.

To provide a more integrated, compact, higher performance, alignment tolerant alternative to previous solutions, the fabrication of thin film LEDs and MSM PDs, and also the development of a process for stacking the thin film devices onto host substrates such as SiO_2 coated silicon and silicon CMOS circuits to form a optoelectronic transceiver, were demonstrated.

CHAPTER 1

INTRODUCTION

1.1 Problem Definition

Traditionally, bi-directional optical communication has been carried out using two optical cables with an emitter/detector pair at the ends of the link. This architecture allows for full duplex operation with the incoming signal propagating on one cable and the outgoing signal on the other. However, in some optical communication applications such as optical data distribution systems, fiber-to-the-curb/home/building/desktop (FTTX), and in military and aerospace fiber applications (MAFA), it would be advantageous to provide bi-directional communication using a single optical fiber. Most network architectures for FTTX, such as asynchronous transfer mode passive optical network (APON) and Ethernet passive optical network (EPON) support single fiber bi-directional communication because it reduces the amount of fiber, therefore, reducing the cost of each link [1], [2], [3], [4]. Moreover, in MAFA systems the reduction in the number of cables reduces the weight, thereby, reducing the fuel cost [5], [6].

The telecommunications backbone has experienced considerable growth over the last 10 years. However, little has changed in the access network. The incredible growth of Internet traffic has highlighted the aggravating lag of access network capacity, which has made the 'last mile' the bottleneck between high capacity local area networks and the backbone network [1]. In response to the demands for Internet services, telephone companies have deployed digital subscriber line (DSL) technology. DSL utilizes the same twisted pair as telephone lines, but requires a DSL modem at the customer's premise and a digital subscriber line access multiplexer (DSLAM) in the central office

[1]. With DSL, subscribers can reach speeds in the range of 128 kb/s to 1.5 Mb/s. Cable television providers responded to Internet service demands by integrating data services over their coaxial cable networks, which were initially designed for analog video broadcast [1]. A drawback to this approach is that the approximately 36Mb/s bandwidth which is provided by the cable companies is typically divided between 2000 homes, which leads to very slow speed during peak hours [1]. In spite of this, DSL and cable modems are an improvement over 56 kb/s modems, but they are not capable of providing enough bandwidth for up-and-coming services such as IP telephony, video on demand (VoD), interactive gaming, or two-way videoconferencing [1]. To provide virtually unlimited bandwidth to residential customers, Bellsouth installed the first APON fiber-to-the-home (FTTH) system in North America in 1999 and began offering video and high-speed data services to trial customers [2]. However, EPON, which represents the convergence of low-cost Ethernet equipment and low-cost fiber infrastructure, is emerging as the best candidate for next-generation access networks [1]. When the Full Service Access Network initiative began in 1995, ATM was positioned to become the prevalent technology in the Local Area Network (LAN), Metropolitan Area Network (MAN), and backbone. Since that time, however, Ethernet technology has surpassed ATM.

In addition to access networks, optical communication has become a very important technology in advanced military, avionics, shipboard, and aerospace systems. This technology can be found on different platforms. Table 1, which is categorized by platform, highlights a few of the applications.

Table 1: Optical communication in different non-telecommunications platforms [6]

Platform	Applications
Land Based	Tactical communications systems Fiber optic guided missile (EFOGM)
Marine and Shipboard	AEGIS network backbone PHALANX close-In Weapon System (CIWS) Towed sensor arrays
Military Avionics	Eurofighter F-22 Raptor tactical fighter RAH-66 Comanche helicopter Fiber optic towed decoys (FOTD)
Commercial Avionics	Boeing 757 In-Service Program (Fly-by-light testbed) Boeing 777 Optical Local Area Network In-Flight Entertainment (IFE) systems
Space	NASA X-Ray Timing Explorer (XTE) NASA Hubble Space Telescope (HST) International Space Station Laser initiation systems

In MAFA systems the main advantages of fiber optics over copper or coax cables are small size, lightweight, ultra high bandwidth, high bandwidth-density product, EMI/RFI isolation, radiation resistance, and resistance to obsolescence [6]. To quantify the size and weight advantage, consider that the life–cycle cost of 1 pound of payload is about $1000 for a commercial aircraft, the majority of which is fuel cost. With a fiber optic-based landing gear system, the overall weight of a jumbo jet can be reduced by approximately 250 pounds, representing a savings of $250,000 per jet [6]. Other platforms that can take advantage of this savings acquired from switching to a fiber-based system are satellites and spacecrafts. The fuel cost per pound per launch is $20,000 to $50,000 [6].

As the demand for FTTX and MAFA continue to increase, there will be an increasing demand for affordable optical network units (ONUs). The main component of ONUs is the optoelectronic transceiver, and the cost of the ONU is critical. One approach to affordable ONUs is single fiber bi-directional communications. There are several different approaches to making an optoelectronic transceiver for single fiber bi-directional communications.

The first approach used biconical couplers and an emitter/ detector pair at both ends of the optical fiber to communicate [7]. A simpler approach, which eliminated the need for a coupler, used a bi-functional device such as an LED, edge-emitting laser (EEL), or vertical cavity surface emitting laser (VCSEL) at both ends of the link [8], [9], [10]. These bi-functional devices are capable of operating as light emitters or photodetectors, depending on how they are biased. Because these devices are inherently light emitters, the optimum structural designs have to be altered to improve the

sensitivities of these devices in detection mode, which compromises the performances of the devices in light emission mode. Another approach used a new structure containing two p-n junctions, which operated as an LED and a heterojunction phototransistor, alternately [11]. Two similar approaches used a photonic integrated circuit (PIC) at each end of the optical link [12], [13]. The two p-n junction device and the PICs were grown monolithically. Even though the emitter and the detector were separated using a monolithic approach, the growth material and structure was limited due to the lattice-matching conditions. To avoid this limitation, a hybrid integration method was used to integrate a thin film GaAs-based LED onto a large silicon CMOS bipolar junction detector [14]. In order to increase the responsivity and speed of the detector, a material other than silicon needed to be used. The research herein uses a heterogeneous integration method to stack two independently grown and customized thin film devices onto SiO_2-coated silicon and a silicon CMOS transceiver circuit to form a 3D integrated optoelectronic transceiver.

1.2 Dissertation Outline

This dissertation presents the results of an experimental study of thin-film emitters and detectors that are stacked and 3D heterogeneously integrated onto SiO_2-coated silicon and silicon CMOS transceiver circuitry to form an optoelectronic transceiver for single optical fiber bi-directional communication. The emitters and detectors were designed and grown independently, separated from their growth substrate using selective etching and stacked in 3D on top of one another, with the detector on the bottom. The thin-film devices that were fabricated and studied in detail were resonant cavity light emitting diodes (RCELEDs) and inverted metal-semiconductor-metal (I-MSM) photodetectors (PDs).

Chapter 2 provides background information about different devices used to providing single fiber bi-directional optical communications. It discusses the approach of using bi-conical couplers along with an emitter/detector pair on each end of the link to provide full duplex communication. Also covered in this chapter is a review of bi-functional devices such as LEDs, edge-emitting lasers, and VCSELs that are used for half duplex single fiber bi-directional communications. In addition, monolithically grown photonic integrated circuits and co-located emitter and detector devices are highlighted.

Also included in this chapter is the device physics for the integrated devices. This section gives a brief review of p-n and metal-semiconductor junction theory. These theories are then extended to light emitters and photodetectors. The light emitters discussed are LEDs, RCELEDs, and VCSELs. The coupling efficiency of the LED light into an optical fiber is also covered. The photodetectors discussed are PINs and MSMs. A capacitance comparison between the two photodetectors is included.

The last few sections of chapter 2 describe different optoelectronic integration techniques. More established hybrid integration techniques such as flip-chip, bridge, and wire bonding, are discussed first. Following these approaches is a review of more recently developed techniques such as epitaxial liftoff (ELO), appliqué, and fluidic assembly integration techniques. The fabrication of thin-film LEDs and I-MSM PDs using a thin film heterogeneous integration process is discussed for the research in this thesis.

Chapter 3 covers the process used to fabricate the 3D stacked optoelectronic transceivers. This chapter highlights the ability to fabricate devices of different size, shape, and material using the thin film heterogeneous integration process. Some measurement results are included with each demonstration.

Chapter 4 describes a geometrical optics approach used to provide the theoretical analysis of coupling efficiency between an LED and a multimode optical fiber, and between a multimode fiber and a photodetector. The longitudinal and lateral alignment tolerance is also discussed.

Chapter 5 compares the experimental results to the calculated results. The results include the responsivity of the I-MSM PD with LED shadowing, LED and I-MSM PD bandwidth, and LED coupling efficiency. Also covered is the alignment tolerance of the stacked device.

The final chapter summarizes the goal of this research and the contributions made to the field. It also points out how this research can be extended into the future.

CHAPTER 2

BACKGROUND

2.1 Literature Review

2.1.1 Biconical Tapered Coupler

The development of full duplex bi-directional communication over a single fiber was hindered by the lack of suitable access or directional couplers to couple the light source and photodetector to a single fiber [7]. High quality full duplex transmission of analog-modulated video over a single multimode fiber was achieved in 1977 [7]. The transmission link employed fused biconical taper couplers, a device that exhibited low insertion loss, high coupling to the transmission line, and high isolation, which were required for high performance bi-directional communication. The coupler was fabricated using two sections of multimode fiber that were twisted around one another, then heated using a torch to fuse the two fibers for a short distance along the side where they were contacted. The fibers were simultaneously pulled during the heating to form twin biconical sections, which were fused side by side over the entire length of the tapered sections. Optical power transfer occurred by the conversion of guiding modes to cladding modes in the decreasing taper section in the input arm, transfer of a portion of these cladding modes across the fused region of the structure to the other fiber, and the subsequent conversion of these cladding modes to core-guided modes by the increasing tapers of the two output arms of the couplers [7]. Up to 50% of the optical power in a line was coupled, and excess insertion loss was –0.5 dB when 30% coupling occurred [7]. The directional isolation was very high, which minimized the cross coupling between the

downstream and upstream signals. The biconical taper coupler, which is shown in Figure 1, made single fiber full duplex bi-directional communication possible, which reduced the amount of fiber need for fiber optic links. However, many optical fiber communication applications only required half-duplex operation.

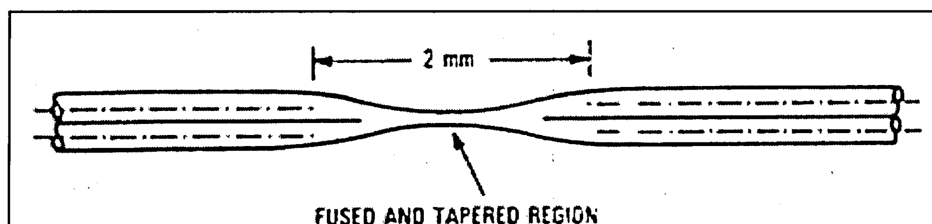

Figure 1: Biconical Coupler [7].

2.1.2 Bi-functional LED

In industrial control and instrumentation systems, half duplex data distribution systems were commonly used. With a half duplex system, a coupler could still be used. In a more economical half-duplex system, an optical distribution system using an LED source-detector (LED-DET) scheme, that is, LEDs used as both a light source and as a photodetector was proposed in 1978 [8]. In this system the use of optical directional couplers and conventional photodiodes were eliminated. When the sensitivity of the LED's used in the LED-DET scheme was better than the sensitivity of the conventional photodiodes reduced by the furcation loss, which was twice the insertion loss of the optical directional coupler, the system using the LED-DET scheme surpassed the conventional half duplex optical transmission systems using directional couplers [8]. In this system, high radiance GaAs-GaAlAs LED's operated as heterojunction photodiodes under reverse-bias voltage in the detection mode. Four different LED structures were

studied using the LED-DET scheme. The first optical bi-functional device studied was a multiheterojunction GaAs-GaAlAs LED (MH LED) with a tapered fiber launcher. The MH LED had a GaAs active layer with a thickness of 0.2 μm, which was located in the middle of the $Ga_{0.9}Al_{0.1}As$ optical waveguide with a thickness of 2.0 μm. The optical power coupled into the multimode step index fiber with a core diameter of 80 μm and

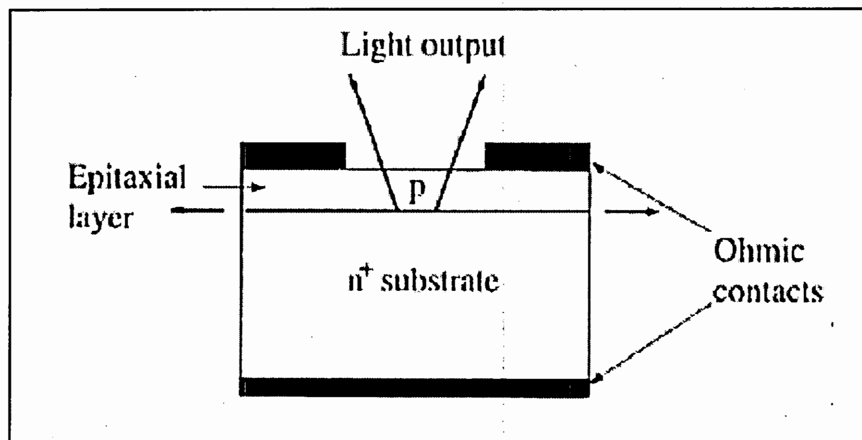

Figure 2: Surface Emitting LED [15].

N.A. = 0.26 from the MH LED was 500 μW at 120 mA. The sensitivity of the MH LED in detection mode was 0.028 A/W at 2 V. The 3 dB bandwidth was 25 MHz in the LED mode and 65 MHz in the detection mode. The results showed that the LED as a photodetector was characterized by a relatively low sensitivity and a large diode capacitance [8]. The sensitivities of a DH LED, a Burrus LED, and a MH LED without a tapered fiber were measured. The sensitivity of the DH LED with $Ga_{0.7}Al_{0.3}As$ layers on both sides a GaAs active layer was 0.005 A/W. The MH LED consisted of a waveguide layer of $Ga_{0.9}Al_{0.1}As$, which also included a GaAs active layer and a $Ga_{0.7}Al_{0.3}As$ cladding layer. The sensitivity of the MH LED was 0.011A/W. The sensitivity of the

Burrus LED was 0.12A/W [8]. Figure 2 and Figure 3 shows the schematics of a surface emitting LED and a Burrus LED, respectively.

Another investigation on the use of three types of LEDs as semiconductor junction transceivers (SJT) was also reported [16]. The types of SJTs studied were: a GaAlAs edge-emitter with fiber optic pigtail, GaAsP large area surface emitter, and a Burrus diode. To determine the detection capability of the LEDs, the external quantum efficiencies were measured, which was defined as the ratio of the short circuit electron current to the incident photon current. The GaAs Burrus diode peak quantum efficiency was ~10^{-4}. At short wavelengths, corresponding to photon energies greater than the band

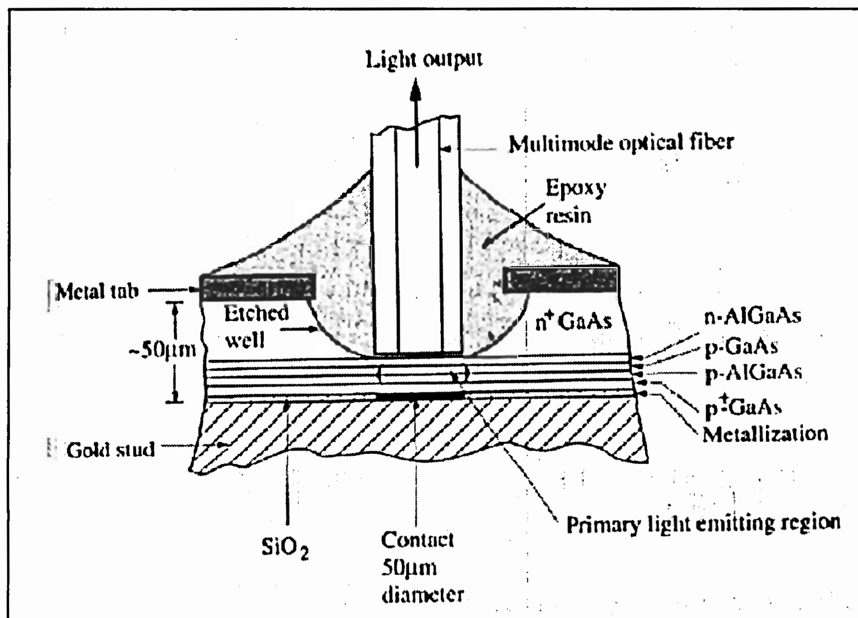

Figure 3: Burrus LED [15].

energy, the absorption coefficient was large; electron hole pairs were created near the surface where surface recombination effects became important and limited the photosensitivity [16]. The GaAsP surface emitter had higher quantum efficiency and broader spectral response than the Burrus diode. Within the edge emitting diode the field

that separated the electron hole pairs was perpendicular to the direction of the incident optical flux, and extended to the surface of the diode [16]. Therefore, the quantum efficiency was less dependent on photon energy than in the surface emitting diode. This was apparent from the broad spectral response of the quantum efficiency for the edge emitter. The quantum efficiency was 0.7%, which was low compared to the other LEDs. This was mainly due to the low coupling efficiency of the optical fiber to the edge emitting diode. This investigation also reported that the dark current in the surface emitting diodes was below 1-nA with reverse bias as high as 15 V. The edge emitter and Burrus LEDs had much higher dark currents. It was concluded that broad area surface emitting GaAsP LED used as semiconductor junction transceivers could perform at levels suitable for low cost fiber optics industrial instrumentation and control systems with large diameter fiber [16]. The penalty for using an SJT instead of an LED/PIN diode combination was a factor of five loss in responsivity [16].

To improve the sensitivity, avalanche gains in LEDs were studied [17]. A double heterostructure Burrus-type LED was examined. Unlike silicon photodetectors, which exhibit essentially constant sensitivity over a wide variation of reverse bias, the sensitivity of these LEDs depended heavily on the reverse bias conditions. The maximum quantum efficiency was 5.7A/W. Unfortunately, the dark current of the LED increased with the increase in reverse bias. This resulted in an optimum signal to noise ratio at a gain of about half of the maximum gain [17]. The LED had an external quantum efficiency of 2.5 A/W at the optimum point with a dark current of 6-nA at 20-V reverse bias.

2.1.3 Two p-n Junction Device

With the LED operating in detection mode, the device was either characterized by low sensitivity or relatively high applied bias. To avoid this problem, a device with a new structure containing two p-n junctions that operated as an LED and a heterojunction phototransistor (HPT), alternately, with a low applied bias voltage was grown by the conventional slider-boat LPE technique [11]. The LPE process was in two stages. In the first stage, an undoped GaAs (collector) and a p-GaAs (base) layer were grown on the Si-doped GaAs substrate. In the second stage n-$Ga_{0.7}Al_{0.3}As$ (emitter/LED lower confinement, p-$Ga_{0.95}Al_{0.05}As$ (active layer), and p-$Ga_{0.7}Al_{0.3}As$ (upper confinement layer) were subsequently grown on the wafer. A view of the device is shown in Figure 4. In the LED mode, the device emitted light at a peak wavelength of ~840 nm with a Lambertian profile. The external quantum efficiency was ~1% and the 3 dB bandwidth

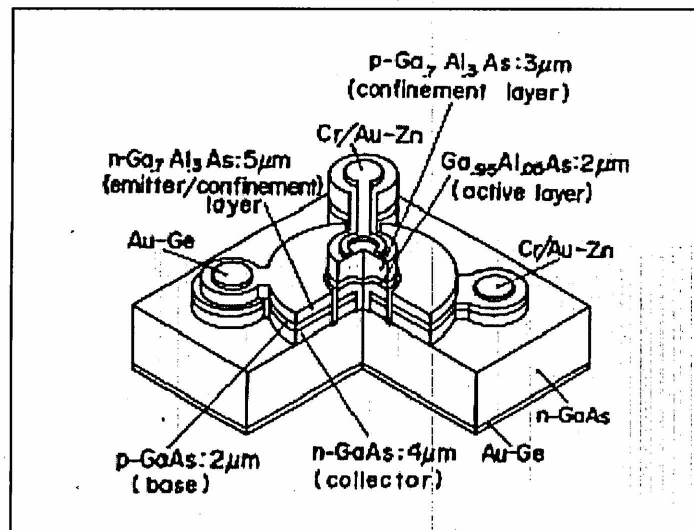

Figure 4: Structure with two PN junctions [11].

was 10 MHz. In the HPT mode, the device detected light in the 700-870 nm wavelength range. The sensitivity was 2 A/W and the 3 dB bandwidth was 5 MHz.

2.1.4 Bi-functional Laser

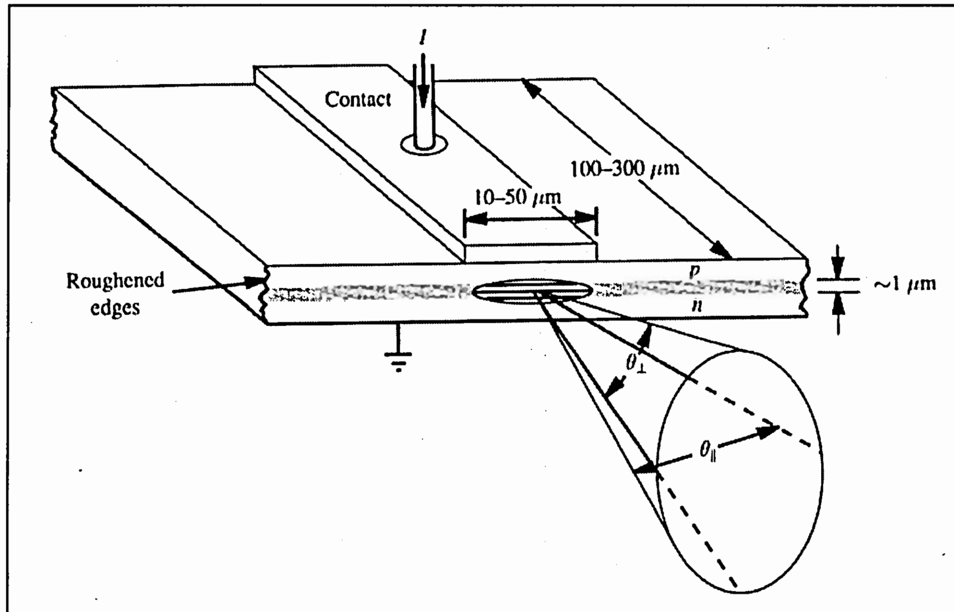

Figure 5: Edge Emitting Laser [18].

The HPT bandwidth was one of the most important limiting factors in the optical communication link. Another alternative to the LED that increased the bandwidth and the sensitivity of the optical link was to use a laser instead of an LED as a bi-functional device. It has been reported that lasers possess the qualities of a photodetector with a gigabit per second detection capability [9]. The use of lasers in analog and digital half duplex optical communications links improved both the transmission capability and the power margin of the transmission system [9]. A channeled-substrate planar (CSP) structure GaAs/GaAlAs laser operating as a bi-functional device at 100 Mbps in a half duplex transmission experiment using a 500 m single-mode fiber was reported [9]. The laser was either forward biased or zero biased, depending on whether the laser was in transmitting mode or receiving mode. This laser is shown in Figure 5.

The laser emitted at an 830 nm wavelength with a full width of 3.74 μm at e^{-2} of the peak intensity. When the laser was zero biased or reverse biased, the light incident on the active region was absorbed and the laser performed like a photodetector. The responsivity in this mode was 0.15 A/W. The bandwidth of the CSP laser/detector was limited by the large capacitance of the planar structure of the diode [9]. The impulse response of the laser/detector was 2.5 ns (FWHM) at zero bias. At a data rate of 100 Mbps an optical power margin of 14 dB for a bit error rate of 10^{-9} was obtained. One problem with the laser was that the responsivity was not broad enough to account for the extremely broad spectral responsivity range needed for a low cost configuration.

2.1.5 Photonic Integrated Circuit

To combat the broad spectral range problem, a simple photonic integrated circuit (PIC) that would have the benefits of the laser plus the desired broad spectral responsivity range was constructed [12]. The PIC was a simple in-line waveguide device, with the integration of a gain section, a specially designed detector, and a beam expander. All three sections were integrated inside the Fabry-Perot cavity of a laser along an underlying waveguide. To obtain a broad spectral responsivity range, a 1.4 μm bulk quaternary layer was add to the detector region. By making use of the high gain provided by the MQW layers together with the polarization independent response of the bulk active layer in the detector section, an optimized gain and detector section was achieved. The detector section did not significantly degrade the performance of the laser. The purpose of the beam expander was to reduce the packaging cost of the PIC. With the beam expander

there was no need for a lensed fiber, as good coupling into a cleaved single-mode fiber was achieved [12]. Figure 6 shows the schematic structure of the PIC.

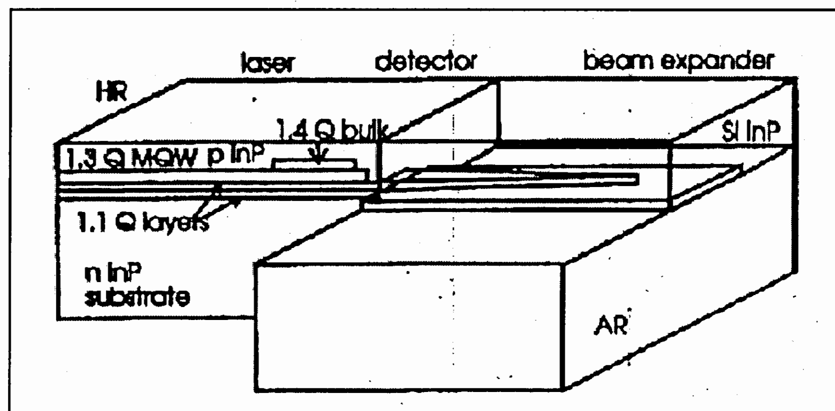

Figure 6: Schematic structure of PIC [12].

The bi-functional device included three sections: a laser, a detector, and a beam expander integrated along an underlying backbone of the waveguide. Two InGaAsP quaternary layers, with λ_p = 1.1 μm, separated by an InP stop etch layer formed the underlying waveguide structure. The bottom layer was 800 Å thick and the top layer was 1400 Å thick. The laser section consisted of six compressively strained (0.9%) 70 Å thick quantum wells, and 150 Å tensile strained barriers. The length of the laser section was 500 μm. The detector section consisted of MQW layers and an 800 Å bulk layer. This section was electrically separated from the laser section. To decrease the amount of capacitance this section was only 85 μm in length, which yielded a capacitance that was approximately 2 pF [12]. The beam expander section consisted of a top layer that was adiabatically tapered laterally from 3 μm to termination. The bottom remained 5 μm in width along the 300 μm beam expander section. The purpose of the section was to transform the elliptically shaped mode both laterally and vertically to a shape that better

matched the shape of the mode in a single-mode fiber [12]. The PIC was grown in four steps by metal organic chemical vapor phase epitaxy. First, the waveguide layers, the MQW, and the bulk $\lambda_p = 1.4$ μm InGaAsP were grown.

To increase the responsivity of the device the front facet was antireflection (AR) coated. The highest responsivity measured was 0.43 A/W, with very low sensitivity to polarization. The specially designed detector had a broad spectral range of 80 nm. The laser section operated in two different ways. One way was to simultaneously drive the gain section and the detector, which yielded a threshold of ~65 mA. A better operation scheme was to drive the detector section at a constant current that was higher than 30 mA, which yielded a threshold of 20 mA.

Another PIC that was fabricated for fiber access systems was a monolithically integrated semiconductor LED-amplifier device [13]. As a transmitter source, the integrated LED-amplifier operated at 1.3 μm wavelength with about 10 mW chip output power and a few milliwatt of power coupled into a single mode fiber. As a receiver, the amplifier section of the PIC was used as a waveguide photodetector. A schematic diagram of the monolithically integrated LED-amplifier is shown in Figure 7.

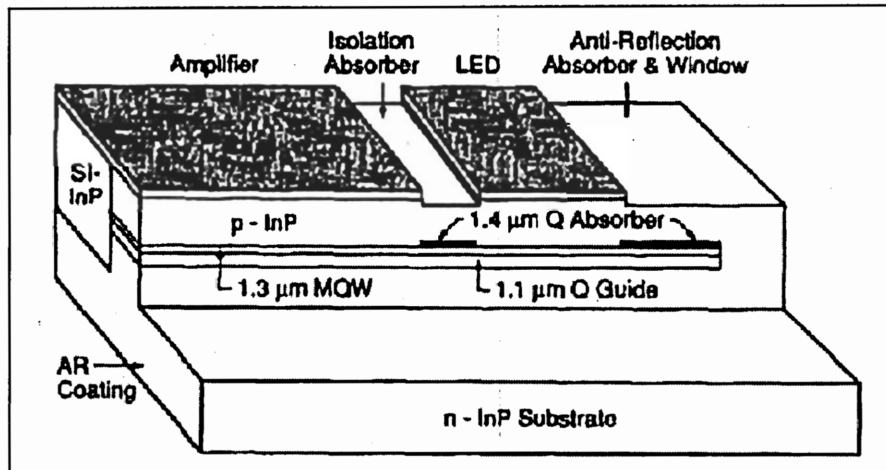

Figure 7: Monolithically integrated LED-amplifier [13].

The device was fabricated with two active elements. The back active section was used as a conventional LED and the front section amplified the input from the LED to higher output power. Single-mode buried heterostructure waveguides were used in this integration. The active regions consisted of six compressively strained 50 Å thick InGaAsP (λ_g = 1.36 µm) quantum wells with 150 Å thick InGaAsP (λ_g = 1.1 µm) barriers and an underlying 2000 Å InGaAsP (λ_g = 1.1 µm) thick guiding layer. The same active waveguide structures were used for both the LED and the amplifier for optical emission and gain around a λ = 1.3 µm wavelength. To provide partial isolation and to avoid forming a long superluminesent diode, a simple waveguide absorber was grown between the LED and the amplifier [13]. A thin InGaAsP (λ_g = 1.4 µm) layer was grown on top of the MQW layer to absorb more uniformly the LED light over a broad spectral range. The length of the waveguide absorber /isolator was 40~60 µm, which was adjusted to provide 6 to 8 dB attenuation while transmitting 0.2 mW of LED light into the amplifier. The backside of the LED also had a 170-µm long waveguide absorber followed by an unguided region, which eliminated optical reflections from the back facet.

The lengths of the integrated amplifier and LED were 550 μm and 300 μm, respectively. The device was grown by four-step metal organic vapor phase epitaxy (MOVPE).

With 125 mA of current applied to the amplifier, a 10 mW chip optical output with 4 mW coupled into a single mode fiber were obtained with about 150 mA current applied to the LED [9]. The broad spectral response was 300 Å to 500 Å FWHM. The zero or reverse biased integrated amplifier was used as a photodetector. The 550 μm long amplifier in receiving mode produced a large capacitance of 10 pF, which limited the receiver sensitivity. Also, the detector was more sensitive to TE polarization than TM because the MQW active layers were compressively strained [13].

2.1.6 Bi-functional VCSEL

Another semiconductor device that can operate as a bi-functional device with limited detector device optimization is the vertical cavity surface emitting laser (VCSEL). The idea behind this research was to exploit the property of resonant cavity enhancement (RCE) inherent in the VCSEL, along with avalanche gain, in order to achieve an efficient photodetector performance, while maintaining the lasing function [10]. To achieve this, the emitting facet reflectivity was reduced to allow improved injection of light into the cavity for detection, but was maintained at a sufficiently high level to allow the device to continue to perform as a laser [10]. Therefore, the tradeoff that was made in optimizing the device was to reduce the top mirror reflectivity (required for increased light injection onto the cavity and to broaden the spectral range of the detector) but still maintaining a high enough level for low threshold and efficient lasing [10]. The VCSEL structure used was a proton bombarded, top-emitting device with an aperture of 12 μm, operating at

around 850 nm. The cavity was formed using top and bottom mirrors consisting of 20 and 32.5 GaAs-AlAs mirror pairs, respectively. The active region consisted of three 70 Å GaAs quantum wells. A schematic of a cross section of is shown in Figure 8. Before device modification the typical threshold current was 4.5 mA with the slope of the L-I curve 0.26 mW/mA for output powers up to 2 mW. After etching away the mirrors, the threshold current was 6.5 mA, while the slope of the light curve increased to 0.33 mW/mA. The quantum efficiency of the VCSEL in detection mode was 14% at zero bias. The dark current increased with applied bias to 20 nA at 8 V, and just around 150 nA just below breakdown. The observed breakdown voltage was 8.7 V. The range of wavelengths over which the VCSEL absorbed light was very narrow, due to the high selectivity of the Fabry-Perot

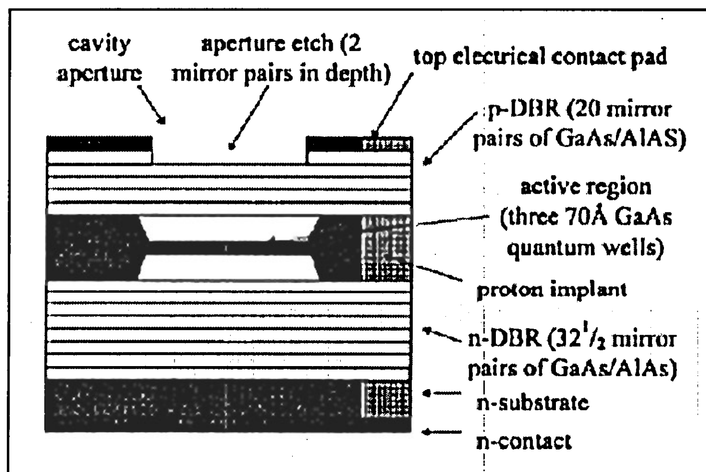

Figure 8: Schematic cross section of a VCSEL [10].

resonant cavity formed by the mirrors. The spectral response had an absorption peak with a FWHM of 2.4 nm, which occurred at the same wavelength that the lasing peak occurred. The VCSEL transceiver operated between 1 and 2 Gbps with an estimated capacitance of 1.2 pF [10].

2.1.7 Co-located Emitter and Detector

When a laser and a detector grown monolithically or a single bi-functional device such as an LED is used to create a transceiver, the optimization of individual devices is limited. To avoid this problem, a transceiver was fabricated by growing and optimizing a GaAs based LED, separating it from its growth substrate, and integrating it onto a silicon detector array with analog optoelectronic transceiver interfaces and digital circuitry on the same chip[14]. A schematic view of the silicon phototransistor is shown in Figure 9.

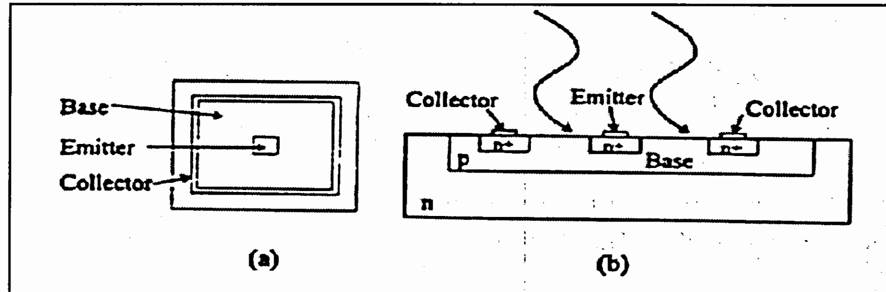

Figure 9: Schematic of bipolar junction phototransistor with integrated LED [14].

This heterogeneous integration approach enabled an emitter to be optimized without the risk of degrading the performance of the silicon detector. The double heterostructure LED was composed of a 100 Å highly doped p-type GaAs contact layer, a 2.24 μm p-type $Al_{0.3}Ga_{0.7}As$ buffer layer, 5000Å intrinsic GaAs active layer, a 2.24 μm n-type $Al_{0.3}Ga_{0.7}As$ injection layer, and a highly doped n-type contact layer. The structure was grown on top of a 2000 Å AlAs sacrificial etch layer. This AlAs sacrificial layer enabled the separation of the epitaxial devices from its growth substrate. The devices were then bonded to a transfer diaphragm for subsequent bonding to the center of the silicon detector circuit. The silicon detector was a 1 mm x 1 mm array of phototransistors with

the base current controlled by the incident optical light. The maximum operating frequency of the system was 50 kHz, which was limited by the large gain, low bandwidth amplifier [14].

To achieve higher speeds and responsivity, material systems other than silicon must be used for the emitter and photodetector. This dissertation presents a heterogeneous integration method that was used to stack a GaAs RCE LED on top of either a GaAs or an InGaAs I-MSM PD. With the LED in the center of the larger I-MSM PD, a coupler is unnecessary for single fiber bi-directional communication. Unlike the bi-functional devices such as the LED, EEL, and VCSELs, described previously, the performance of one function is not compromised to improve the other, because there is a device for each function. Furthermore, the material and structure of the 3D stacked device are not limited because of lattice matching constraints, in contrast to photonic integrated circuits. Each device is designed and grown independently, removed from its growth substrate using a thin film integration process, and stacked. A schematic of the 3D stacked device is shown in Figure 10.

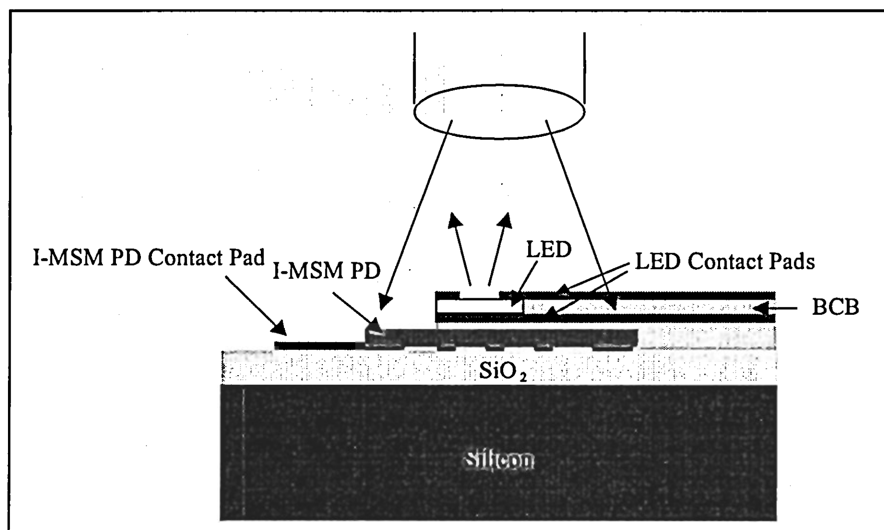

Figure 10: 3D stacked thin film device

2.2 3D Stacked Device Physics

2.2.1 Junctions

To understand the devices used in this research a brief review of junction theory is necessary. The two junctions that are of importance to this research are p-n junctions and metal-semiconductor junctions. These junctions are fundamental to the performance of functions such as rectification, amplification, switching, and other operations in electronic circuits, as well as in photonic devices.

2.2.1.1 p-n Junctions

The first junction to be discussed is the p-n junction. Let us consider two separate semiconductors, one p-type and the other n-type, as shown in Figure 11. As these two materials are joined together to form a junction by a growth, alloying, diffusion, or implantation technique, electrons from the n-type material diffuse to the p-type material, which has a much lower concentration of electrons. The same action happens on the other side of the junction with the holes diffusing into the n-type material. Unlike two types of air molecules, which would continue to diffuse until a homogenous mixture has formed, an opposing electric field created by the ionized donors and acceptors limits the amount of diffusion. In equilibrium the electric field builds up to a point where the net current is zero [19]. The region in which the electric field exists is called the depletion region, since it is nearly depleted of carriers compared to the rest of the bulk material. The width, W of the region is related to the built-in potential difference or voltage, V_o, across the depletion region. The band diagrams before and after forming the junction are shown in Figure 11.

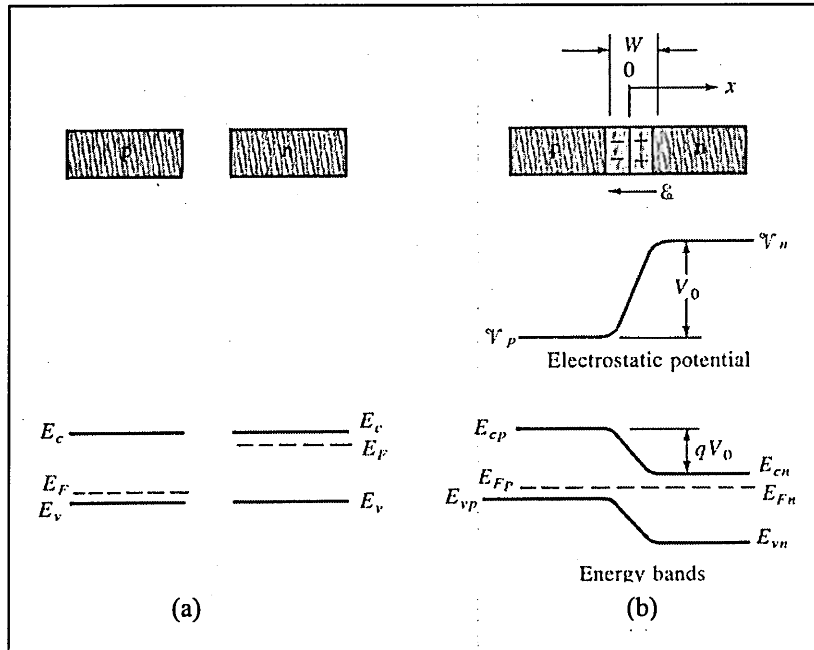

Figure 11: (a) Separate p and n type semiconductors and their band diagrams, and (b) formation of depletion region when materials are joined together and corresponding contact potential and energy band diagram [19].

A quantitative relationship between V_o and the doping concentration can be found by considering the equilibrium current equations. The electron and hole current densities, $J_n(x)$ and $J_p(x)$, respectively, are given by [19]

$$J_n(x) = q\mu_n n(x)E(x) + qD_n \frac{dn(x)}{dx}$$ **Equation 1**

$$J_p(x) = q\mu_p p(x)E(x) - qD_p \frac{dp(x)}{dx}$$ **Equation 2**

where q is the magnitude of the electron charge, $E(x)$ is the electric field, μ_n and μ_p are the electron and hole mobilities, $n(x)$ and $p(x)$ are the electron and hole concentrations, and D_n and D_p are the electron and hole diffusion coefficients, respectively. The built-in voltage is given by [19]

$$V_o = \frac{kT}{q} \ln \frac{N_a N_d}{n_i^2}$$ **Equation 3**

where k is Boltzmann's constant, T is the absolute temperature, n_i is the intrinsic carrier concentration, N_a and N_d are the acceptor and donor concentrations, respectively.

The depletion width, W, is given by [19]

$$W = \left[\frac{2\varepsilon V_o}{q} \left(\frac{1}{N_a} + \frac{1}{N_d} \right) \right]^{1/2}$$ **Equation 4**

where ε is the semiconductor dielectric constant. When a voltage is applied to the p-n device, the depletion width changes. The effects of applying a voltage can be seen in Figure 12. By applying a forward bias, the electrostatic potential barrier is lowered, corresponding to a smaller depletion width. However, by applying a reverse bias, the electrostatic potential barrier is raised, which translates to a widening of the depletion region.

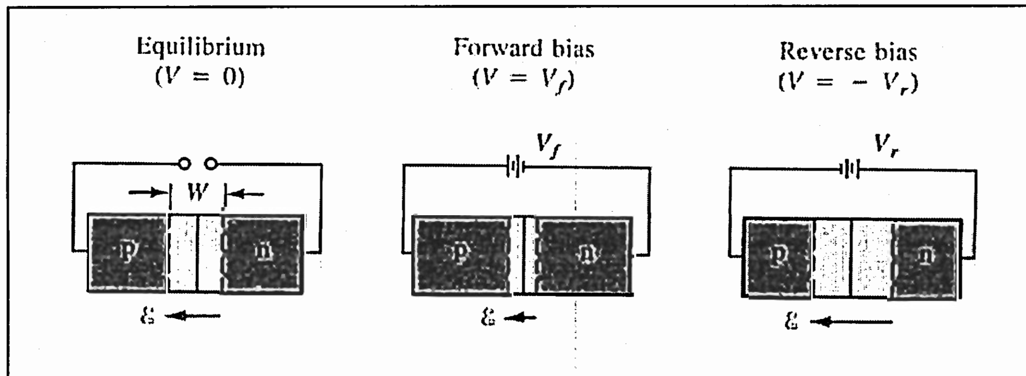

Figure 12: Effects of bias at a p-n junction on depletion width [19].

A varying depletion region results in a varying capacitance. There are two types of capacitance associated with p-n junctions: (1) the junction capacitance that depends on the depletion region and (2) the charge storage capacitance that arises from voltage lagging a changing current [19]. The junction capacitance is dominant under reverse bias

and the storage capacitance is dominant under forward bias. The junction capacitance is given by [19]

$$C_j = \frac{\varepsilon A}{W} \qquad \textbf{Equation 5}$$

where ε is semiconductor dielectric constant, W is the depletion width, and A is the cross-sectional area of the junction. The charge storage capacitance for a p^+-n junction, where p^+ indicates a heavily doped p-type junction, is given by [19]

$$C_s = \frac{q^2}{kT} A L_p P_n e^{qV/kT} = \frac{q}{kT} I \tau_p \qquad \textbf{Equation 6}$$

where A is the cross-sectional area, L_p is the hole diffusion length, P_n is the minority hole concentration, V is the applied voltage, I is the applied current, and τ_p is the minority carrier lifetime. This equation assumes that the p^+-n junction is forward biased in steady state with V, and has a steady state current I. The charge storage capacitance can be a very serious problem for LEDs, which are forward biased p-n junctions, by limiting the high speed operation.

2.2.1.2 Metal-Semiconductor Junction

As stated earlier, p-n junctions can be used to perform many electronic circuit functions. However, a simpler junction to fabricate is a metal-semiconductor junction, which can perform some of the same functions, such as high-speed rectification. Unlike the multiple masking steps required to make p-n junctions, the metal-semiconductor junction requires one mask to define the contact pattern and the deposition of an appropriate metal film. When a metal is brought in contact with a semiconductor, charge is transferred until the Fermi level is aligned. This charge motion causes an electric field

to form that limits the amount of electrons that diffuse. In compound semiconductors, unlike silicon, metals which form ohmic contacts and Schottky barriers are identified empirically, i.e., there is no consistent relationship between work function and electron affinity which can consistently predict whether a metal/semiconductor interface will form an ohmic or Schottky contact. Just as in the case of a p-n junction, a depletion region is formed near the junction with width, W. The resulting current from a forward biased metal-semiconductor Schottky barrier junction diode is given by [15]

$$I = ABT^2 e^{-q\phi_B / kT} e^{qV / nkT} \qquad \textbf{Equation 7}$$

where A is the Richardson constant, B is the junction parameter constant, T is the absolute temperature, q is the magnitude of the electron charge, k is Boltzmann's constant, $q\phi_B$ is Schottky barrier height, and n is the ideality factor. The capacitance of the device is related to its depletion width. Since the Schottky barrier on an n-type semiconductor is similar to a p^+-n junction, the width is similarly given by [20]

$$W = \left[\frac{2\varepsilon (V_{bi} - V)}{qN_d} \right]^{1/2} \qquad \textbf{Equation 8}$$

where ε is the semiconductor's dielectric constant, V_{bi} is the built in voltage, V is the applied voltage, and N_d is the donor concentration. The capacitance is given by [20]

$$C_j = \frac{\varepsilon A}{W} \qquad \textbf{Equation 9}$$

where A is the cross-sectional area, ε is the semiconductor's dielectric constant, and W is the depletion width.

2.2.2 Light Emitters

2.2.2.1 Light Emitting Diodes

An LED is a simple p-n junction that spontaneously emits light when forward biased. Under forward bias, electrons are electrically injected into the p side and holes are electrically injected into the n side of the junction [21]. As the minority carriers diffuse away from the junction, they recombine with the majority carriers. A semiconductor bandgap can be direct or indirect. Semiconductors are classified as either direct or indirect materials depending on the shape of the band gap as a function of momentum, k [21]. Semiconductor LEDs are comprised of direct bandgap semiconductors, which means that most of the injected carriers recombine radiatively. Most of the recombination occurs near the junction. The amount of energy emitted when the carriers recombine is near the bandgap energy of the semiconductor and is related to the frequency at which the photon is emitted where,

$$E_g \cong h\lambda \qquad \textbf{Equation 10}$$

The wavelength of light required usually determines the type of semiconductor that is necessary. GaAs has a direct bandgap of 1.43eV ($\lambda \approx 850\mu m$) at room temperature and therefore emits in the near-infrared region [19].

The processes occurring in a junction LED can be divide into three stages: (1) The excitation or injection stage where excess carriers are injected into the junction by forward bias; (2) the recombination stage where excess carriers give up their energy as photons; and (3) the extraction stage where the photon leaves the semiconductor [15]. Each of these of the processes has an efficiency which contributes to the overall device efficiency, η_o, that is expressed as,

$$\eta_o = \eta_{in}\eta_r\,\eta_e$$ **Equation 11**

where η_{in}, η_r, and η_e are the injection, recombination and extraction efficiency, respectively. An injection efficiency of η_{in} = 0.8 can be achieved for GaAs. In direct bandgap materials the radiative recombination efficiency is usually ~ 50% for homojunction devices and 60-80% for double heterojunction devices [15]. Given these high efficiencies for η_{in} and η_r, a critical factor in the overall device efficiency is the extraction efficiency. Several factors influence the amount of light that emerges from the device. One of the most important factors is the absorption coefficient of the semiconductor. In GaAs the absorption coefficient, α, is about 10^3 cm^{-1} at $\lambda \approx 850$ nm, which implies that after traversing 2 μm, half of the photons are reabsorbed [15]. Two other factors that affect the extraction efficiency are surface state nonradiative recombination and device geometry. The external quantum efficiency, η_o is defined as the ratio of the optical power, P_o, to the electrical input power, P_e, which is expressed by [15],

$$\eta_o = \frac{P_o}{P_e}$$ **Equation 12**

This equation takes in to account the extraction efficiency. Typical values for η_o range from 1% to 5% for LEDs.

When trying to couple light into a fiber, the radiation pattern of the emitter must be known. LEDs are characterized by their Lambertian output pattern, which means that emitted light is equally bright when viewed from any direction [22].

The power delivered from an LED at an angle θ measured relative to a normal to the emitting surface varies with *cos (θ)*, where the brightness function is given as [22]

$$B(\theta,\phi) = B_o \cos\theta \qquad \textbf{Equation 13}$$

where B_o is the radiance along the normal to the radiating surface. The total optical power emitted from a surface emitting LED of area, A_{LED}, and aperture radius, r_{LED}, is given by [22],

$$P_{LED} = A_{LED} \int_0^{2\pi} \int_0^{\pi/2} B(\theta,\phi) \sin\theta \, d\theta \, d\phi$$

$$= \pi r_{LED}^2 \left(2\pi B_o \int_0^{\pi/2} \cos\theta \sin\theta \, d\theta \right)$$

$$= \pi^2 r_{LED}^2 B_o \qquad \textbf{Equation 14}$$

When the radius of the fiber core is larger than the radius of the LED, the power coupled into a step-index fiber is calculated by integrating over the solid acceptance angle, which is related to the fiber numerical aperture, NA, and is given by [22],

$$P_{Step} = \int_0^{r_{LED}} \int_0^{2\pi} \left(2\pi B_o \int_0^{\theta_{o,max}} \cos\theta \sin\theta \, d\theta \right) d\phi \; r dr$$

$$= \pi B_o \int_0^{r_{LED}} \int_0^{2\pi} \sin^2\theta_{o,max} \, d\phi \, r dr$$

$$= \pi B_o \int_0^{r_{LED}} \int_0^{2\pi} (NA)^2 \, d\phi \; r dr$$

$$= \pi^2 r_{LED}^2 B_o (NA)^2 = \pi^2 r_{LED}^2 B_o (n_1^2 - n_2^2)^{1/2} \qquad \textbf{Equation 15}$$

Therefore, the coupling efficiency between an LED and a step index fiber with a core diameter that is larger than the LED diameter is given by [22], [23], [24], [25], [26], [27],

$$\eta_{Step} = \frac{P_{Step}}{P_{LED}} = (NA)^2 \qquad \textbf{Equation 16}$$

When the LED diameter is larger than the fiber core diameter, the coupling efficiency is given by [22],

$$\eta_{Step} = \left(\frac{r_{core}}{r_{LED}}\right)^2 (NA)^2 \qquad \textbf{Equation 17}$$

where r_{core} is the radius of the step-index fiber core d r_{LED} is the radius of the LED. The importance of the numerical aperture is seen by the acceptance angle shown in Figure 13.

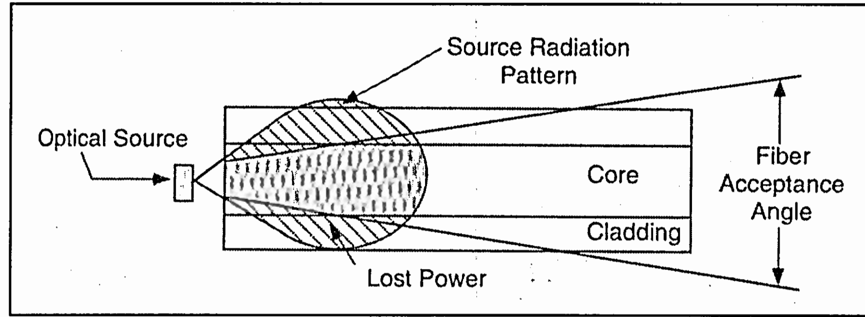

Figure 13: LED coupling into a step-index multimode fiber [22].

The power coupled to into a graded-index fiber is quite different from that coupled into a step-index fiber because the fiber numerical aperture varies as a function of radial coordinate, r. Generally, the core index of refraction deceases as the radial distance from the center of the fiber increases. The local NA for graded-index fiber is defined as [22],

$$NA(r) = \begin{cases} \left[n^2(r) - n_2^2\right]^{1/2} & for\ r \le r_{core} \\ 0 & for\ r > rcore \end{cases} \qquad \textbf{Equation 18}$$

where $n(r)$ is defined by [22],

$$n(r) = \begin{cases} n_1\left[1 - 2\Delta\left(\frac{r}{r_{core}}\right)^{\alpha}\right]^{1/2} & for\ 0 \le r \le r_{core} \\ n_2 & for\ r \ge r_{core} \end{cases} \qquad \textbf{Equation 19}$$

and Δ is defined by [22],

$$\Delta = \frac{n_1^2 - n_2^2}{2n_1^2} \qquad \textbf{Equation 20}$$

where α is a dimensionless parameter that defines the shape of the index profile [22]. Therefore, power coupled from an LED into a graded-index fiber is given by [22],

$$P_{graded} = \pi B_o \int_0^{r_{LED}} \int_0^{2\pi} (NA(r))^2 \, d\phi \, r dr$$

$$= 2\pi^2 B_o \int_0^{r_{LED}} \left[n^2(r) - n_2^2\right]^{1/2} r dr$$

$$= 2\pi^2 r_{LED}^2 B_o n_1^2 \Delta \left[1 - \frac{2}{\alpha + 2}\left(\frac{r_{LED}}{r_{core}}\right)^\alpha\right] \qquad \textbf{Equation 21}$$

The coupling efficiency is given by [22],

$$\eta_{graded} = \frac{P_{graded}}{P_{LED}} = 2n_1^2 \Delta \left[1 - \frac{2}{\alpha + 2}\left(\frac{r_{LED}}{r_{core}}\right)^\alpha\right] \qquad \textbf{Equation 22}$$

For optical communications requiring bite rates less than 200 Mbps, multimode fiber-coupled and LEDs are the best combo. The frequency response of an LED is limited by its diffusion capacitance, which is due to the storage of injected carriers in the active region of the diode [22]. The optical power varies as a function of frequency, ω, and is given by [22],

$$P(\omega) = P_o \left[1 + (\omega \tau_{eff})^2\right]^{-1/2} \qquad \textbf{Equation 23}$$

where P_o is the power emitted at a zero modulation frequency and τ_{eff} is the effective carrier lifetime. τ_{eff} is given by [22],

$$\tau_{eff} = \tau \left\{ \frac{\sinh(d / L_D) + (L_D S / D)(\cosh d / L_D - 1)}{[(L_D S / D)^2 + 1] \sinh(d / L_D) + (2 L_D S / D) \cosh(d / L_D)} \right\} \qquad \textbf{Equation 24}$$

where τ is the carrier lifetime, d is the active layer thickness, L_D is the diffusion length with diffusion coefficient D, and S is the interfacial recombination velocity. The 3-dB modulation bandwidth $\Delta\omega$ is given by [22],

$$\Delta\omega = \frac{1}{\tau_{eff}} \quad \textbf{Equation 25}$$

A closed-closed form approximation of the transient response of high-radiance double-heterojunction LEDs has been derived that assumes that the junction space charge capacitance C_s varies much more slowly with current than the diffusion capacitance C_d and can therefore be considered a constant. With this assumption, the rise time to the half-current point of the LED is given by [22]

$$\tau_{1/2} = \frac{C_s}{\beta I_p} \ln \frac{I_p}{I_s} + \tau \ln 2 \quad \textbf{Equation 26}$$

where $\beta = q/(2k_B T)$, I_p is the amplitude of the current function used to drive the LED, and I_s is the saturation current. This equation indicates that an increase in current gives a reduction in rise time. Another equation relating the recombination lifetime to the current density and the active region width, d, shows that the lifetime can be reduce by increasing the current density, J. The recombination lifetime is given by [15]

$$\tau_r = \left(\frac{qd}{JB_r} \right)^{1/2} \quad \textbf{Equation 27}$$

where B_r is the band-to-band recombination in units of cm^3s^{-1}.

2.2.2.2 Vertical Cavity Surface Emitting Lasers

Vertical cavity surface emitting lasers (VCSELs) are very attractive for a number of reasons. The VCSEL surface emitting geometry makes it a great candidate for many applications such as arrays and optically integrated elements for parallel optical processing [28], [29]. Basically, a VCSEL is a laser with its mirrors on the top and bottom surfaces, forming a vertical cavity. With this arrangement, the electric field is in the same direction as the mode propagation [15]. The advantage of using a vertical cavity configuration as opposed to a cleaved cavity configuration is that the cavity length is smaller, which means that the frequency separation between the modes increases. This leads to better modal purity [15]. However, since the round trip distance is reduced, the gain is also reduced. Therefore, the threshold current density increases. Having high reflectivity mirrors can lessen this problem.

The operation of a semiconductor laser is very similar to that of an LED. However, for all lasers, stimulated emission and optical feedback are necessary. Under forward bias, large numbers of electrons and holes are injected into opposite sides of the p-n junction depletion region. In most semiconductor lasers, the electron injection is larger than the hole injection, since the electron injection efficiency is higher for the same amount of applied bias. Also the mobility of electrons is higher than that of holes. For example, the electron and hole mobilities for GaAs are 8500 cm^2/V-sec and 400 cm^2/V-sec, respectively [19]. These factors make conditions for population inversion possible. A population inversion exists when the population of excited atoms exceeds the population of ground state atoms. Population inversion in a semiconductor laser is a little different from other types of lasers. However, just as in other lasers, the rate of

stimulated emission must still be greater than the absorption rate for inversion. Stated mathematically,

$$R_{st} > R_{abs} \qquad \textbf{Equation 28}$$

where R_{st} and R_{abs} are the stimulated emission rate and the absorption rate, respectively. For a semiconductor this condition is achieved when

$$F_n - F_p > h\nu > E_g \qquad \textbf{Equation 29}$$

where F_n and F_p represent the electron and hole quasi-Fermi levels, respectively, h is Planck's constant, ν is the photon's frequency, E_g is the bandgap energy [18], [19]. The difference in the quasi-Fermi levels is equal to the applied forward bias. In order to achieve lasing, two conditions are necessary: (1) the gain must at least be equal to the loss; and (2) the radiation must be coherent [15]. The combination of the cavity and the stimulated emission produces coherent light. The gain can be calculated by analyzing the light intensity for one roundtrip within the semiconductor cavity. The intensity is given by [15]

$$I = I_o R_1 R_2 e^{2(g-\gamma)l} \qquad \textbf{Equation 30}$$

where I_o is the initial intensity, R_1 and R_2 are the reflectivities of mirror 1 and mirror 2, respectively, g is the gain, l is the length of the cavity, and γ is the loss. When the round trip gain is equal to the loss,

$$I = I_o$$

and

$$1 = R_1 R_2 e^{2(g_{th}-\gamma)l}$$

Solving for the threshold gain, g_{th} yields [15],

$$g_{th} = \gamma + \frac{1}{2l}\ln\left(\frac{1}{R_1R_2}\right)$$ **Equation 31**

The threshold current is given by [15],

$$J_{th} = \frac{8\pi\nu_0^2 q d\tau_r n_r^2 \Delta\nu}{\tau c^2}\left(g_{th}\right)$$ **Equation 32**

where ν_o is the frequency corresponding to the spontaneous emission spectrum, $\Delta\nu$ is the linewidth of the spontaneous emission spectrum, d is the active layer thickness, τ_r is the spontaneous recombination lifetime, and n_r is the semiconductor refractive index.

The output of a laser consists of a large number of discrete frequency components. These discrete components are called longitudinal modes of the cavity. The mirrors at the end of the cavity establish a standing wave in the laser cavity resonator with wavelength, λ, which satisfies [15]

$$l = \frac{m\lambda}{2n_r}$$ **Equation 33**

where l is the length of the cavity, n_r is the semiconductor refractive index, and m is an integer called the mode number. The frequency separation between adjacent modes is given by [15]

$$\delta\nu = \frac{c}{2n_r l}$$ **Equation 34**

Another parameter of importance is the linewidth of the individual modes. The linewidth of an optical cavity is given by $\Delta\omega \cong$ (photon lifetime)$^{-1}$which is proportional to (cavity length)$^{-1}$ [9]. The linewidth is also directly dependent on the spontaneous emission rate. The spontaneous emission rate of a laser near threshold is given by [20]

$$R_{spon} \sim \frac{n}{4\tau_o}$$ **Equation 35**

and the radiative lifetime at inversion is given by [20]

$$\tau \sim \frac{\tau_o}{4}$$ **Equation 36**

where τ_o is the lifetime for typical LED operating conditions.

2.2.2.3 Resonant Cavity Enhanced Light Emitting Diodes

The emitter used in this research is a double heterojunction GaAs-based resonant cavity enhanced light emitting diode (RCE LED). The spectral characteristic of an RCE LED lies between the spectral characteristics of a surface emitting LED and a VCSEL. However, the basic operation of an RCE LED is the same as that of a surface emitting LED. The optical properties of RCELEDs are superior to that of conventional LEDs, but the complexity of the fabrication process is very similar [30], [31], [32]. The superiority of its optical properties is due to the placement of the active region in an optical cavity, where the optical cavity mode is in resonance with the spontaneous emission of the active region [30].

There are many advantages in placing the active region in an optical cavity. One advantage is the ability to enhance the spontaneous emission [30]. The probability of spontaneous emission is proportional to the optical mode density, and the optical mode density in an optical cavity is significantly enhanced for on-resonance wavelengths [30]. A dramatic change in spontaneous emission lifetime also results from the placement of the active region of an LED in a resonant optical cavity. For high finesse optical cavities, change in the spontaneous emission lifetime is a factor of 10 or greater [30].
Another advantage of placing the active region in an optical cavity is that the emission of the light through the top mirror or surface is increased due to the light that is reflected off of the highly reflective bottom mirror/contact. Unlike RCELEDs, conventional LEDs have anisotropic light emission [30]. Due to the fact that the top mirror reflectivity is less than that of the bottom mirror, RCELEDs are isotropic with most of the light that propagates along the optical axis exiting the top surface [30].

Improved spectral purity is another advantage of RCELEDs over LEDs. The density of states in the conduction band and valence band and the thermal energy of the carriers determine the spectra linewidths of conventional LEDs [30]. An LED linewidth is usually around 1.8 *kT*, where *kT* is thermal energy. Spectral purity can be improved with RCELEDs due to the fact that the spontaneous emission from the active region is constrained to emit in the modes of the optical cavity. The Q-factor of a co-planar Fabry-Perot cavity is given by [33]

$$Q = \frac{\nu}{\Delta \nu} = 2\pi \frac{L_c}{\lambda}\left(-\ln\sqrt{R_1 R_2}\right)^{-1} \qquad \textbf{Equation 37}$$

where L_c is the cavity length, and $\Delta\nu$ and ν are the linewidth and cavity resonant frequencies, respectively. R_1 and R_2 are the reflectivities of the top and bottom mirrors, respectively. Given a Q factor of 120, a reflectivity product of 0.9 and a wavelength that is equal to the cavity length, the corresponding linewidth is $h\Delta\nu$ = 12 meV which is narrower than 1.8 *kT (eV)*. This improvement in spectral purity is important for optical communications because it leads to less chromatic dispersion. The pulse broadening due to chromatic dispersion is given by [34]

$$\Delta\tau \approx \left(\frac{1}{c}\frac{dn(\lambda_o)}{d\lambda_o}\right) l \Delta\lambda_o \qquad \textbf{Equation 38}$$

where l is the fiber length, $\Delta\lambda_o$ is the spectral width of the source, and the chromatic dispersion coefficient is the bracketed term. As can be seen from Equation 40, chromatic dispersion is the rate of change of the index of refraction of an optical fiber with respect to wavelength divided by the speed of light, c. The chromatic dispersion coefficient for λ=850 nm is approximately equal to 100 ps/(km·nm) [34].

There are two important conditions that needs to be met in order to maximize LED power and temperature insensitivity [34]:

$$(1-R_1)>(1-R_2)$$
$$and$$
$$\xi(2\alpha L_c)<(1-R_1).$$

Equation 39

The first condition states that the transmission of light through the top mirror must be greater than the transmission through the bottom mirror in order to have the majority of the light exit through the top output mirror. The second condition states that the round trip cavity absorption loss, $2\alpha L_c$, must be less than the transmission of light through the top output mirror. The factor ξ is an intensity enhancement factor that is between 1 and 2, where a value of 1 is given for thick active regions, and a value of 2 is given for a thin active region placed in an electric field antinode of the cavity's standing wave [54]. The second condition is needed to ensure that self absorption does not negate the enhancement created by the resonant cavity and that there is a significant amount of output power. The peak intensity enhancement factor is given by [34]

$$G_e=\frac{\xi}{2}\frac{\left(1+\sqrt{R_2}\right)^2(1-R_1)}{\left(1-\sqrt{R_1R_2}\right)^2}\frac{\tau_{cav}}{\tau_o}$$

Equation 40

where τ_{cav} and τ_o are the lifetimes with and without a cavity. This formula assumes that there is no reabsorption of the light by the active material of the cavity, which is a good assumption for thin active regions.

2.2.3 Photodetectors

2.2.3.1 PIN Photodetectors

The most commonly used photodetection device is the junction photodiode. The basic principles of operation for a junction diode are as follows: (1) the diode is reversed biased, which results in a small reverse saturation current; (2) the incident photons are absorbed, mainly in the depletion region, and excess electron-hole pairs are generated; (3) the photogenerated carriers in the depletion region drift in opposite directions because of the reverse bias, thus, creating a photocurrent [9]. There are several types of junction diodes. One that is of interest to this research is the p-i-n (or PIN) photodiode.

The PIN photodiode is a junction diode in which a nominally undoped or intrinsic region is sandwiched between a p^+ and n^+ region as shown in Figure 14. The intrinsic (i) region does not have to be truly intrinsic as long as it is has low doping. This nominally undoped region can be either p^- or n^-, depending on the method used to form the junction.

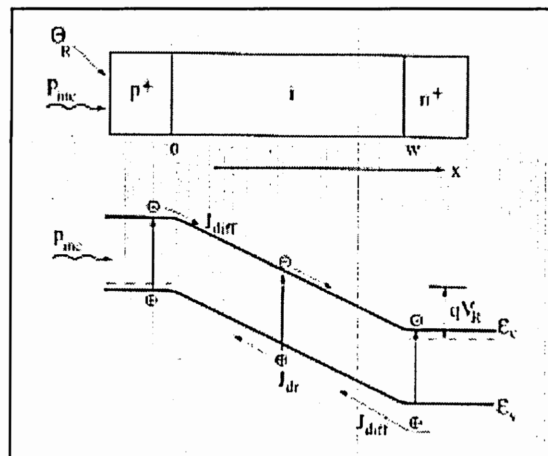

Figure 14: PIN photodetector with energy band diagram [9].

Because of the low carrier density in the intrinsic region, which leads to a high resistivity, the majority of any applied bias will drop across the i-region, which is fully

depleted at zero or low reverse bias [9], [51]. The advantage of a PIN photodiode is that it has a "controlled" depletion region or width, which can be tailored to meet the requirements of photoresponse and bandwidth [9]. By increasing the thickness of the intrinsic region, the photoresponse can be enhanced. However, increasing the thickness of the active region reduces the bandwidth. This photoresponse-bandwidth tradeoff limits the amount of tailoring that can be done.

Since there is no internal optical gain under normal operation of a PIN photodiode, the maximum quantum efficiency is 100%. Therefore, the gain-bandwidth product of a PIN with maximum quantum efficiency only depends on the bandwidth of the device. The bandwidth is usually limited by the carrier transit time or by external circuit parameters such as input resistance and input capacitance [9]. The transit time of carriers across the depletion region depends on the width of the region and the carrier velocity. By reducing the thickness of the intrinsic region, the transit time can be reduced. However, there is a trade off between transit time and quantum efficiency as previously stated. For optimal speed performance usually the transit time, t_{tr}, is restricted to [9]

$$t_{tr} = \frac{1}{2}(\text{modulation period}) \qquad \textbf{Equation 41}$$

and

$$t_{tr} = \tau_{RC} \qquad \textbf{Equation 42}$$

where τ_{RC} is the RC time constant of the device, which is dependent on the junction capacitance of the device.

The photogenerated current consists of two components: (1) drift current; and (2) diffusion current. The drift current is a function of the number of photogenerated

electron-hole pairs generated in the depletion region. The generation rate, assuming 100% quantum efficiency, is given by [9]

$$G(x) = \frac{P_{inc}(1-\Theta_R)}{Ah\nu}\alpha e^{-\alpha x} \qquad \text{Equation 43}$$

where P_{inc} is the incident optical power, Θ_R is the reflectivity of the top surface, α is the absorption coefficient, h is Planck's constant, ν is the incident light frequency, and A is the cross sectional area of the junction. The drift current density, J_{dr}, is given by [9]

$$J_{dr} = -q\int_0^W G(x)dx$$

$$= -q\frac{P_{inc}(1-\Theta_R)}{Ah\nu}\left(1-e^{-\alpha W}\right) \qquad \text{Equation 44}$$

where q is the magnitude of the electron charge and W is the width of the depletion region.

Now focusing on the diffusion component of the current, minority carrier generation in the bulk regions becomes important. Since the top p^+ layer is usually transparent in a double heterojunction device, the main concern is minority carriers produced in the n^+ layer. The diffusion current density for the minority carrier holes produced in this layer is given by [9]

$$J_{diff} = -q\frac{P_{inc}(1-\Theta_R)}{Ah\nu}\frac{\alpha L_h}{1+\alpha L_h}e^{-\alpha W} - qp_{NO}\frac{D_h}{L_h} \qquad \text{Equation 45}$$

where L_h is the diffusion length for holes, D_h is the diffusion coefficient for holes, and p_{NO} is the minority concentration at a distance more than approximately $3L_h$ from the depletion region. The total current density is given by

$$J = J_{dr} + J_{diff} \qquad \text{Equation 46}$$

2.2.3.2 Metal-Semiconductor-Metal Photodetectors

The detectors used in this research are Metal-Semiconductor-Metal (MSM) photodetectors (PDs). An MSM PD is formed when two interdigitated Schottky contacts are deposited onto a nominally undoped semiconductor. The contacts are biased to create an electric field between the two contacts. When light is incident on the semiconductor, an electron hole pair is generated, and the carriers are swept to their respective contacts by the electric field. The speed and sensitivity of the MSM PD is dependent on the width of the contact fingers and the gap between them. Decreasing the gap between the interdigitated contacts can increase the speed of the device by decreasing the carrier transit time. Increasing the width of the contacts can increase the speed by reducing the gap capacitance and the contact resistance. However, there exist a tradeoff between speed and sensitivity. To increase the sensitivity, the gap between the contact fingers has to increase and the width of the contact has to decrease. This minimizes the amount of surface optical shadowing from the contacts.

This tradeoff can be avoided by back illuminating the MSM PD [63]. To optimize MSMs for speed and sensitivity, the research herein uses inverted-metal-semiconductor-metal (I-MSM) PDs [50]. Basically, an I-MSM PD is a thin film MSM PD that has been removed from its growth substrate using a substrate removal process, and the MSM is subsequently inverted and bonded to a host substrate. By inverting the MSM PD, the contact shadowing is avoided increasing the sensitivity. In addition, the contact width and the gap between the contacts can be optimized to increase the speed of the device.

A photomicrograph of a conventional MSM PD with its interdigitated fingers is shown in Figure 15.

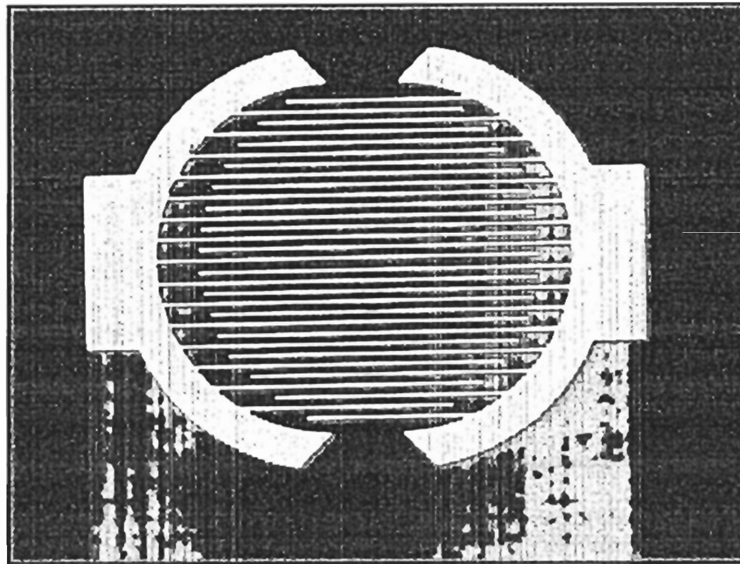

Figure 15: Metal-Semiconductor-Metal Photodetector.

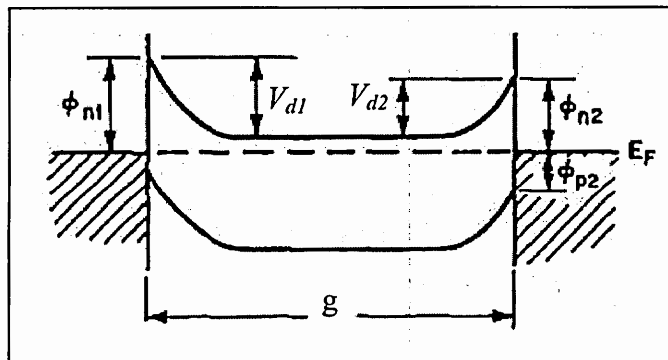

Figure 16: Equilibrium band diagram of MSM PD [56].

The energy band diagram for an MSM PD in thermal equilibrium is shown in Figure 16, where the electron Schottky barrier heights and built in voltages are labeled Φ_{n1} and Φ_{n2}, V_{d1} and V_{d2}, respectively. Φ_{p2} is the hole Schottky barrier height from the second contact, and g is the gap length between the contacts. A symmetric MSM PD, which means $\Phi_{n1} =$

Φ_{n2}, is formed when the metals and areas of the contacts are the same. When the device is biased, one contact (contact 1) is reversed biased and the other contact (contact 2) is forward biased.

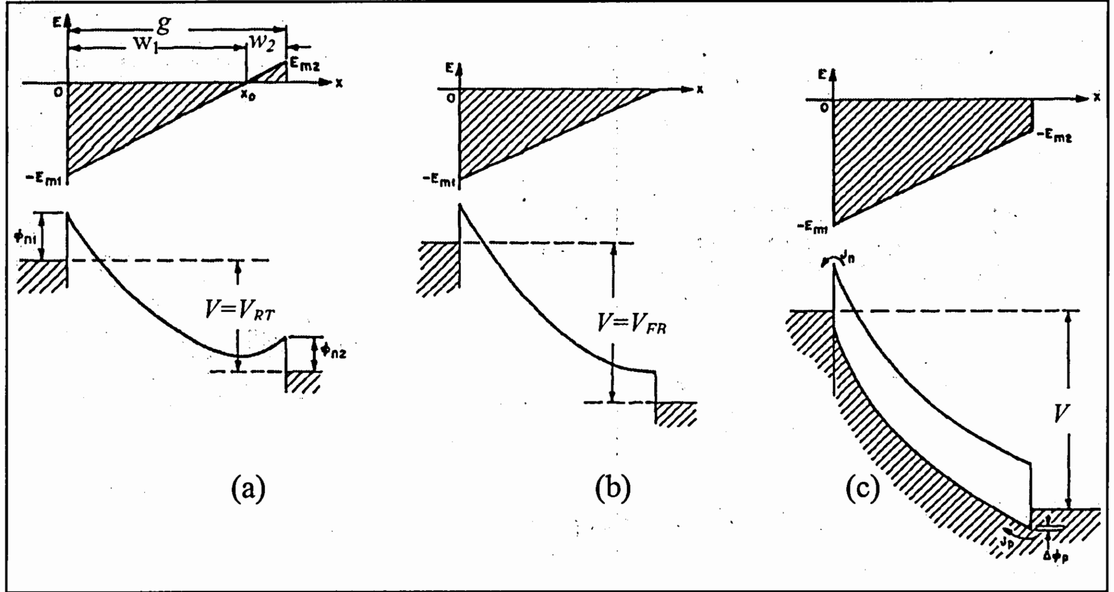

Figure 17: Band diagram and electric field plot for an MSM PD at (a) reach through voltage, (b) flat band voltage, and (c) over flat band voltage [56].

There are three regions of interest when the effects of increasing the applied voltage are studied for MSM structures. The three regions are shown in Figure 17. In the first region, as the voltage increases the sum of the depletion widths around each contact increases until it is equal to the finger gap, g. The voltage at which the two depletion regions touch is called the reach-through voltage, V_{rt}, and is given by [56]

$$V_{rt} = \frac{qN_D}{2\varepsilon_s} g^2 - (V_{d1} - V_{d2}) - g\sqrt{\left[\frac{2qN_D}{\varepsilon_s}(V_{d2} - V_2)\right]} \qquad \textbf{Equation 47}$$

where q is the magnitude of the electron charge, N_D is the donor concentration, ε_s is semiconductor dielectric constant, g is the finger gap, V_{d1} and V_{d2} are the built voltages at contact 1 and contact 2, respectively, and V_2, is the applied voltage at contact 2.

In the second region, as the voltage increases beyond the reach-through voltage, the electric field approaches zero at contact 2. When the electric field becomes zero at contact 2 the energy band becomes flat at contact 2, and the corresponding flat-band voltage, V_{FB}, is given by [56],

$$V_{FB} = \frac{qN_D g^2}{2\varepsilon_s} - (V_{d1} - V_{d2}) \qquad \textbf{Equation 48}$$

The maximum voltage that can be applied before avalanche breakdown occurs near contact 1 limits the third region. The breakdown voltage, V_B, is strongly dependent on the maximum electric field, which is approximately a constant independent of the width of the depletion region, and is given by [56]

$$V_B \cong E_{\max} g - V_{FB} - 2(V_{d1} - V_{d2}) \qquad \textbf{Equation 49}$$

The dark current that is produced when the device is biased without light incident on the detector is due to thermionic emission over the Schottky barriers [56]. When the voltage is less than the reach-through voltage, most of the current is from electron emission. As the voltage is increased past the fully depleted reach-through condition, the electron current remains small. However, the hole current from the forward biased contact begins to dramatically increase as the hole Schottky barrier is lowered, and it reaches a high level at the flat band condition. The total current densities for the three regions are defined as [56]:

Region 1. $V < V_{rt}$

$$J = A_n^* T^2 e^{-q\phi_{n1}/kT} e^{q\Delta\phi_{n1}} \left(1 - e^{-qV1}\right) + \frac{qD_p p_{no} \tanh\left[(x_2 - x_1)/L_p\right]}{L_p}\left(1 - e^{-qV_1}\right) + \frac{A_p^* T^2 e^{-q\phi_{p2}/kT} e^{-qV_{d2}}}{\cosh\left[(x_2 - x_1)/L_p\right]}\left(e^{qV_2} - 1\right) \qquad \textbf{Equation 50}$$

Region 2. $V_{rt}<V<V_{FB}$

$$J = A_n^* T^2 e^{-q\phi_{n1}/kT} e^{q\Delta\phi_{n1}} + A_p^* T^2 e^{-q\phi_{p2}/kT} \left[e^{-\frac{q(V-V_{FB})^2}{4(V_{FB}-\Delta V_d)}} - e^{-qV_{d2}} \right]$$ **Equation 51**

Region 3. $V>V_{FB}$

$$J = A_n^* T^2 e^{-q\phi_{n1}/kT} e^{q\Delta\phi_{n1}} + A_p^* T^2 e^{-q\phi_{p2}/kT} e^{q\Delta_{p2}}$$ **Equation 52**

where the A_n^* and A_p^* are the electron and hole Richardson constants, ϕ_n and ϕ_p are the electron and hole Schottky barrier height, $\Delta\phi_n$ and $\Delta\phi_p$ are the electron and hole barrier height lowering, respectively, V_{FB} is the flat band voltage, V_1 and V_2 are the applied voltages at contact 1 and contact 2, respectively, V_{d2} is the built in voltage at contact 2, ΔV_d is the difference between the built in voltages at contact 2 and contact 1, T is the absolute temperature, q is the magnitude of the electron charge, k is Boltzmann's constant, and (x_2-x_1) defines the neutral region for the holes. Low dark current, high performance GaAs MSM PDs have been relatively easy to fabricate because high electron Schottky barrier contacts ($\phi_n \sim 0.7$eV) can be readily obtained on GaAs [60]. With GaAs MSMs, metal electrode properties are just as important as semiconductor properties [49]. From the current densities, ϕ_{n1} and ϕ_{p2} exponentially influence the electron and hole injections at their respective contacts. When the same metal is used for both contacts, it is reasonable to assume that the bandgap energy is given by [49]

$$E_g \approx \phi_{n1} + \phi_{p2}$$ **Equation 53**

This relationship produces a rivalry between the electron injection and hole injection because the metal choice may affect the barrier heights differently. Low dark current MSM PDs on GaAs have been fabricated using WSi_x [49]. With this metal the barrier heights were nearly equal to $E_g/2$ [49]. Unlike GaAs, InGaAs MSM PDs have very low Schottky barriers for most metals ($\phi_n \sim 0.2eV$) [65]. There have been several approaches

taken to enhance the barrier height such as growing thin strained layers of higher barrier height GaAs and AlGaAs on InGaAs [67]. Dielectric films have also been deposited on InGaAs using a Langmuir-Blodgett technique [60]. Another approach is to grow a large band gap lattice matched InAlAs layer followed by an InAlAs/InGaAs graded superlattice [65]. InAlAs has a high Schottky barrier height of ~ 0.8eV. An attractive alternative to epitaxial growth techniques is to use Fe-doped or implanted high resistance InGaAs in place of nominally undoped InGaAs to increase the Schottky barrier height [66].

In order to achieve gigabit operation in optical communications, fast photoreceivers are needed. Fast response and high sensitivity can be achieved by reducing the input capacitance of the front-end preamplifier connected to a photodiode [75]. The MSM PD's planar interdigitated electrode structure gives the device a smaller capacitance per unit area than PINs, which means that a large MSM PD can be used with a high-impedance integrating amplifier without necessarily compromising the bandwidth [60]. In addition, a low detector capacitance benefits the receiver sensitivity because it reduces the equivalent input noise current. For example, the equivalent input noise impedance in FETs is directly proportional to the square of the total front-end capacitance, $(C_{detector} + C_{gs} + C_{stray})^2$ [60].

The ideal capacitance for a MSM structure is given by [69],[49],[59],[60],

$$C = C_o(N-1)l \qquad \textbf{Equation 54}$$

where N is the number of fingers, l is the finger length and C_o is the gap capacitance per unit length, and is given by [69]

$$C_o = \varepsilon_o(1+\varepsilon_r)K/K' \qquad \textbf{Equation 55}$$

where ε_0 and ε_r are the dielectric constant of vacuum and the relative dielectric constant of the semiconductor, respectively. K and K' are complete elliptic integrals and are given by [69]

$$K = K(k) = \int_0^{\pi/2} \frac{d\phi}{\sqrt{1-k^2 \sin^2 \phi}} \qquad \textbf{Equation 56}$$

$$k = \tan^2 \frac{\pi}{4}\left(\frac{w}{w+g}\right) \qquad \textbf{Equation 57}$$

$$K' = K(k'), \qquad k' = \sqrt{1-k^2} \qquad \textbf{Equation 58}$$

where g and w are the respective finger spacing (gap) and width. An approximation of K/K' is given by following equation [19]

$$\frac{K}{K'} = \frac{\pi}{2} \Big/ \ln\left\{2\sqrt{\frac{1+k'}{1-k'}}\right\} \quad \mathit{for} \quad 0 < k < 1/\sqrt{2} \ \ \mathit{and} \ \ 0 < K/K' < 1 \qquad \textbf{Equation 59}$$

The gap capacitance per unit area is given by [9]

$$C_{MSM} = \frac{C_o}{w+g} \qquad \textbf{Equation 60}$$

The theoretical capacitance of GaAs MSM PDs as a function of gap size using equation 62 is shown in Figure 18.

The MSM PD ideal capacitance formula may be used to compare the MSM PD capacitance to that of a conventional p-i-n PD. Typically, the capacitance of an MSM is ¼ the capacitance of a vertical p-i-n with the same light sensitive area [49]. The capacitance per unit area of a vertical p-i-n PD is given by [64]

$$C_{p-i-n} = \frac{\varepsilon_o \varepsilon_r}{d}\left[1 + \frac{d}{\pi r}\left(\ln\frac{16\pi r}{d} - 1\right)\right] \qquad \textbf{Equation 61}$$

where d is the intrinsic region thickness, which is equal to the finger spacing of the MSM PD for comparison. The second term in the formula takes into account the fringing field, where r is the detector radius. The capacitance of a GaAs PIN is shown in Figure 19.

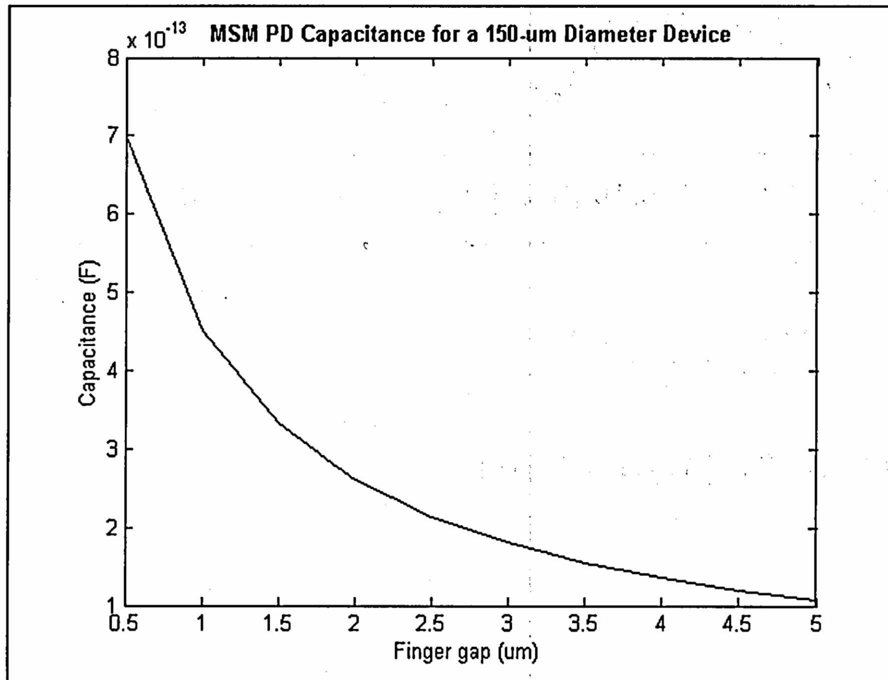

Figure 18: MSM PD capacitance versus gap size.

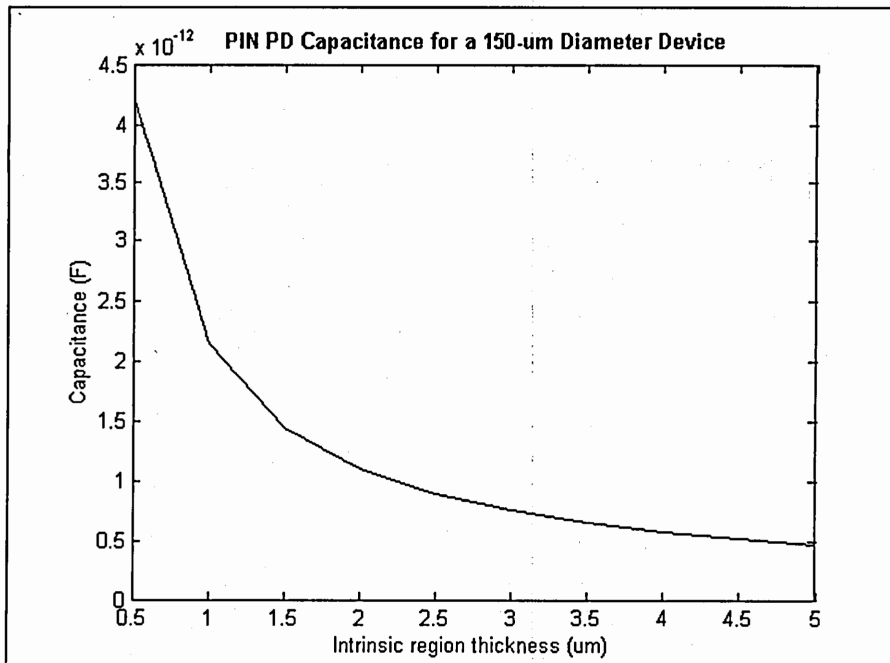

Figure 19: PIN PD capacitance versus intrinsic region thickness.

A comparison of the two types of detectors is shown in Figure 20, assuming, to enable simple capacitance comparison, that the PIN PD intrinsic region is equivalent to the MSM gap spacing. The graph indicates that for a given finger gap the capacitance is the MSM is ¼ the capacitance of a similar PIN PD, which is consistent with reported results [49].

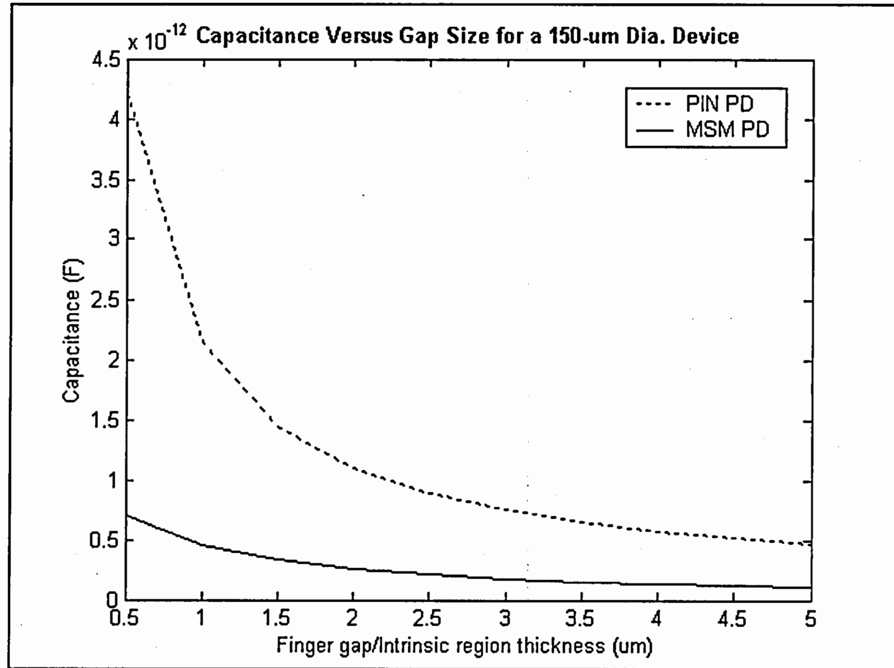

Figure 20: Capacitance comparison.

The 3 dB bandwidth, f_{RC}, is given by [62]

$$f_{RC} = \frac{1}{2\pi RC}$$ **Equation 62**

The transit time limited frequency response of the MSM PD is complex due to the variation in the electric field with depth, and holes generated deep in the semiconductor, where the electric field is weakest, have longer transit times [64]. However, a one-dimensional approximation, which assumes that the carriers travel at a constant saturation

velocity, can be used to calculate the 3 dB bandwidth, f_{tr}. This approximation is valid when the electric field is high enough to saturate the carrier velocity throughout the absorption region, and the absorption thickness is smaller than the finger spacing [62]. In this approximation, the transit time is taken as the time required to travel one-half of the gap. The transit time and its frequency response is [62]

$$t_{tr(msm)} = \frac{g}{2v_s} \quad and \quad f_{tr} = \frac{1}{2\pi t_{tr}} \qquad \textbf{Equation 63}$$

where v_s is the saturation velocity and g is the finger gap spacing. Figure 21 indicates that a 200 μm diameter device is RC time limited when the finger gap is less than 3.25 μm, and transit time limited when it is greater than 3.25 μm. A gap width of 3.25 μm would yield the optimum response time. The resistance was assumed to be 50 ohm.

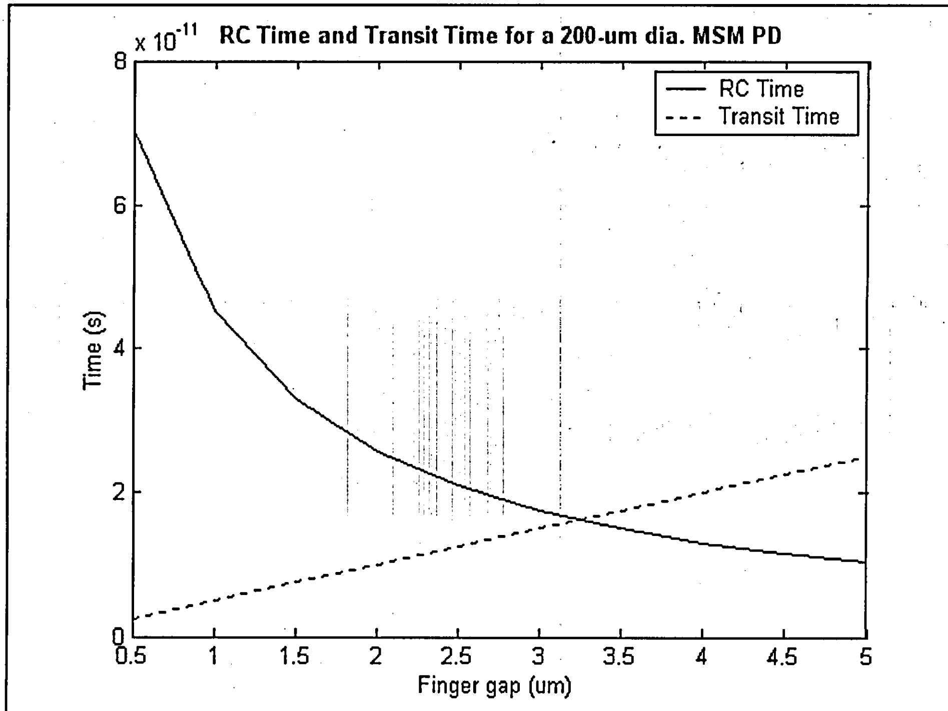

Figure 21: 200 μm diameter MSM PD RC and transit time using a 50 ohm load.

The optimal finger gap changes with detector size. Figure 22 and Figure 23 shows that for a 150 μm and 120 μm diameter MSM PD, the optimal finger gap is 2.5 μm and 2 μm, respectively.

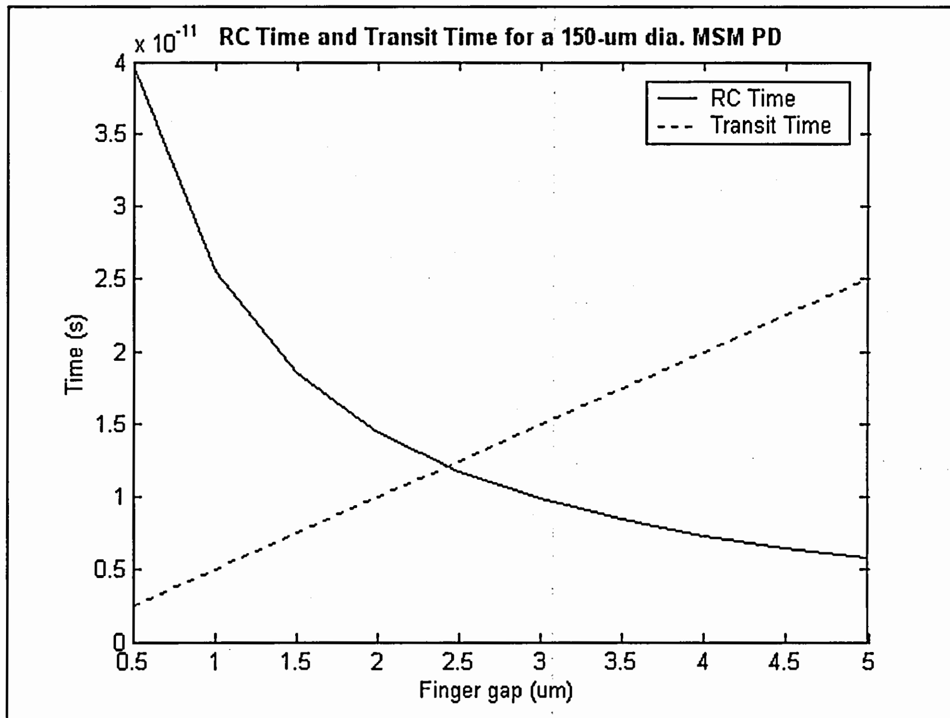

Figure 22: 150μm diameter MSM PD RC and transit time using a 50 ohm load.

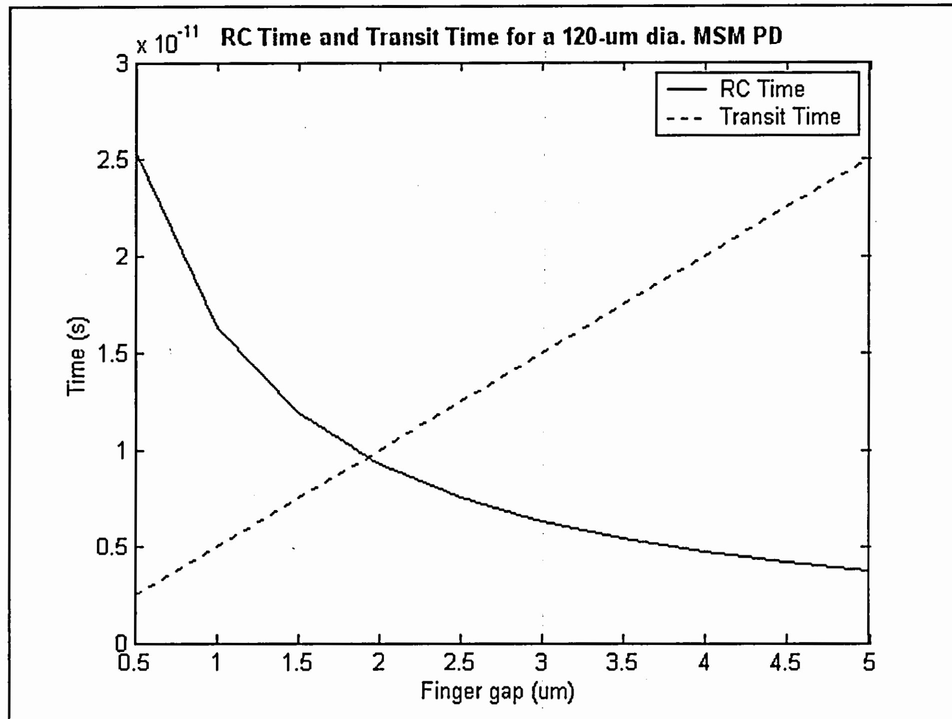

Figure 23: 120 μm diameter MSM PD RC and transit time using a 50 ohm load.

A first order approximation of transit time for PIN PDs is usually calculated by dividing the intrinsic region thickness by the saturation velocity [76],[19]. This approximation assumes a constant carrier velocity, which implies that the device is fully depleted. The PIN transit time is given by [76]

$$t_{tr(pin)} = \frac{d}{v_s}$$ **Equation 64**

where d is the intrinsic region thickness and v_s is the saturation velocity. This result is comparable to the MSM PD transit time, when the time is taken as the time required to travel half the gap, instead of the entire depletion region. Thus, the overall 3 dB bandwidth of these detectors is a function of the RC time constant and transit time, and is given by [62]

$$f_{3dB} \approx \frac{1}{2\pi\sqrt{t_{tr}^2 + (RC)^2}}$$ **Equation 65**

Figure 24 shows the frequency response of the MSM and PIN photodetectors, assuming that the PIN PD intrinsic region thickness is equivalent to the MSM PD gap spacing.

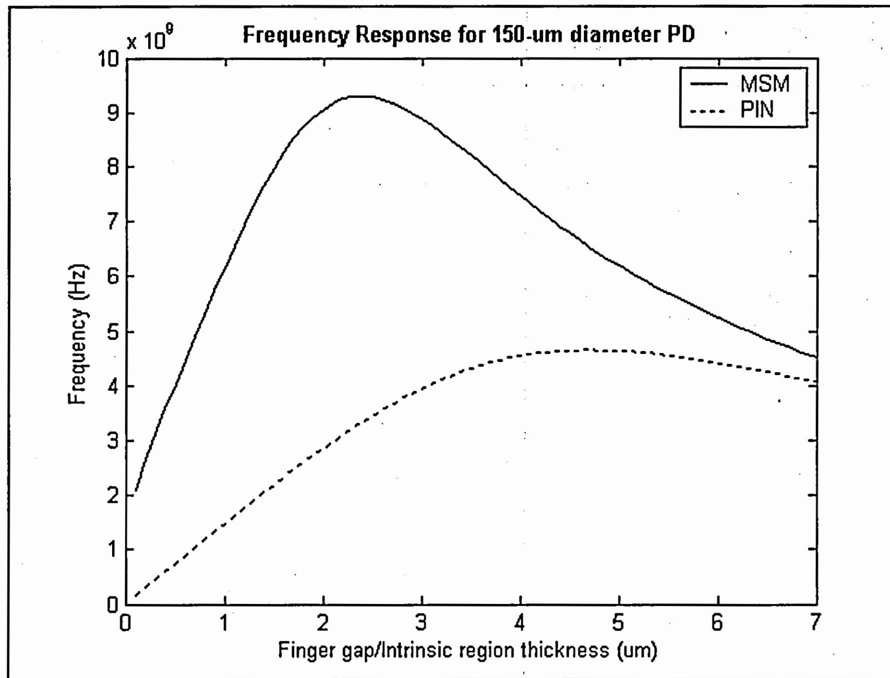

Figure 24: Frequency response of photodetectors.

This graph was generated with η set to unity and v_s set to $1\text{x}10^7$ cm/s for GaAs, and the transit time was taken as the time to travel one-half of the depletion region [62]. According to the graph the maximum MSM frequency of 9 GHz is achieved when the finger gap is 2 to 3 μm for a 150 μm diameter GaAs MSM PD.

Another point of comparison between the MSM and PIN PDs is the responsivity. The responsivity, R, of a photodetector is given by [9]

$$R = \eta_{ext} \frac{q}{h\nu}$$ **Equation 66**

where q is the magnitude of the electric charge, h is Planck's constant, ν is the frequency of the incident light, and η_{ext} is the external quantum efficiency. The external quantum efficiency of a conventional MSM PD is limited by the finger size and spacing, and is given by [9], [60], [68]

$$\eta_{MSM} = \eta_i (1 - \Theta_R) \left[\frac{g}{g+w} \right] (1 - e^{-\alpha d}) \qquad \textbf{Equation 67}$$

where η_i is the internal quantum efficiency, which is the number of electron hole pairs created divide by the number of photons absorbed by the semiconductor, α is the absorption coefficient, and d is the absorption depth. The reflectance of an uncoated semiconductor surface in air, Θ_R, is given by [52]

$$\Theta_R = \left(\frac{1 - n_s}{1 + n_s} \right)^2 \qquad \textbf{Equation 68}$$

where n_s is the refractive index of the semiconductor. The external quantum efficiency of a vertical PIN PD is not limited by finger shadowing and is given by [64]

$$\eta_{PIN} = \eta_i (1 - \Theta_R)(1 - e^{-\alpha d}). \qquad \textbf{Equation 69}$$

To eliminate the reduction in external quantum efficiency (EQE) for the MSM PD due to opaque fingers, transparent electrodes have been used [71]. In addition, an antireflection coating such as SiN_x has been used to decrease the reflectance. Indium-tin-oxide (ITO) is a transparent material that has a high-electrical conductivity, a low optical absorption coefficient at λ = 850nm, and forms a good Schottky contact on GaAs [71]. Devices that have utilized SiN_x antireflection coating with ITO electrodes have reportedly shown EQEs of ~0.8 at 5V [71]. One drawback to ITO contacts is the high absorption coefficient at long wavelengths (1.3μm to 1.55μm). This is why it is rarely used with

long wavelength detector materials such as InGaAs [38]. However, by back-illuminating a SiN_x-coated InGaAs/InAlAs MSM PD, the typical responsivity of 0.45 A/W can increase to about 0.96A/W with a 1.5 μm absorption layer thickness [63]. Inverted-MSM PDs (I-MSM PDs) with absorption thickness of approximately 1 μm and an antireflection coating has demonstrated a responsivity of 0.7 A/W [50].

2.3 Thin Film Fabrication and Integration Techniques

Optoelectronic integrated circuits (OEICs) are comprised of microelectronics, and optoelectronic (OE) devices such as light emitters and photodetectors. An OEIC enables the processing of complicated optical information, which makes it useful for a plethora of applications. Some applications using OEICs include: free space optical interconnection of multichip modules, fiber-optic communication with or without wavelength division, visible laser projection displays, digital laser printing and scanning, and reading and writing of optical memory [77]. The challenge of integrating digital and analog microelectronics with optoelectronics has produced different approaches for realizing an OEIC. One approach is monolithic integration [36], [37], [78]. In this approach, the OE, optical, and microelectronic devices are all integrated in material grown on a single substrate. This technique has the potential for high density, low on-chip power dissipation, and low cost [77]. However, it is incompatible with silicon microelectronics since silicon is an indirect band gap semiconductor, which makes it an inefficient light emitter and photodetector. Another approach uses heterogeneous integration techniques [39], [40], [41], [79], [80], [81]. The heterogeneous approach enables the integration of dissimilar materials. Therefore, this approach has the advantage of the integratibility of silicon microelectronics with direct bandgap semiconductors. With the integration of low cost silicon circuitry and optoelectronics, the desired functionality of an OEIC can be achieved without sacrificing cost, yield, or reliability [41].

2.3.1 Hybrid Integration Techniques

There are three established hybrid integration techniques: (1) flip chip bonding; (2) bridge bonding; and (3) wire bonding. Flip chip, or bump bonding, is an approach in which a semiconductor device, array, or IC has metal "bumps" applied to electrical interconnections, this "bumped" sample is subsequently inverted and bonded to another substrate with metallized interconnections, such as a high intraconnect substrate or IC. The main advantage of flip chip bonding is that a large number of connections can be made with one flip of the bumped substrate onto the bump bonding pads, which is good for high-density arrays [77]. Also high-speed operation is possible because of the short length and large area electrical interconnections. However, since the flipped optoelectronics devices are not mounted to the die, it has a low efficiency for heat dissipation [77]. Most of the heat is dissipated via air cooling.

The second approach is the bridge bonding technique. This integration technique is similar to flip chip bonding. However, there is a bridge that is bonded to the optoelectronics and circuitry, which bridges the two devices together forming an OEIC. Since both devices are bonded to the die in this approach, the heat dissipation is maximized. Also high-density arrays are still possible. Due to the long metal thin film leads needed to bridge the devices, however, the OEIC speed is limited by the RC time constant [77].

This is also the case with the third integration approach, wire bonding. The main advantage to wire bonding is the suitability for top and bottom light emission and detection from the optoelectronic devices. Heat dissipation is also maximized in this

approach. The wire bonding pads can consume a lot of chip area and is not usually used for bonding high-density arrays [77].

Flip chip bonding, bridge bonding, and wire bonding integration approaches have been around for years and as a result are very mature. Another promising approach for integrating semiconductor devices with microelectronics, both electronic and optoelectronic, is the thin film device integration technique [41]. When the substrate is removed in the flip chip integration process, it can also be classified as a thin film integration method. Other thin film integration techniques that have not been discussed are the epitaxial liftoff (ELO), appliqué, and fluidic assembly methods. While each method has its unique approach, the integration usually comprise of four main steps: (1) fabrication of III-V device, (2) transfer of the device to host substrate, (3) bonding to the host substrate, and (4) removal of III-V device substrate [82]. A comparison of these methods is shown in Table 2.

Table 2: Integration Methods

Integration Method	III-V Fabrication	Substrate Removal	Epilayer Transfer	Bonding to Silicon
Flip Chip	Before Transfer	After Transfer	Substrate	Bump Bonding
ELO & Modified ELO	Before &/or After Transfer	Before or After Transfer	Free Standing or on a Membrane	Van der Waals or metallic bond
Appliqué	Before Transfer	Before Transfer	Free Standing or Fluidic Carrier	Metallic bond
Fluidic Assembly	Before Transfer	Before Transfer	Fluidic Suspended	Van der Waals

2.3.2 ELO Integration Technique

The ELO integration method was used in the late 1980's to remove GaAs from its growth substrate [42], [84]. This process is feasible because AlAs that is lattice matched to GaAs has a high etch rate in hydrofluoric acid (HF). The selectivity of HF is ~10^7 to 1 in etching AlAs to GaAs, and thus, a high Al concentration etch layer can be laterally etched to separate epilayers of interest from the growth substrate. The first step in the ELO process is to grow a sacrificial high Al concentration AlGaAs layer on a GaAs substrate. The sacrificial layer of $Al_xGa_{1-x}As$ is limited to values of $x < 0.6$ and is usually 100 Å to 2000 Å thick [41]. Next, the GaAs epilayer, which is the material of interest for optoelectronics or electronic devices, is grown on top of the sacrificial layer. The device is fabricated using standard processing. The sample is then coated with black wax and immersed in HF, which attacks the high Al concentration AlGaAs layer. As the etching continues the tension from the black wax causes the epi-layer to curve, which aids the etching process by allowing more reaction to take place between the HF and high Al concentration AlGaAs. The epi-layer is finally released and bonded to a host substrate.

To assist in the integration to silicon circuitry and in the use of material systems other than GaAs, modifications were made to the standard ELO process. A modified ELO process includes a transfer diaphragm technique that serves as an intermediate host substrate before transferring the device to its final substrate [41]. It also uses a total substrate removal process, in which etching away the substrate instead of a sacrificial layer separates the epilayer. This modification makes the integration of InP based

material possible. The ELO thin film integration processes have been used to transfer MSM and pin photodetectors, LEDs, and edge-emitting lasers [41].

2.3.3 Appliqué Integration Technique

Another thin film device integration technique that is used to transfer GaAs devices is the appliqué process [79], [82]. The name appliqué means that a small patch of material is bonded to a larger piece of material. The growth process for each device begins with an oxide free GaAs buffer layer. This is followed by an AlAs stop etch layer. Next, the smoothing layers are grown, which are intended to help achieve a smooth bottom surface after substrate removal. A thick GaAs layers is grown, followed by the top epilayer. Next the devices are fabricated and tested to make sure the devices are functioning properly before transferring them. The sample is pattern with photoresist and etched with 1N $K_2Cr_2O_7$:1 HBr:1 CH_3COOH until the devices are etched below the smoothing layers. The sample is then bonded to a glass slide with the device side down on the glass. The substrate is then mechanically lapped to a thickness of about 100 μm. The remaining material is etched away using NH_4OH:H_2O_2 until the AlAs stop etch layer is reached. The selectivity of the etchant is 30:1 GaAs over AlAs. Next, the smoothing layers are removed. The back of the epilayer is metallized with Pd-Ge-In-Sn contacts. The sample is removed from the glass slide and transferred to a host substrate using a mechanical probe. Light pressure is applied while the sample is being annealed to maintain contact. This process has been used to transfer pin photodiodes, MESFETs, and VCSELs [79], [82].

2.3.4 Fluidic Assembly Integration Technique

The last approach discussed is the fluidic assembly thin film integration technique. Fluidic assembly is a micromechanical process for transferring microscopic devices on one substrate to another, host, substrate [85], [86], [87]. This process begins with the growth of a sacrificial AlAs layer grown on a GaAs substrate, followed by the epilayer device growth. The top surface is then metallized with the appropriate ohmic contacts such as AuGe/Ni/Au. A photoresist mask is patterned over the sample. The devices are then ion milled into trapezoidal blocks. The trapezoidal blocks are separated from their growth substrates by placing them in an HF solution. The etch solution is then diluted with water and subsequently replaced with ethanol, which serves as a carrier assembly fluid. Next, the host substrate is prepared by etching trapezoidal holes that will serve as integration sites. The sidewall angles of the host substrate are fabricated such that there is a 2-3μm gap around the trapezoidal blocks. The bottoms of the host substrate holes are metallized to form contacts and bonding sites. The substrate is then placed in the carrier assembly fluid. The blocks fall into the holes and the ethanol carrier fluid is evaporated in a bake oven at 70°C. The substrate is planarized using SiO_2 and polyimide. A via is etch and the top contact is deposited. The integration process has been used to integrate thin film LEDs and VCSELs [85], [86], [87].

CHAPTER 3

FABRICATION AND INTEGRATION

3.1 SiO_2 Coated Silicon Integration

3.1.1 Thin Film GaAs RCE LED Fabrication and Integration

The LED structure used in this research was a simple double heterostructure PpPnN: GaAs (20nm, contact layer)/AlGaAs (1000nm, cladding layer)/GaAs (1000nm, Active layer)/AlGaAs (1000nm, cladding layer)/GaAs (20nm, contact layer) with a 200 nm AlAs sacrificial etch layer grown between the device layers and the GaAs substrate. To fabricate the thin film RCE LED, the modified epitaxial lift off (ELO) process was used as described earlier [40]. First, AuZn/Au (1000 Å/1500 Å) was deposited onto the semiconductor, which served as an ohmic p-contact and, after being patterned, as a square or circular mesa mask. The LED material was mesa etched down to the AlAs layer using H_2SO_4:H_2O_2:H_2O (1:8:200). The LEDs were coated with Apiezon W and placed in 10% HF, which selectively laterally etched the AlAs and released the devices from their growth substrates [42]. The LEDs embedded in Apiezon W were then bonded to a transparent Mylar diaphragm, and the Apiezon W was then removed using trichloroethylene. Next, the LEDs were transferred to a SiO_2-coated silicon host substrate by using the transparent diaphragm to align the thin film device over the bond pads, and water tension to remove and bond the device to the host substrate [19]. To increase the strength of the bond, the samples were heated at 200°C for 6 minutes to allow the bottom contact metal from the LED and the metal from the bonding site to form a metal-to-metal bond. The bonded devices were then coated with a layer of

benzocyclobutene (BCB), which serves as an isolation layer between the top and bottom contact. The BCB was then cured at 250°C for 1 hour. A thin layer of SiO_2 was deposited to increase the adhesion of the top contact. A via was opened over the LEDs. Next, AuGe/Ag/Au/Ti/Al (1000 Å/1000 Å/1500 Å/300 Å/1000 Å) was deposited, which serves as an n-type ohmic top contact. The BCB was removed using a reactive ion etch (RIE) in O_2:SF_6 gas. The Ti/Al metal layers served as mask during the etching process. The Ti/Al layer was removed using 351 Developer and HF. Finally, the device was annealed at 200° C. Figure 25 shows the LED integration process.

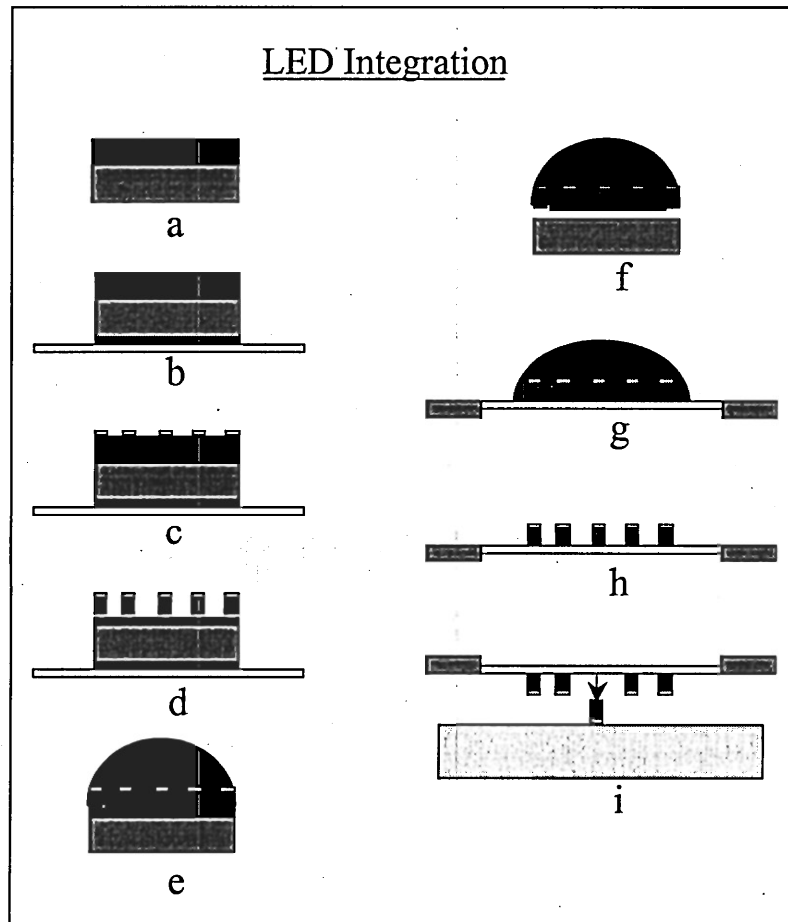

Figure 25: LED thin-film integration process.

3.1.2 Thin Film I-MSM Photodetector Fabrication and Integration

The I-MSM PDs were fabricated using both GaAs and InGaAs semiconductor material. The GaAs I-MSM PD material structure was a 1-micron undoped GaAs layer grown on an AlAs sacrificial etch layer on a GaAs substrate. The MSM PD was fabricated using standard photolithography, followed by metal deposition, and a lift-off process to define the Schottky contacts. The Schottky contact was Pt/Ti/Pt/Au (50 Å/200 Å /200 Å/2200 Å). Square or circular mesas were patterned over the devices, which served as masks during the mesa etching. The GaAs was then mesa etched down to the AlAs layer using H_2SO_4:H_2O_2:H_2O (1:8:200). The MSM PDs were coated with Apiezon W and placed in 10% HF, which selectively etched the AlAs and released the devices from their growth substrates. The devices embedded in Apiezon W were bonded to a transparent Mylar diaphragm, where the black wax was removed using trichloroethylene.

The InGaAs I-MSM PD structure consisted of a heterostructure grown lattice matched to an InP substrate with a stop etch layer. The growth consisted of: InP (substrate)/InGaAs (200 nm, stop etch layer)/InAlAs (40 nm)/InGaAs (50 nm, grade layer)/InGaAs (7400 nm, absorption layer)/InGaAs (50 nm, grade layer)/InAlAs (40 nm), with all layers nominally undoped. The MSM PD was fabricated using standard photolithography, followed by metal deposition, and a lift-off process to define the Schottky contacts. The Schottky contact was Pt/Ti/Pt/Au (50Å/400Å/400Å/2200Å). Square or circular mesas were patterned over the devices, and serve as masks during the mesa etching. The InGaAs was mesa etched down to the InP layer using citric acid:H_2O_2:H_2O (140:10:50). The MSM PDs were then coated with Apeizon W and placed in HCl:H_2O (2:1) to remove the InP substrate. The I-MSMs embedded in Apiezon

W were then bonded to a transparent Mylar diaphragm, and the Apiezon W was removed using trichloroethylene.

Once the MSMs were bonded to the transfer diaphragm, they were ready to be transferred to a SiO_2-coated silicon host substrate. The devices were aligned over their contact pads by using a transparent diaphragm and metal-metal bonded. The devices were then annealed at 200°C for 6 minutes. The I-MSM PD integration process is shown in Figure 26, and an I-MSM PD bonded to a SiO_2-coated silicon substrate is shown in Figure 27.

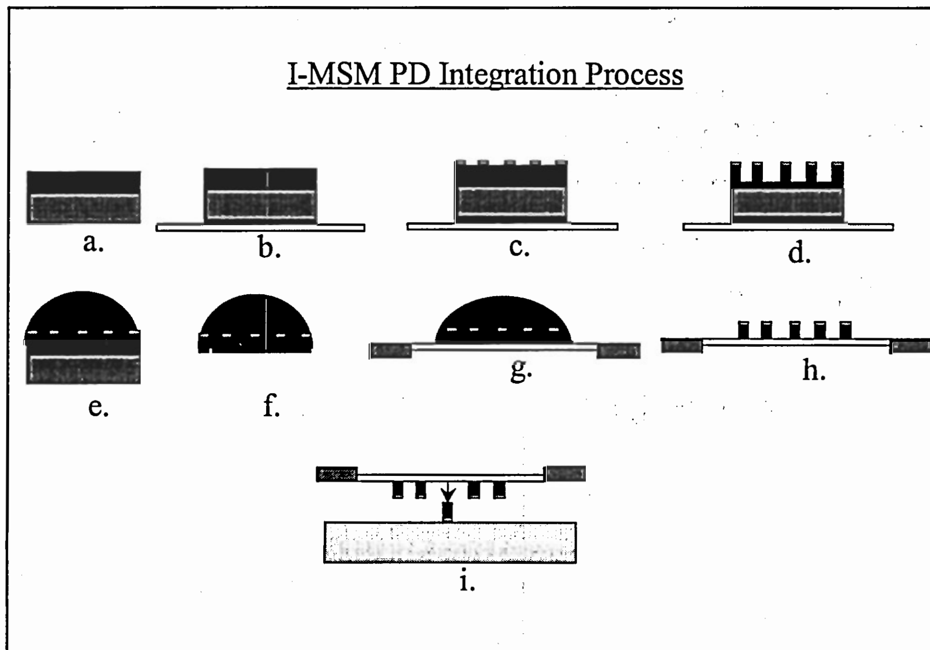

Figure 26: I-MSM PD thin film integration process.

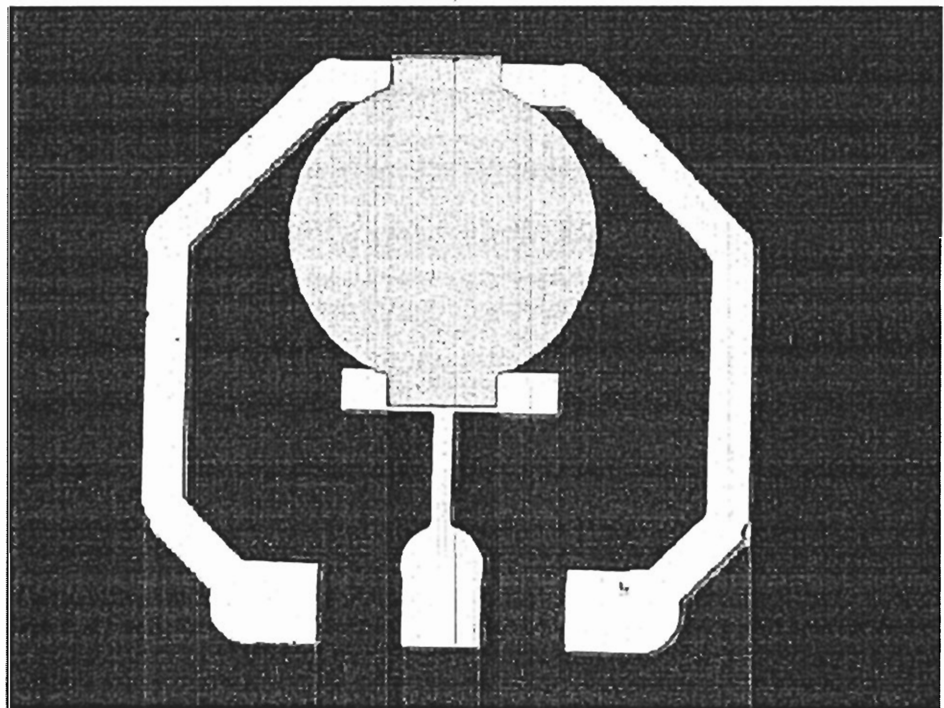

Figure 27: Thin film GaAs I-MSM PD integrated onto SiO_2-coated silicon.

3.2 Integration onto CMOS Circuits

3.2.1 Integration of RCE LEDs Onto CMOS Circuits

Thin film RCE LEDs were fabricated as described in section 3.1.1, and integrated onto Si CMOS circuits. After defining and depositing the LED bottom contact pads on the circuits, the LED were integrated onto the pads. The metal scheme used for the bottom contact on the silicon substrate was Ti/Au/Pt/Ti/Al/Ti/Pt/Au. The Al was used to protect the bottom contact during the removal of the BCB, and the Ti/Pt served as a diffusion barrier between the gold and aluminum, which form intermetallics at temperatures at or above 250°C [47]. Next, a photodefinable BCB isolation layer was spun on, and photolithography was performed to open vias over the top contact pad and the LED. The thickness was approximately 3.4 μm. The top contact of the LED was defined and deposited with a circular 30 μm diameter aperture. The metallization was AuGe/Ag/Au/Ti/Al. Finally, all of the remaining exposed BCB was removed using the RIE with SF_6:O_2. The circuit with integrated LED is shown in Figure 28. The luminescence versus current (LI) curve is shown in Figure 29. The measure power was 1.8 μW at 25 mA and the turn on voltage was 3.5 V.

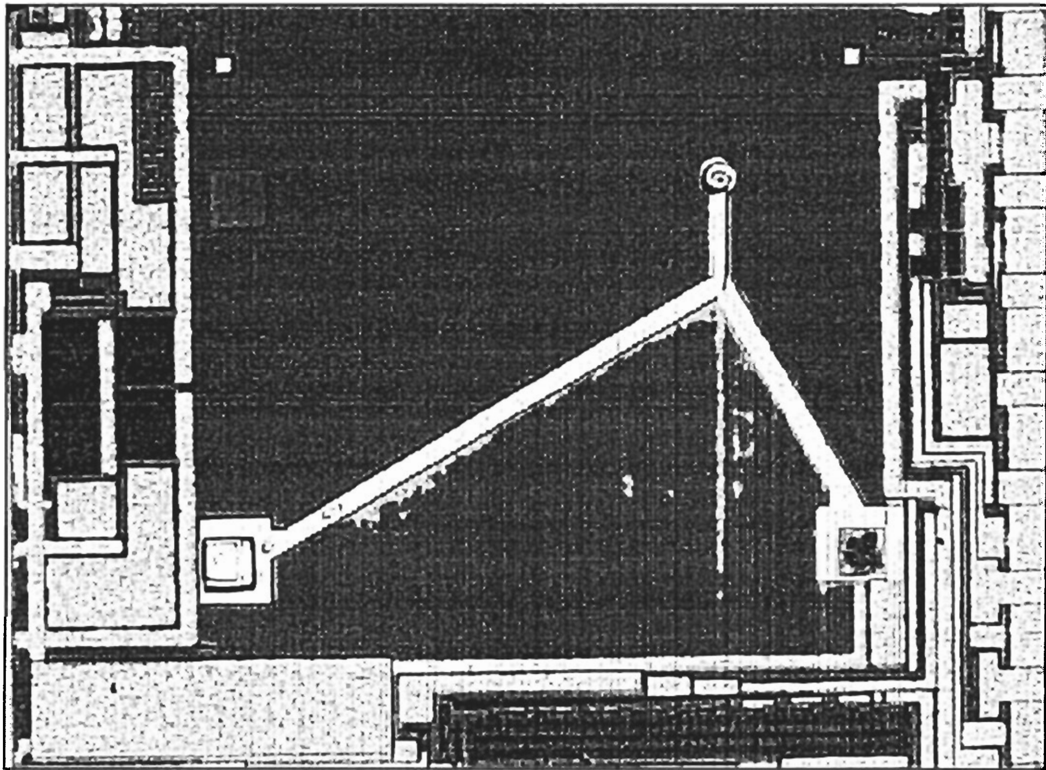

Figure 28: RCE LED integrated onto a CMOS circuit.

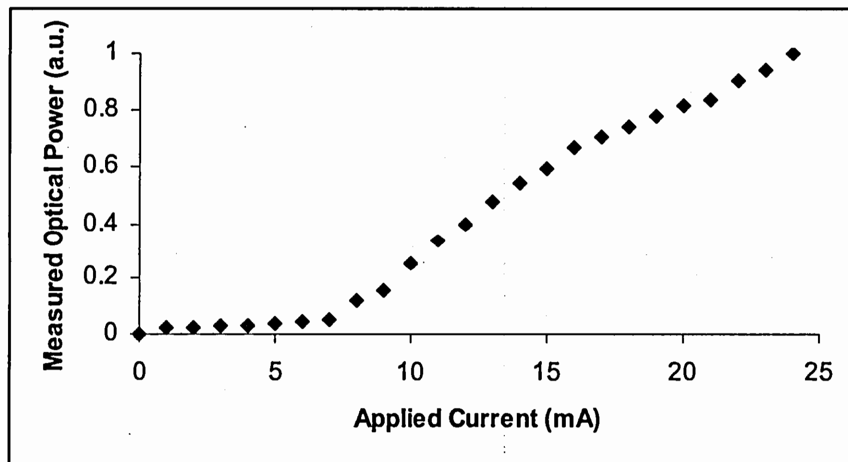

Figure 29: LI curve for 50 μm RCE LED.

3.2.2 Integration of I-MSM PDs onto CMOS Circuits

InGaAs I-MSM PDs were fabricated as described in section 3.1.2, and subsequently bonded to silicon CMOS circuits. The I-MSM PDs were bonded onto Ti/Au pads on the silicon CMOS circuits, and dc characteristics were measured to verify that the devices operated properly. Then, a layer of BCB was spun on and cured at 240 °C for 1 hour, with a resulting thickness of approximately 1.7 μm. This was done to increase the adhesion of the I-MSM PD to the bonding pads. The BCB was etched away using an RIE with SF_6:O_2 gas. The integrated I-MSM PD on a CMOS circuit is shown in Figure 30 and the measured eye diagram at 1 Gbps is shown in Figure 31.

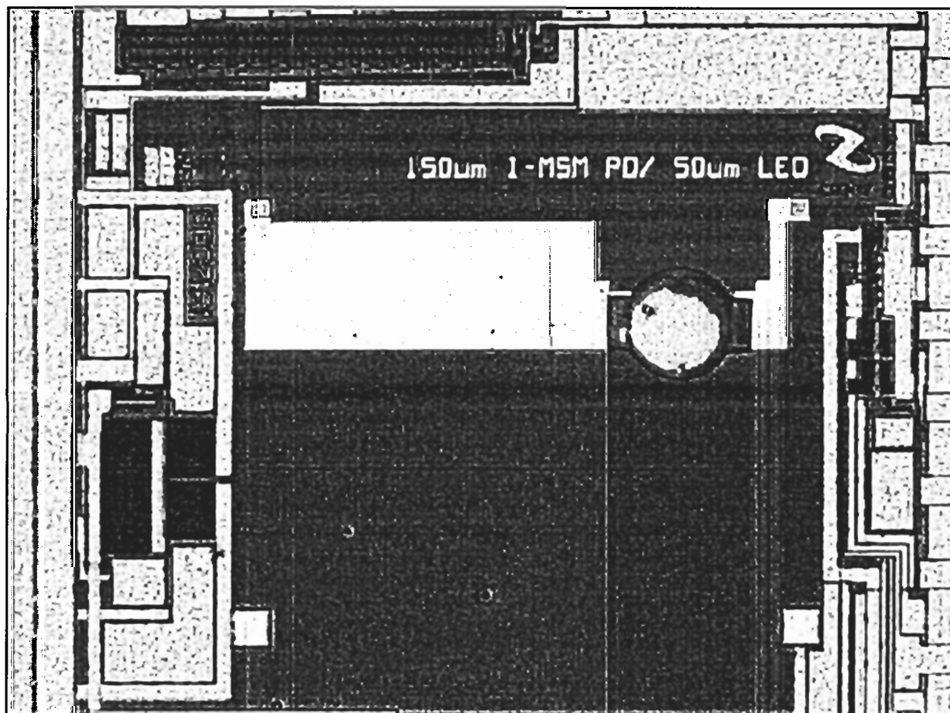

Figure 30: I-MSM PD integrated onto a CMOS circuit.

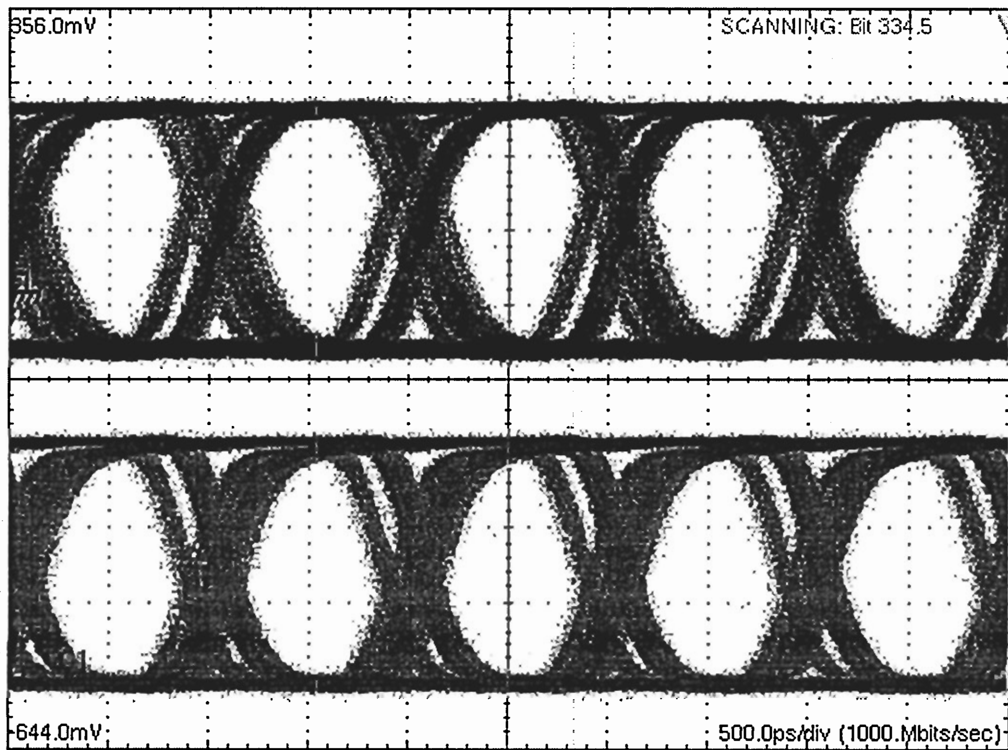

Figure 31: Eye diagram of I-MSM PD receiver operating at 1 Gbps.

3.3 3D Stacked Thin film Integration

3.3.1 3D Stacked Thin film I-MSM PD/RCE LED on Silicon

The last two sections highlighted the fabrication of a heterogeneous transmitter and a heterogeneous receiver. To demonstrate a heterogeneous thin film transceiver, a process for stacking thin film RCE LEDs and I-MSM PDs was developed. However, before integrating the 3D stacked devices onto silicon CMOS transceiver circuits, the devices were integrated on to SiO_2-coated silicon substrates.

To build the 3D stacked thin film structure, an I-MSM PD was bonded to the Ti/Au contact pads that were deposited onto nitride or SiO_2-coated silicon. Then, the first benzocyclobutene (BCB) isolation layer was spun on and cured at 240 °C for 1 hour, with a resulting thickness of approximately 1.7 μm. A thin adhesion layer of SiO_2 was then deposited on the BCB using plasma enhanced chemical vapor deposition (PECVD). After depositing and defining the LED bottom contact pad in the center of the thin film bonded I-MSM, the LED was integrated onto the pad. The metals used for the bottom contact were Ti/Au/Pt/Ti/Al/Ti/Pt/Au. The Al was used to protect the bottom contact during the removal of the BCB, and the Ti/Pt served as a diffusion barrier between the gold and aluminum. Next, a second BCB isolation layer was spun on and cured, with a resulting thickness of approximately 3.4 μm. A thin SiO_2 adhesion layer was deposited using PECVD. A circular contact window with a diameter of 40 μm was etched open using a reactive ion etch (RIE) with SF_6:O_2. The top contact of the LED was defined and deposited with a circular 30 μm diameter aperture using AuGe/Ag/Au/Ti/Al. Finally, all of the remaining exposed BCB was removed using RIE with SF_6:O_2. The 3D stacked device process is shown in Figure 32.

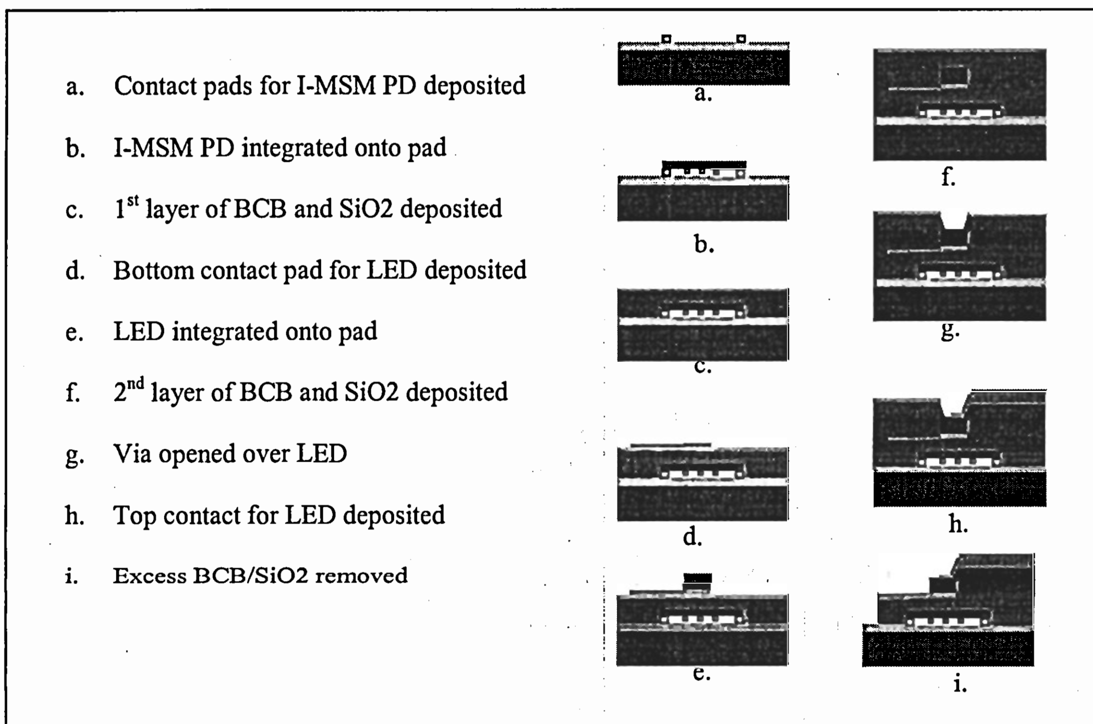

Figure 32: 3D Stacked thin film process.

3.3.2 Measurement Setup For 3D Stacked Device Tests

After fabricating the 3D stacked thin film device, the emitter and detector were tested separately to verify functionality. The main functionality test for photodetectors is the current versus voltage (IV) curve. The IV curve is measured with and without incident light. The dark current measurement is the measurement without light. The responsivity is calculated by measuring the photocurrent as a function of incident light. To measure these currents, a probe station is used to contact the device. A Labview controlled source measurement unit (SMU) supplies the voltage and measures the current. An HP lightwave multimeter is used to illuminate the detector. The photodetector DC test setup is shown in Figure 33.

An important emitter test is the luminescence versus current (LI) measurement. This is considered the single most important characteristic of a LED [15]. To measure the LI curve, a probe station with DC probes is used to contact the device. An ILX current source is used to supply the current. The output light is coupled into a large core multimode fiber, which is connected to a silicon detector. An SMU reads the detected power. A labview computer program controls the current source and SMU. The LI curve measurement setup is shown in Figure 34.

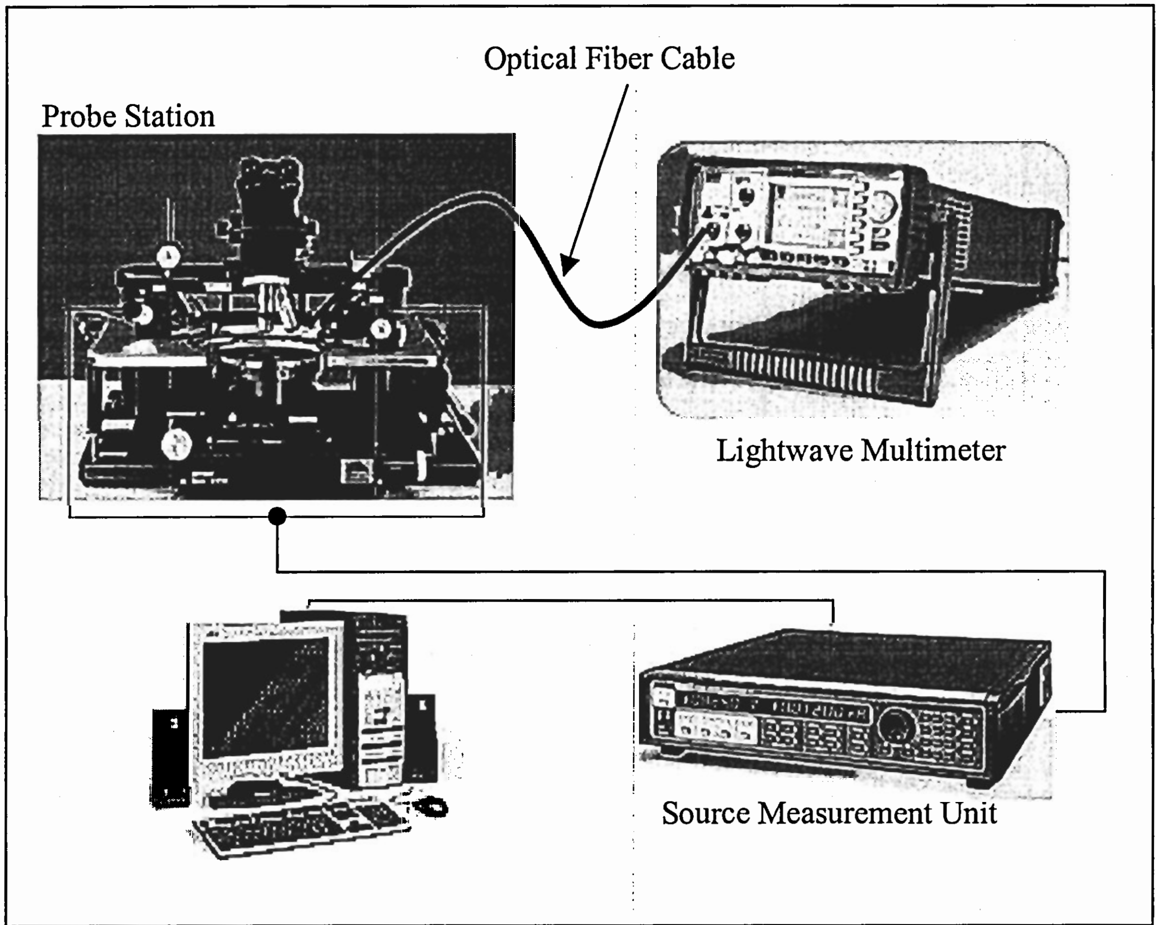

Figure 33: I-MSM PD DC measurement setup

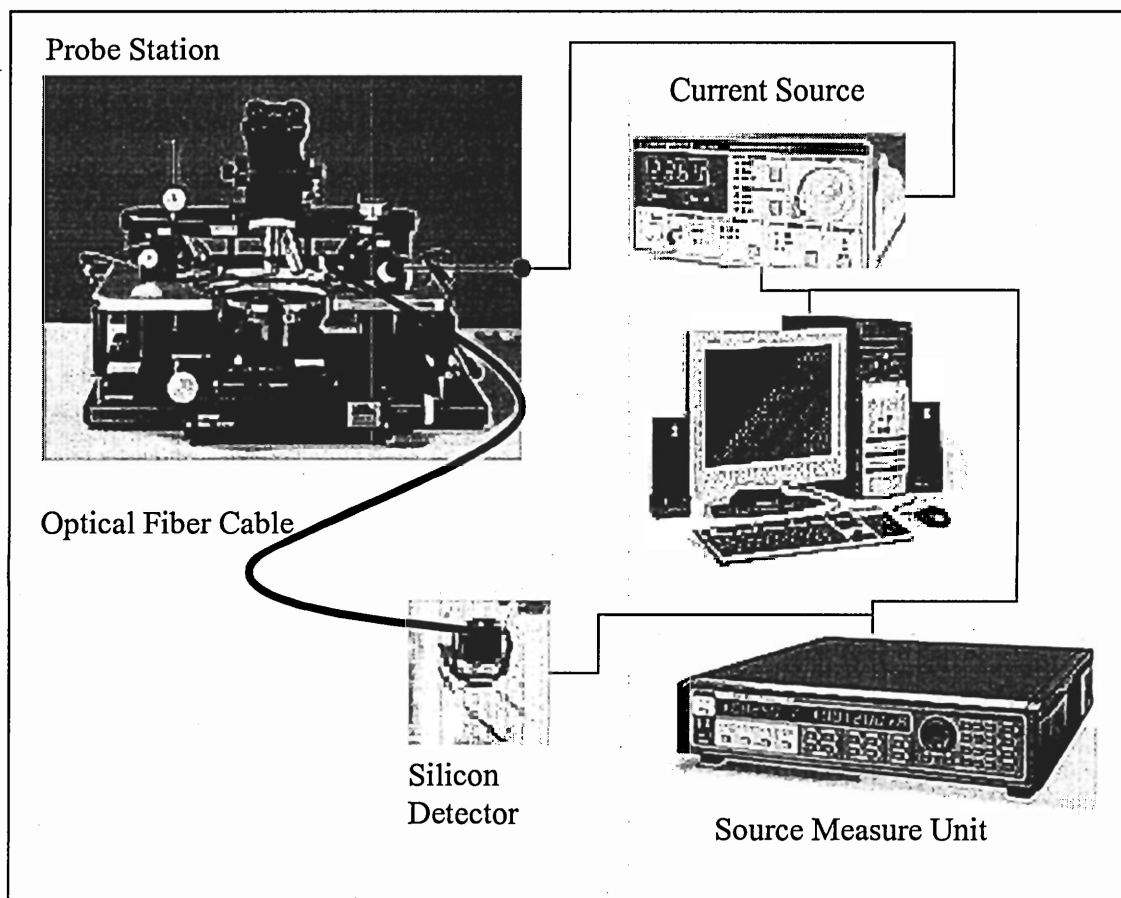

Figure 34: RCE LED LI measurement setup

3.3.3 Square 3D Stack Device: GaAs LED on top of GaAs I-MSM PD

Square shaped 3D stacked thin film devices integrated onto SiO_2-coated silicon substrates were fabricated as described in section 3.3.1. This was the first demonstration of 3D stacked thin film devices. To fabricate the square 3D thin film stacked device for bi-directional optical links, a thin film GaAs-based I-MSM PD and a thin film GaAs-based LED were independently grown, fabricated into devices, and bonded onto a SiO_2-coated host substrate. The I-MSM PD material was a 1-micron undoped GaAs layer grown on an AlAs sacrificial etch layer. MSM fingers were defined and deposited, followed by etching of 300 x 300 μm^2 square mesas. The LED was a double heterostructure PpN AlGaAs/GaAs/AlGaAs with an AlAs sacrificial etch layer. AuZn served as an ohmic p-contact, and 100 μm x100 μm mesas were defined. Both devices were then separated from their growth substrate using thin film integration and a transfer diaphragm as described in sections 3.1.1 and 3.1.2, and were bonded to the host Si substrate, which had contact pads deposited onto it [19]. The I-MSM was integrated onto the pads on the SiO_2 first. After verifying that the device worked properly, the first benzocyclobutene (BCB) isolation layer was spun on and cured. After defining the LED bottom contact pad, the LED was integrated onto the pad that was centered in the middle of the I-MSM PD. A second BCB isolation layer was spun on and cured, and a contact window was opened, followed by top contact deposition and definition. Finally, the excess BCB was removed.

The dark current and photocurrent of the I-MSM PD is shown in Figure 35. The I-MSM PD dark current was 68 nA and the responsivity was 0.11 A/W. The LI curve of

the LED is shown in Figure 36. A picture of the co-located stacked thin-film device is shown in Figure 37.

The square 3D stacked device was the first demonstration of stacking two active thin film devices. The I-MSM PD dark current was acceptable for a 300 μm x 300 μm detection area. The dark current increases with increased detection area. The low responsivity was a result of the LED shadowing and material selection. The LI curve showed that the LED was operating properly.

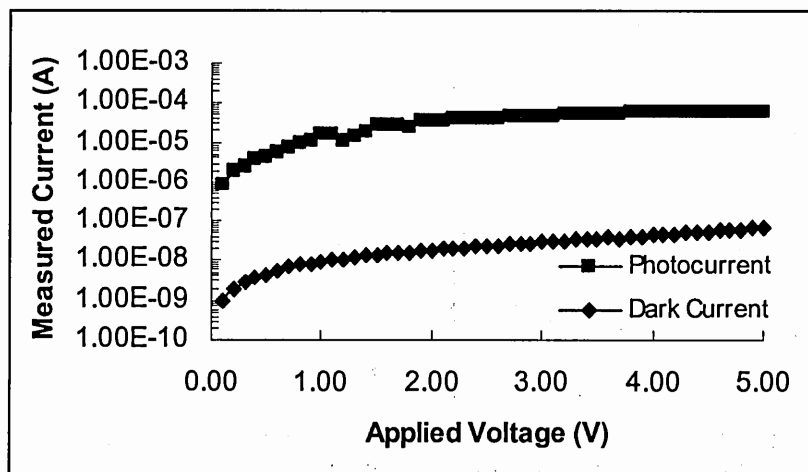

Figure 35: Measured currents for a square I-MSM PD.

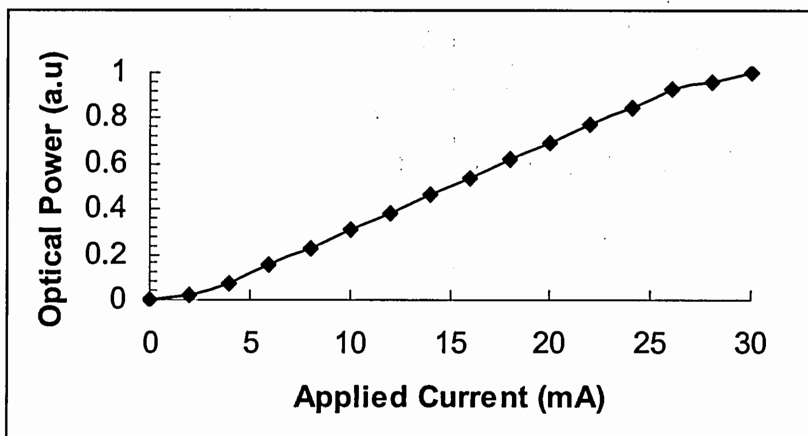

Figure 36: LI curve for a square LED.

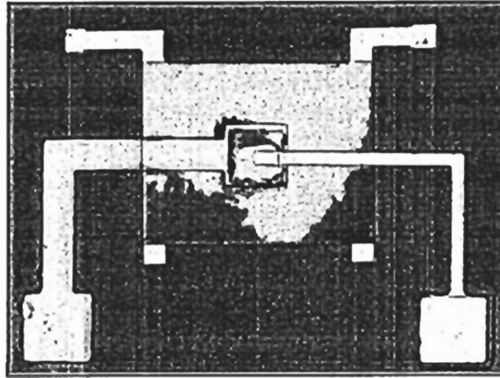

Figure 37: Top view of a square thin film 3D stacked device.

3.3.4 Circular 3D Stack Device: GaAs LED/GaAs I-MSM PD

In order to match the 3D stacked device geometry to the circular geometry of optical fibers, the 3D stacked thin film devices were made in a circular geometry. By matching the two structures, the theoretical coupling efficiency calculations were simplified. Moreover, with the square structure for the PD, the corners of the device could not receive light unless the device was overfilled. However, with the circular structure the beam could completely fill the device without overfilling. Moreover, the smaller area of the circular device reduces the capacitance by a factor of 79% [62]. To fabricate the circular 3D stacked device, a thin film GaAs-based I-MSM PD and a thin film GaAs-based LED were independently grown, fabricated into devices, and bonded onto a SiO_2-coated host substrate. The I-MSM PD material was a 1 μm undoped GaAs layer grown on an AlAs sacrificial etch layer. The MSM PD was fabricated using standard photolithography, followed by metal deposition, and a lift-off process to define the Schottky contacts, as shown in Figure 38a. The Schottky contact was Ti/Au (250 Å/2200 Å). Circular mesas with a diameter of 280 μm were patterned over the devices, which served as masks during the mesa etching. The GaAs was mesa etched down to the AlAs layer using H_2SO_4:H_2O_2:H_2O (1:8:200). The LED was a double heterostructure PpN AlGaAs/GaAs/AlGaAs with an AlAs sacrificial etch layer. AuZn/Au (1000 Å/1500 Å) served as an ohmic p-contact and, after being patterned, as circular mesa etch masks with a diameter of 50 μm. The LED material was mesa etched down to the AlAs layer using H_2SO_4:H_2O_2:H_2O (1:8:200). Both MSM PDs and the LEDs were coated with Apiezon W and placed in 10% HF, which selectively etched the AlAs and released the devices from their growth substrates. The devices embedded in Apiezon W were bonded

to a transparent Mylar diaphragm, where the black wax was removed using trichloroethylene (TCE).

The I-MSM PD was integrated onto the Ti/Au pads on the SiO_2 first. After verifying that the device worked properly by testing its DC characteristics, the first BCB isolation layer was spun on and cured. The thickness was approximately 2.6 μm. The BCB was cured at a temperature of 250°C for 1 hour. A thin adhesion layer of SiO_2 was deposited onto the BCB using plasma enhanced chemical vapor deposition (PECVD). After defining and depositing the LED bottom contact pad in the center of the thin film bonded I-MSM PD, the LED was integrated onto the pad. The metal scheme used for the bottom contact was Ti/Au/Pt/Ti/Al/Ti/Pt/Au. The Al was used to protect the bottom contact during the removal of the BCB, and the Ti/Pt served as diffusion barriers between the gold and aluminum. Next, a second BCB isolation layer was spun on and cured. The thickness was approximately 3.4 μm. A thin SiO_2 adhesion layer was deposited using PECVD. A circular contact window with a diameter of 40 μm was etched open using a reactive ion etch (RIE) with SF_6:O_2. The top contact of the LED was defined and deposited with a circular 30 μm diameter aperture. The metallization was AuGe/Ag/Au/Ti/Al. Finally, all of the remaining exposed BCB was removed using the RIE with SF_6:O_2. The final co-located device is shown in Figure 38.

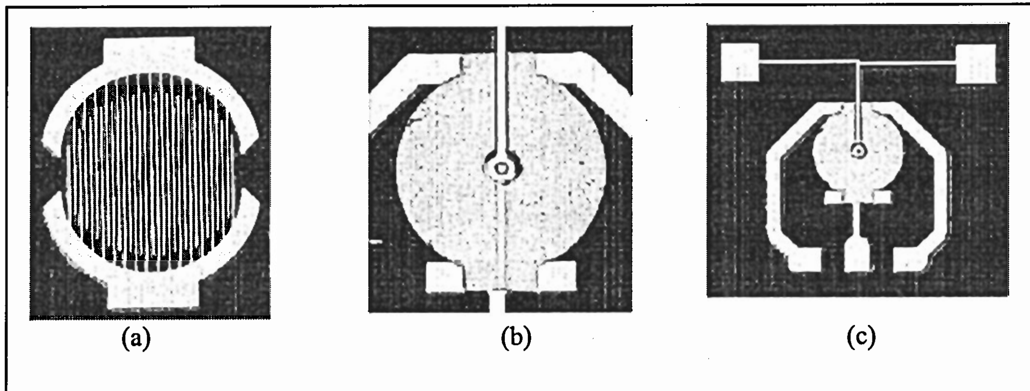

Figure 38: (a) MSM PD, (b) circular thin film 3D stack device, close-up view, and (c) 3D stacked device, showing probe pads.

The LED L-I curve was measured using an ILX Lightwave LDP-3811 precision pulsed current source. The output light was coupled into a multimode optical fiber with a core diameter of 600 μm. The other end of the fiber was FC connected to a UDT silicon photodetector with a responsivity of 0.4547 A/W at λ = 850 nm. The dark current and photocurrent of the I-MSM PD is shown in Figure 39. The responsivity of the I-MSM PD was 0.224 A/W. The LI curve of the LED is shown in Figure 40.

To simplify the theoretical coupling efficiency calculations, reduce the device capacitance, and conserve nonilluminated material, the 3D stacked structure was made in a circular geometry. The 250 μm diameter I-MSM PD had a responsivity of 0.224 A/W, which is typical of GaAs detectors. The LI curve of the RCE LED showed that the device was functioning properly.

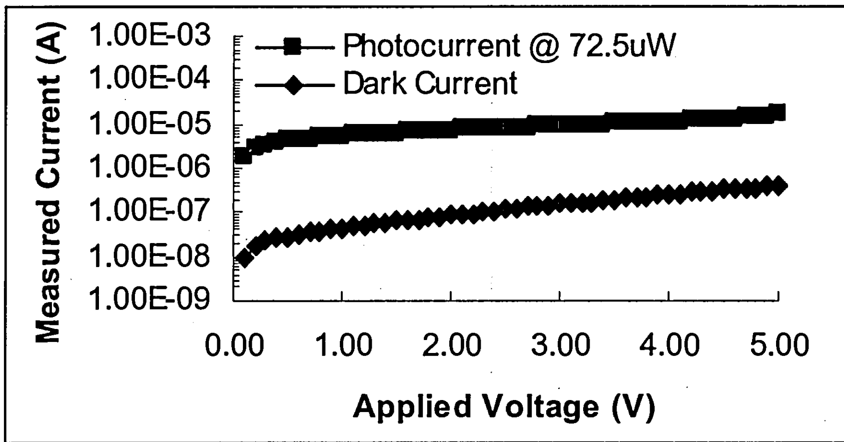

Figure 39: Current measurements for circular 3D stack.

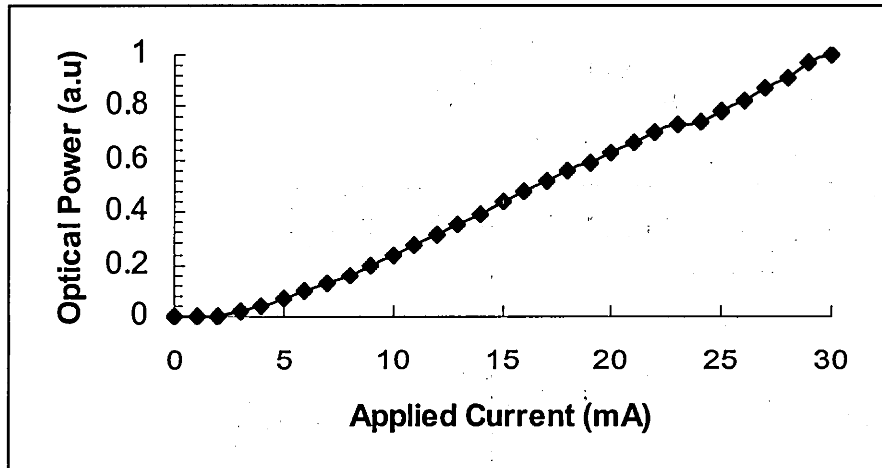

Figure 40: LI curve for circular 3D stack.

3.3.5 3D Stacked Device: GaAs LED Stacked on Top of InGaAs I-MSM PD

To optimize the photodetector for high speed operation, the PD material choice was changed from GaAs to InGaAs. It has been calculated that InGaAs has a higher low field electron mobility and saturation velocity in comparison to GaAs [48]. Due to its small band gap (~0.7 eV, lattice matched with InP), InGaAs has a broader spectral response, with detection capability at 850 nm, 1300 nm and 1500 nm wavelengths. To fabricate this asymmetric optoelectronic 3D device stack, a thin film InGaAs-based I-MSM PD and a thin film GaAs-based LED were independently grown, fabricated into devices, and bonded onto a nitride-coated silicon host substrate. The I-MSM PD structure consisted of a heterostructure grown lattice matched to an InP substrate with a stop etch layer. The growth consists of: InP (substrate)/InGaAs (200 nm, stop etch layer)/InAlAs (40 nm)/InGaAs (50 nm, grade layer)/InGaAs (7400 nm, absorption layer)/InGaAs (50 nm, grade layer)/InAlAs (40 nm), with all layers nominally undoped. The MSM PD was fabricated using standard photolithography, followed by metal deposition, and a lift-off process to define the Schottky contacts. The Schottky contact was Pt/Ti/Pt/Au (50 Å/400 Å/400 Å/2200 Å). Circular mesas with a diameter of 280 μm were patterned over the devices, and served as masks during the mesa etching. The InGaAs was mesa etched down to the InP layer using citric acid:H_2O_2:H_2O (140:10:50). The MSM PDs were then coated with Apeizon W and placed in HCl:H_2O (2:1) to remove the InP substrate. The LED was a heterostructure PpPnN: GaAs (20 nm, contact layer)/AlGaAs (1000 nm, cladding layer)/GaAs (1000 nm, Active layer)/AlGaAs (1000 nm, cladding layer)/GaAs (20 nm, contact layer) with a 200 nm AlAs sacrificial etch layer grown between the device layers and the GaAs substrate. AuZn/Au (1000 Å/1500

Å) served as an ohmic p-contact and, after being patterned, as circular mesa masks with a diameter of 50 μm. The LED material was mesa etched down to the AlAs layer using H_2SO_4:H_2O_2:H_2O (1:8:200). The LEDs were coated with Apiezon W and placed in 10% HF, which selectively laterally etched the AlAs and released the devices from their growth substrates [21]. Both the I-MSMs and the LEDs embedded in Apiezon W were then bonded to transparent Mylar diaphragms (a separate diaphragm for each type of device), and the Apiezon W was then removed using trichloroethylene.

The I-MSM PD was bonded onto the Ti/Au pads on the nitride-coated silicon substrate first, and dc characteristics were measured to verify that the device operated properly. Then, the first benzocyclobutene (BCB) isolation layer was spun on and cured at 240 °C for 1 hour, with a resulting thickness of approximately 1.7 μm. A thin adhesion layer of SiO_2 was then deposited onto the BCB using plasma enhanced chemical vapor deposition (PECVD). After depositing and defining the LED bottom contact pad in the center of the thin film bonded I-MSM, the LED was integrated onto the pad. The metals used for the bottom contact were Ti/Au/Pt/Ti/Al/Ti/Pt/Au. The Al was used to protect the bottom contact during the removal of the BCB, and the Ti/Pt served as diffusion barriers between the gold and aluminum, which form intermetallics at temperatures at or above 240°C. Next, a second BCB isolation layer was spun on and cured, with a resulting total BCB thickness of approximately 3.4 μm. A thin SiO_2 adhesion layer was deposited using PECVD. A circular contact window with a diameter of 40 μm was etched open using an RIE with SF_6:O_2. The top contact of the LED was defined and deposited with a circular 30 μm diameter aperture using AuGe/Ag/Au/Ti/Al.

Finally, all of the remaining exposed BCB was removed using RIE with $SF_6:O_2$. A photomicrograph of the final co-located device structure is shown in Figure 41.

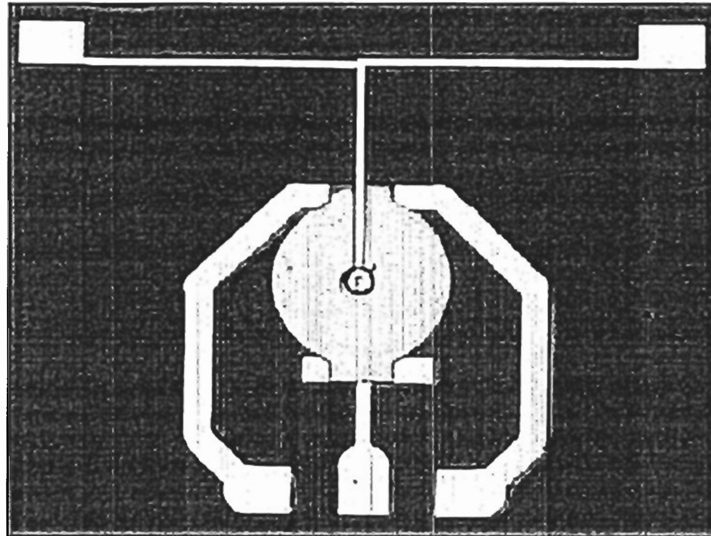

Figure 41: Top view of 3D GaAs/InGaAs stacked structure.

The dark current and photocurrent of the thin film I-MSM PD and the co-located I-MSM PD bonded to the nitride-coated silicon were measured. The dark current results are shown in Figure 42. The dark current of the I-MSM PD before LED integration

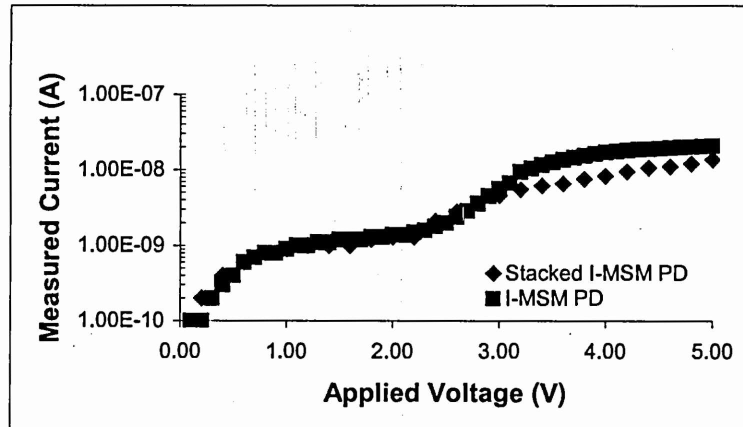

Figure 42: Dark current measurements before and after stacking.

was 21.0 nA at 5 V and the dark current for the co-located I-MSM (with the stacked LED) was 18.8 nA at 5 V. The use of a Pt diffusion barrier metal in the MSM contacts prevented 4 hours of BCB curing at 240°C from degrading the Schottky barrier, and hence, the dark current [88].

To measure the photocurrent, a Hewlett Packard 8153A lightwave multimeter was used as a cw lightsource with $\lambda = 1321$ nm. A mode scrambler was inserted into the light path to make the fiber output more uniform [22], [23], [24]. The light was incident on the device using a 3 m length of 62.5 μm core diameter multimode optical fiber with an NA of 0.22. The responsivity of the I-MSM PD without the LED was 0.36 A/W (measured before the LED was integrated). After integration of the LED onto the I-MSM, the measured photocurrent from the I-MSM PD as a function of longitudinal displacement is shown in Figure 43. The stacked PD responsivity is smaller since the LED shadows the PD, and thus, a fraction of the incident power is not collected by the PD.

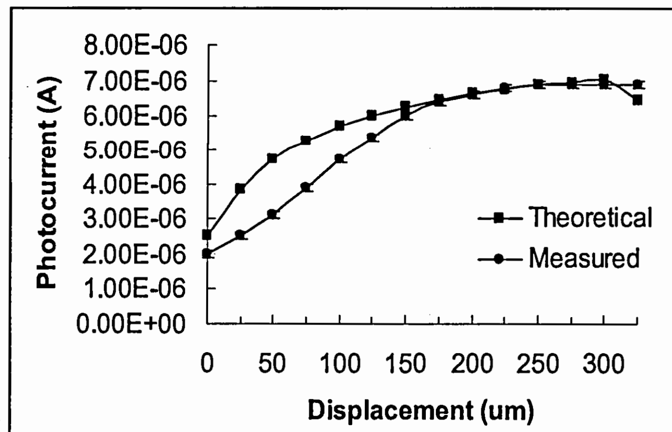

Figure 43: Photocurrent versus longitudinal displacement of fiber from the 3D LED/PD stack.

The LED L-I curve was measured using an ILX Lightwave LDP-3811 precision pulsed current source driving the LED. The output light was coupled into a multimode

step index optical fiber with a core diameter of 600 μm and a numerical aperture (NA) of 0.48. The other end of the fiber was FC connected to a silicon photodetector with a responsivity of 0.45 A/W at λ = 850 nm. The measured L-I curve of the LED is shown in Figure 44.

By changing the PD material from GaAs to InGaAs the detector was optimized for high speed operation. This change in PD material also broadened the spectral response. The responsivity at λ = 1300 nm was 0.31 A/W, which was the highest responsivity achieved out of the three stack designs. The LI curve showed that the RCE LED was functioning properly.

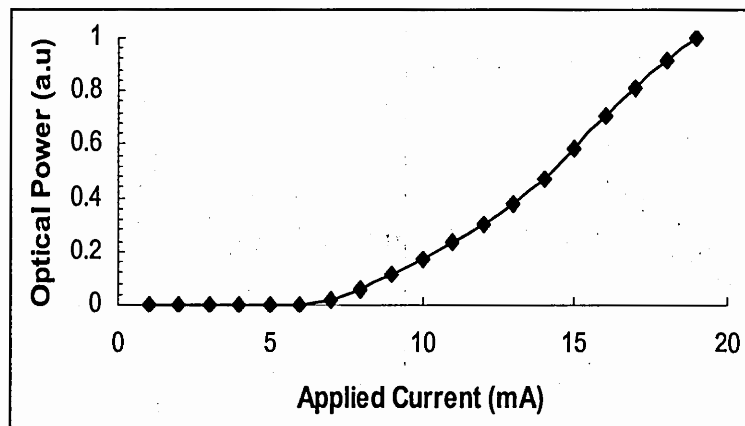

Figure 44: LI curve of mixed stacked LED.

3.4 3D Stacked Thin film I-MSM PD/RCE LED on CMOS Circuit

In the previous sections photodetectors and/ or light emitters were integrated onto oxide coated silicon. The SiN_x and SiO_2-coated silicon host substrates used for the stacked the thin film devices are very similar to silicon CMOS circuits. This section highlights the integration of those photonic devices from the previous section with CMOS circuitry to form optoelectronic integrated circuits (OEICs) using thin film integration.

To create an optoelectronic transceiver, the circuit must consist of a receiver and transmitter section. In addition, an overglass (SiO_2) with open windows over the detector and emitter contact pads is needed to isolate the photonics from the conductive silicon circuit. The circuit used in this research, which is shown in Figure 45, met all of these requirements. All of these circuits were designed by Professor Martin Brooke's research group at Georgia Tech.

The receiver for this circuit consisted of a current-to-voltage converting stage and nine differential voltage amplifier stages. A differential design style was chosen for better noise immunity and bias stabilization during high speed operation. In addition, this topology was selected because it provides a low input resistance, which is critical for high speed operation [89]. The structure of the receiver with its subcomponents is shown in Figure 46.

The transmitter also followed a differential topology. This topology provided current ripple stabilization in the power lines, which is necessary to avoid errors in the emitter output [90]. Furthermore, the differential design minimizes simultaneous

switching noise by subtracting the common noise [90]. The transmitter circuit for driving the emitters is shown in Figure 47.

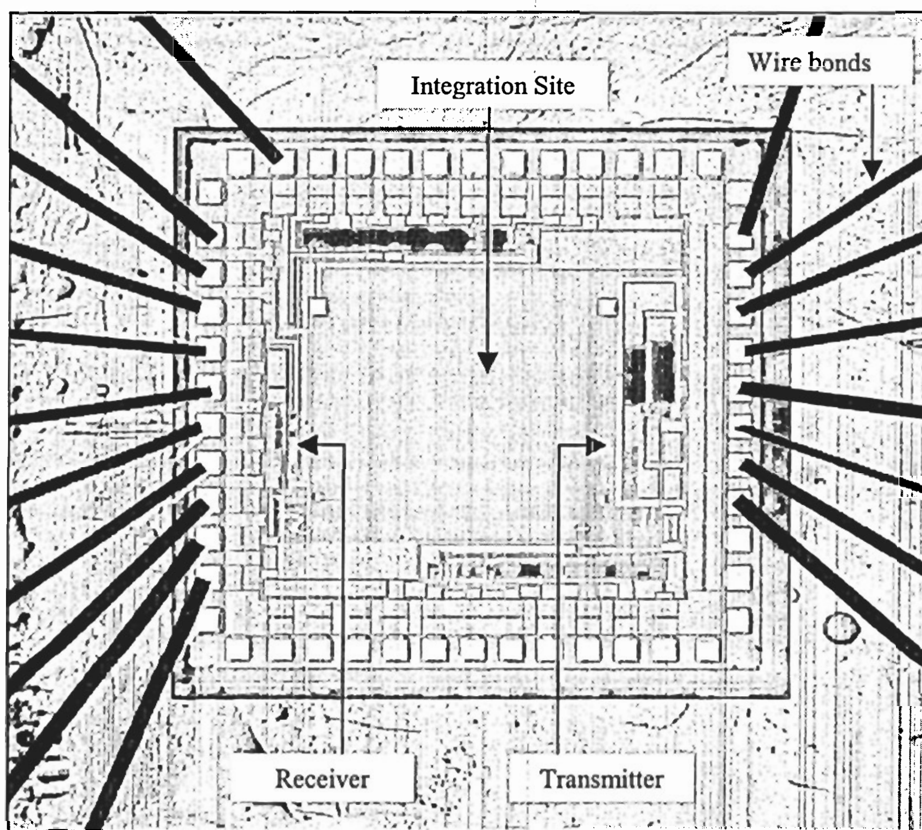

Figure 45: Silicon CMOS transceiver circuit.

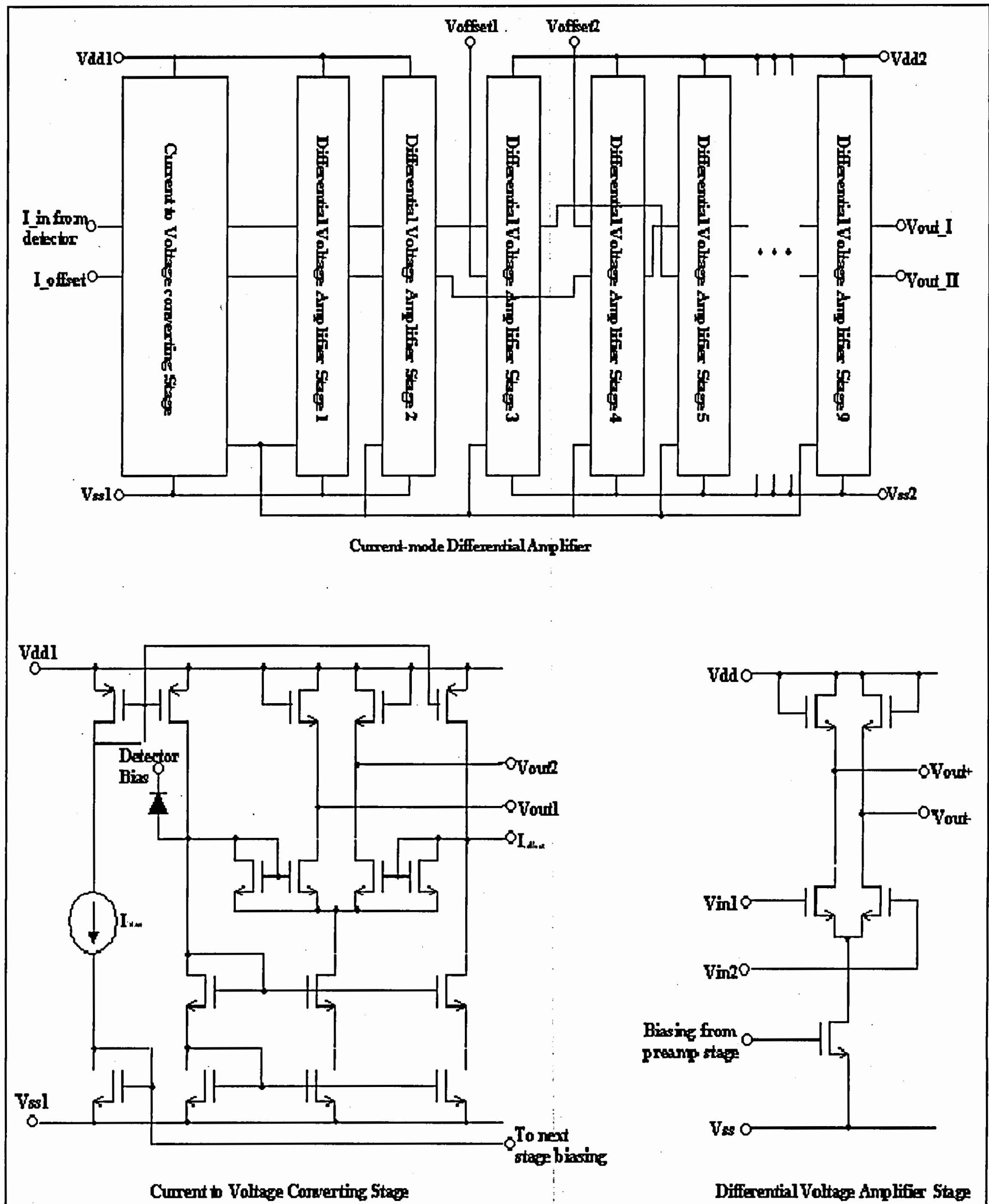

Figure 46: Structure of receiver and subcomponents [89].

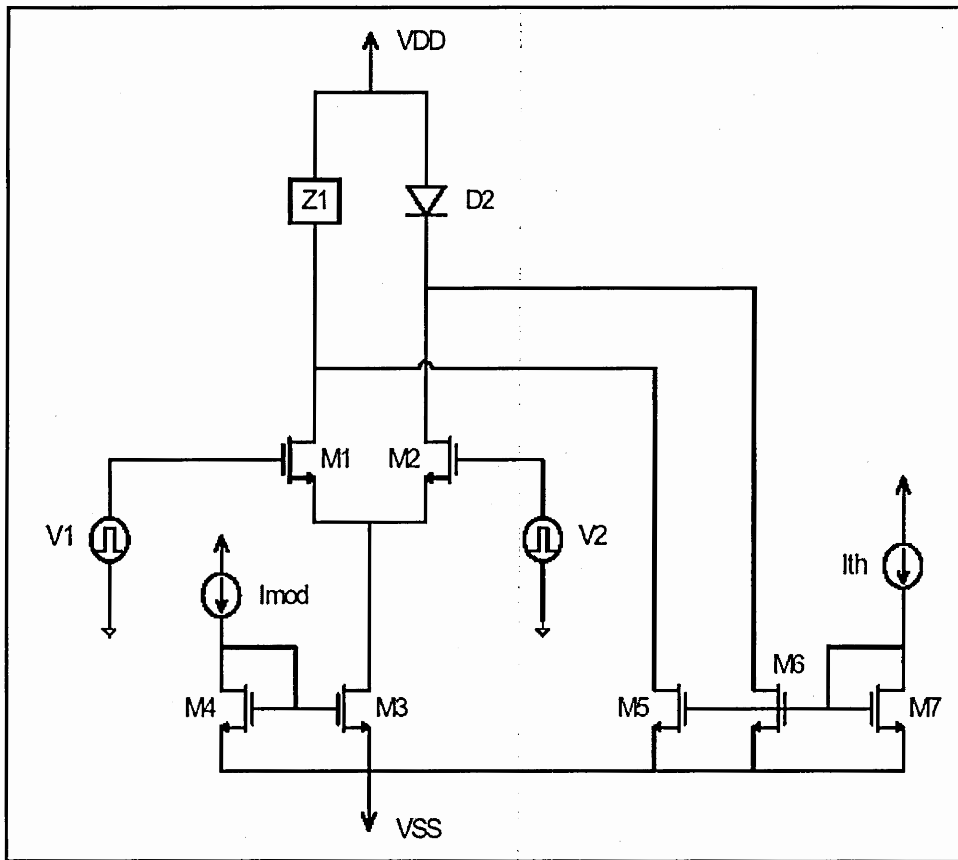

Figure 47: Differential emitter driver [90].

3.4.1 Integration Process for 3D Stacked Emitters/Detectors on CMOS Circuits

To integrate the 3D stacked thin film structure on a CMOS circuit, modifications to the 3D stack thin film process shown in Figure 32 were necessary due to additional p- and n- contact vias. The host substrate area for integration onto SiO_2-coated silicon was approximately 10 mm x 10 mm and the circuit area was 2 mm x 2 mm, which is 25 times smaller. The smaller area made it difficult to ignore the edgebead formed during the application of the BCB. The edgebead left the integration site for the LED nonuniform and left unetched BCB on some wirebonding pads. To reduce the edgebead, circuit scraps were placed around the edges of the circuit when BCB was spun on. Proper placement of the scraps left only a small amount of edge bead on three unused wirebond pads.

With the addition of two more vias, additional RIE steps were necessary to open the windows. This increased the possibility of redeposition (RIE grass) on the circuit. Therefore, photodefinable BCB (photo-BCB) was used instead of dry etch BCB.

The first step in the modified 3D stack thin-film process was to deposit the I-MSM PD Ti/Au contact pads, which was e-beam deposited Ti/Au (400Å/2200Å). Next the I-MSM PD was integrated. Then, the first photo-BCB isolation layer was spun on using scraps, was exposed, developed, and cured at 240 °C for 1 hour, with a resulting thickness of approximately 2.0 μm. To remove any unwanted residue from the p- and n- contact vias, the circuit was etched in the RIE using SF_6:O_2 for 45 seconds. This step also increased the BCB/metal adhesion. After depositing and defining the LED bottom contact pad in the center of the embedded I-MSM PD, the LED was integrated onto the

pad. The metals used for the bottom contact were Ti/Au/Pt/Ti/Al/Ti/Pt/Au. The Al was used to protect the bottom contact during the removal of the BCB, and the Ti/Pt served as diffusion barriers between the gold and aluminum. Next, a second photo-BCB isolation layer was spun on, exposed, developed, and cured, with a resulting thickness of approximately 3.4 μm. During the exposure and development step a circular via with a diameter of 40 μm over the LED was opened along with the re-opening of the n-contact via. Again, to remove any unwanted residue from the p- and n- contact vias, the circuit was etched in the RIE using SF_6:O_2 for 45 seconds. The top contact of the LED was defined and deposited with a circular 30 μm diameter aperture using AuGe/Ag/Au/Ti/Al. Finally, all of the remaining exposed BCB was removed using RIE with SF_6:O_2. The 3D stacked device process for silicon CMOS circuits is shown in Figure 48. Pictures of a GaAs RCE LED/InGaAs I-MSM PD 3D stack integrated on to silicon CMOS circuitry using the modified process are shown in Figure 49 and Figure 50.

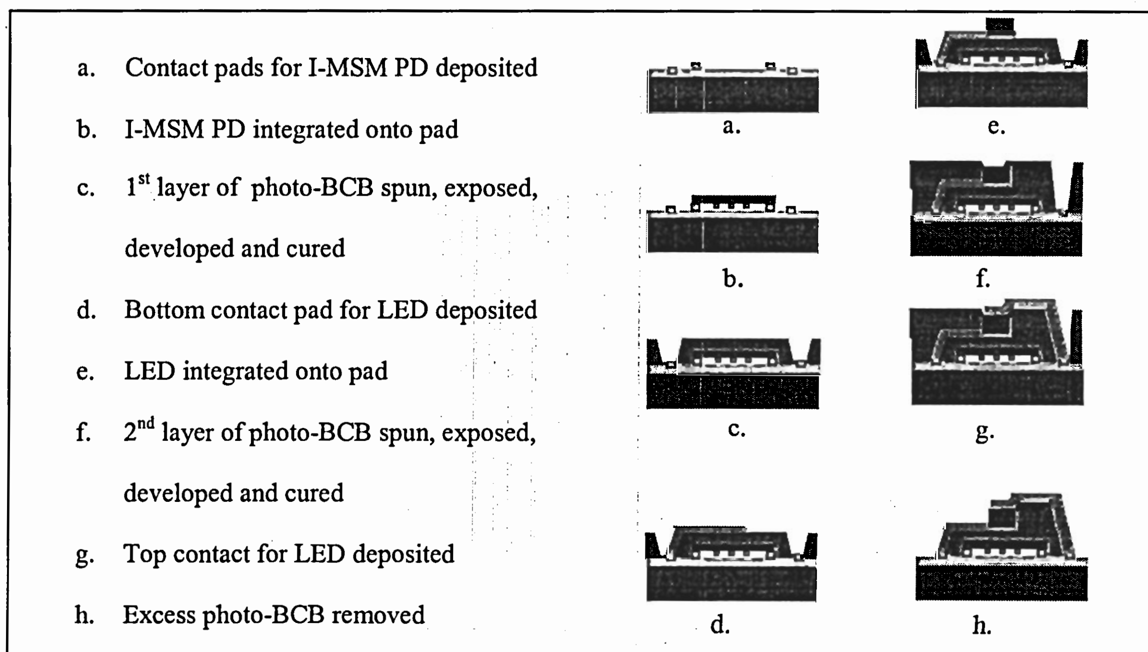

Figure 48: 3D stacked thin film process for silicon CMOS circuit integration.

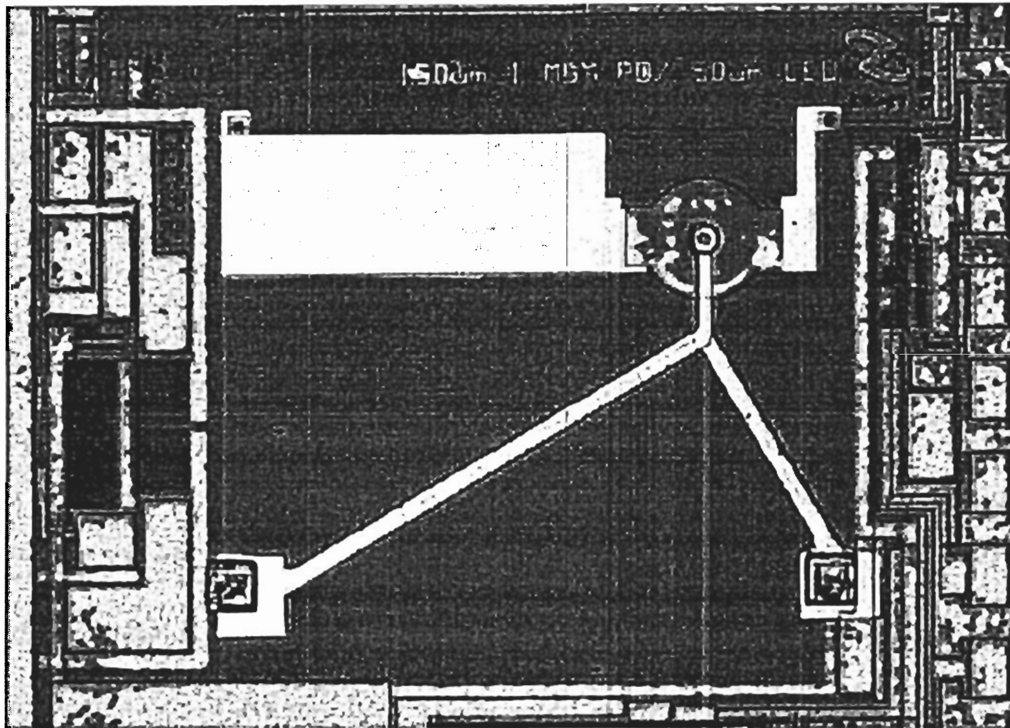

Figure 49: 3D Stacked GaAs RCE LED/InGaAs I-MSM PD on silicon CMOS circuitry.

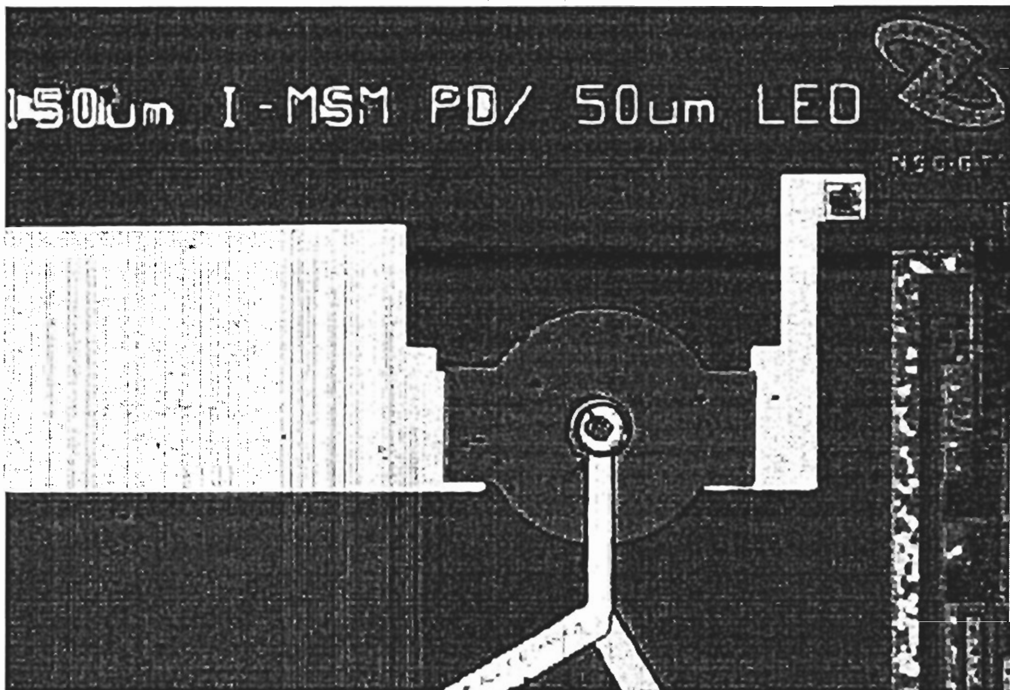

Figure 50: Closer view of RCE LED/PD in Figure 49.

3.4.2 Stacked Device Circuit Testboard

Once the on-circuit stacked devices pass the functionality tests, the circuits are bonded to a test board. The circuits are fabricated such that the designers have the ability to adjust several voltage and current biases to achieve the maximum transceiver performance. Studies have shown that a high percentage of circuits do not perform as expected from simulation results [91]. Therefore, the testboard is designed as shown in Figure 51, with all of the available pads for adjusting the biases. After bonding the circuit to the board, the circuit is wirebonded as shown in Figure 52.

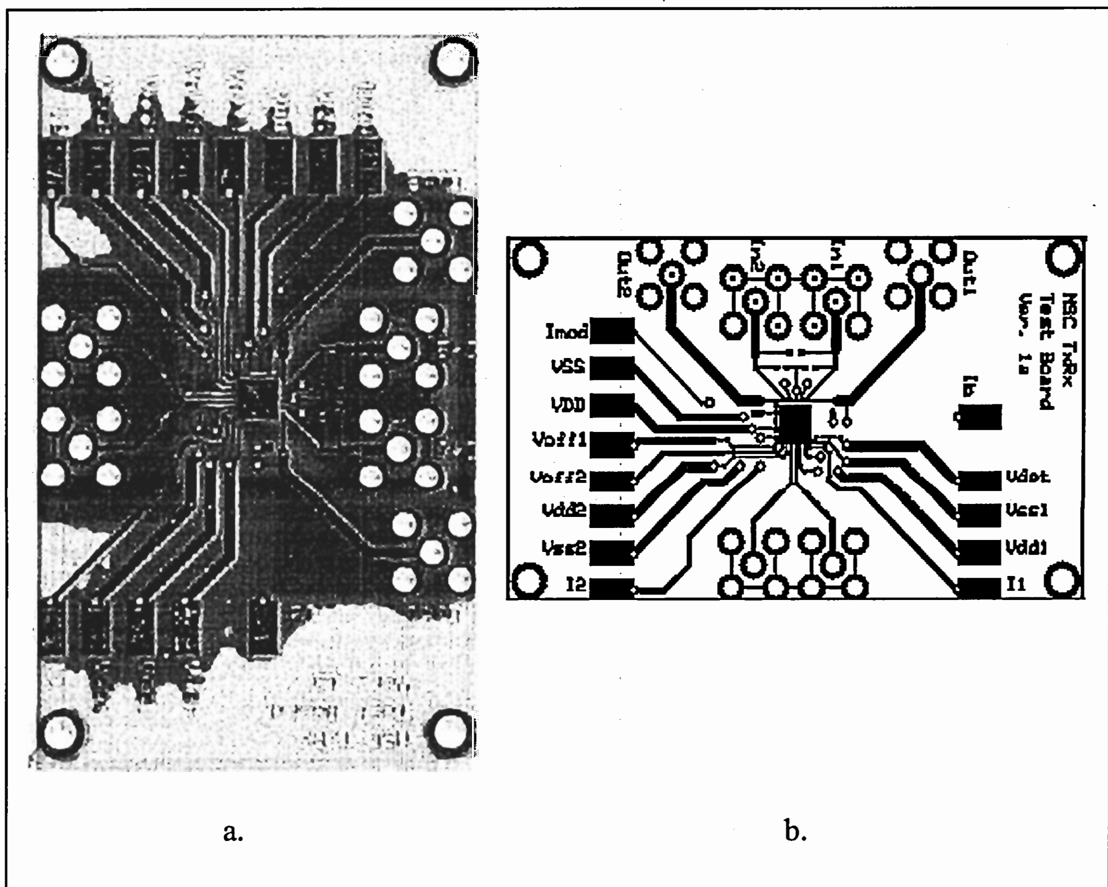

Figure 51: a) Picture of circuit testboard and b) schematic.

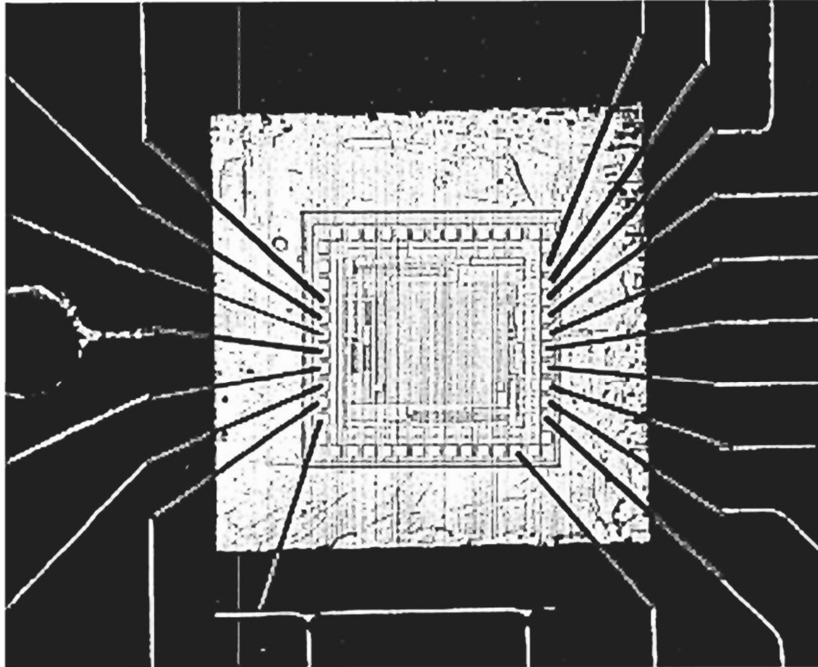

Figure 52: Circuit photo with wirebonding diagram.

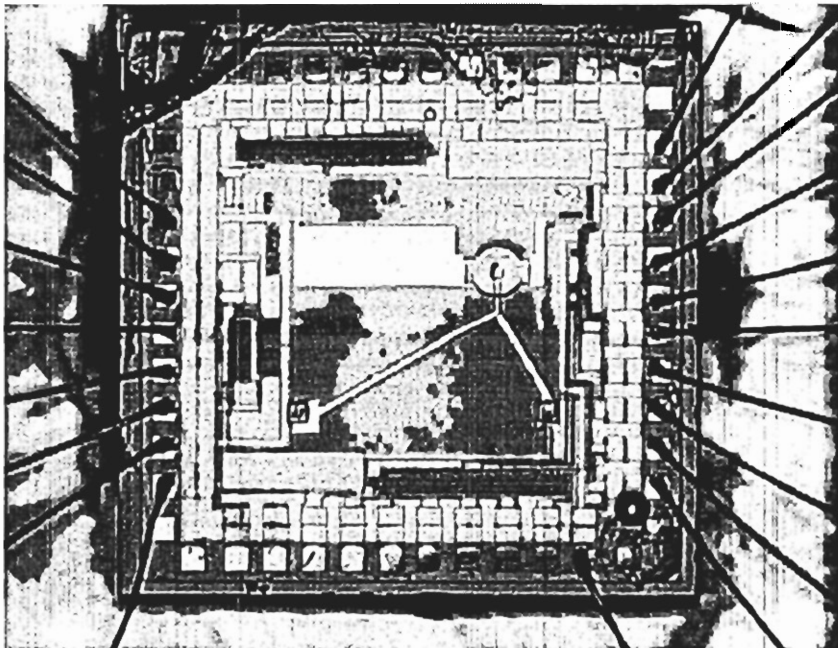

Figure 53: Integrated circuit photo with wirebonds.

3.4.3 3D Stacked Device Circuit Measurement Setup and Results

Once the circuit is bonded to the testboard and the wirebonding is completed, functionality tests are performed to verify that the stack devices are still working. As stated earlier, the circuit has both receiver and transmitter circuitry. To test the speed of the optical receiver, a laser with an external modulator is used, operating at $\lambda = 1550$ nm wavelength, to excite the photodetector. A Microwave Logic bit error rate tester (BERT) supplies the modulation and a Tektronix Communication Signal Analyzer (CSA) reads the output signal. The measurement setup for the receiver portion of the transceiver is shown in Figure 54. All OEIC testing was performed collaboratively with members of Professor Martin Brooke's research group at Georgia Tech.

The transmitter portion of the transceiver also requires the use of a BERT and CSA for speed testing of the LED. The BERT modulates the current providing modulation to the LED. The output signal is captured with a silicon photodetector with a responsivity of 0.5 A/W at $\lambda = 850$ nm that operates at 155 Mbps. The signal is then fed into a transimpedance amplifier (TIA) with an input sensitivity of approximately 0.26 μA and a differential gain of 22 K. A limiting amplifier follows the TIA with an input sensitivity of 2 mV. Finally the output signal is read by the CSA. The optical transmitter measurement setup is shown in Figure 55.

The speed results of the integrated optical receiver are shown in Figure 56 and Figure 57. Both the output signal and eye diagram show the photodetector operating at 1 Gbps. The speed results of the optical transmitter are shown in Figure 58 and Figure 59. In these two figures, the LED is operating at 40 Mbps. The spectral output of the LED, which was measured using a spectrum analyzer, is shown in Figure 60.

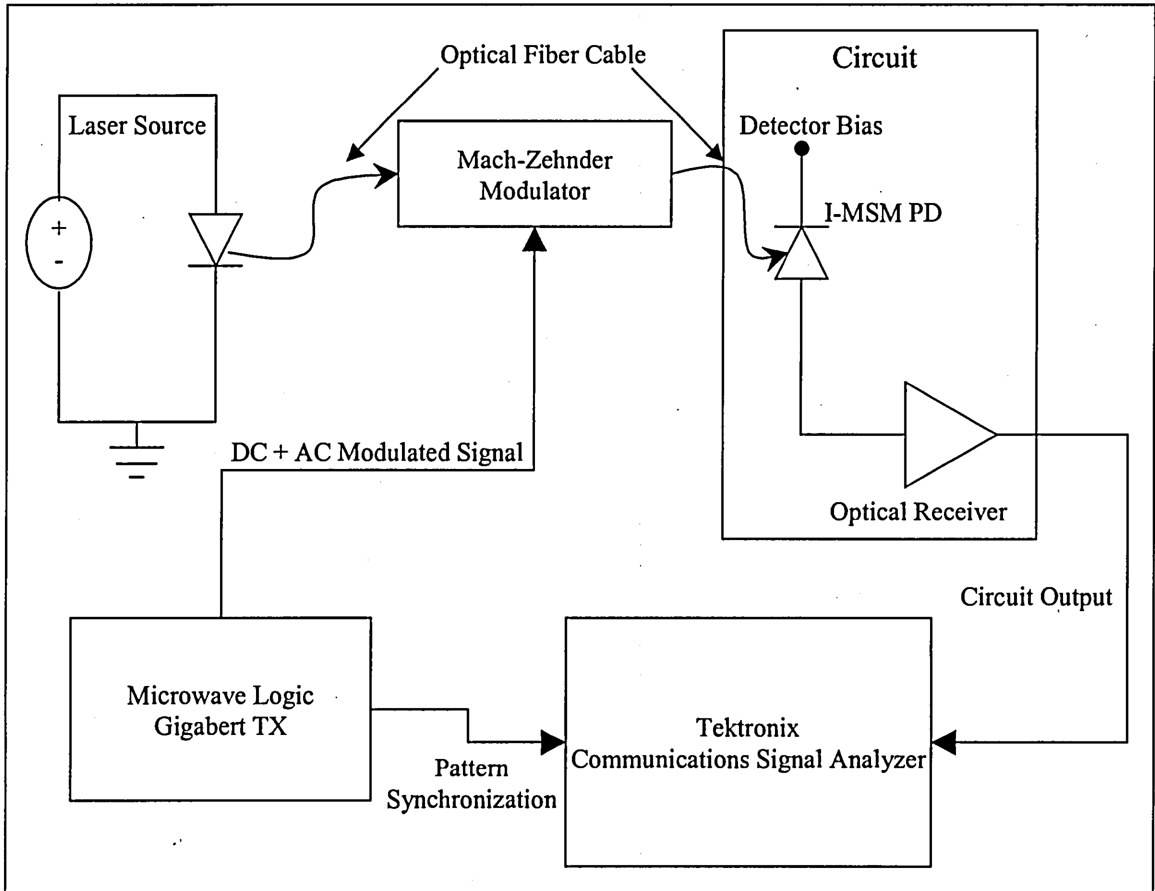

Figure 54: I-MSM photoreceiver speed measurement experimental setup.

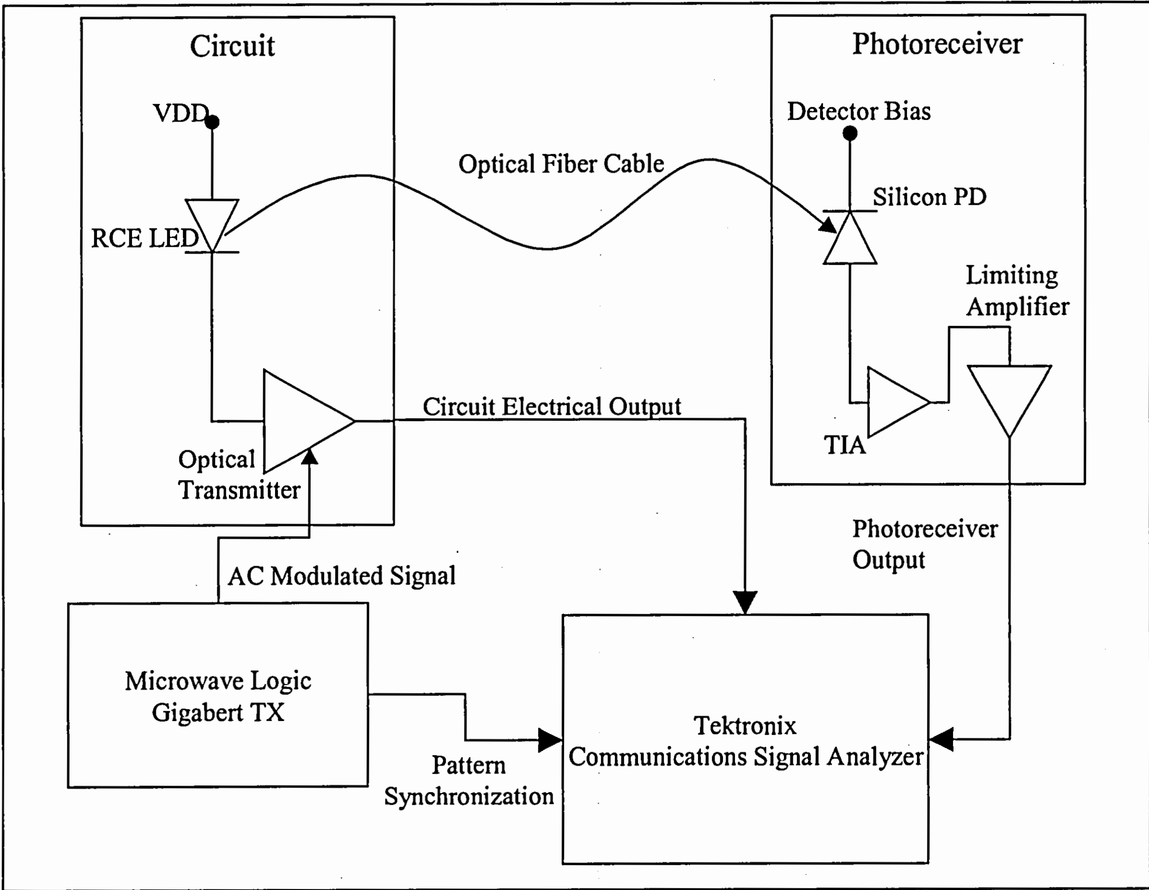

Figure 55: RCE LED optical transmitter speed measurement experimental setup.

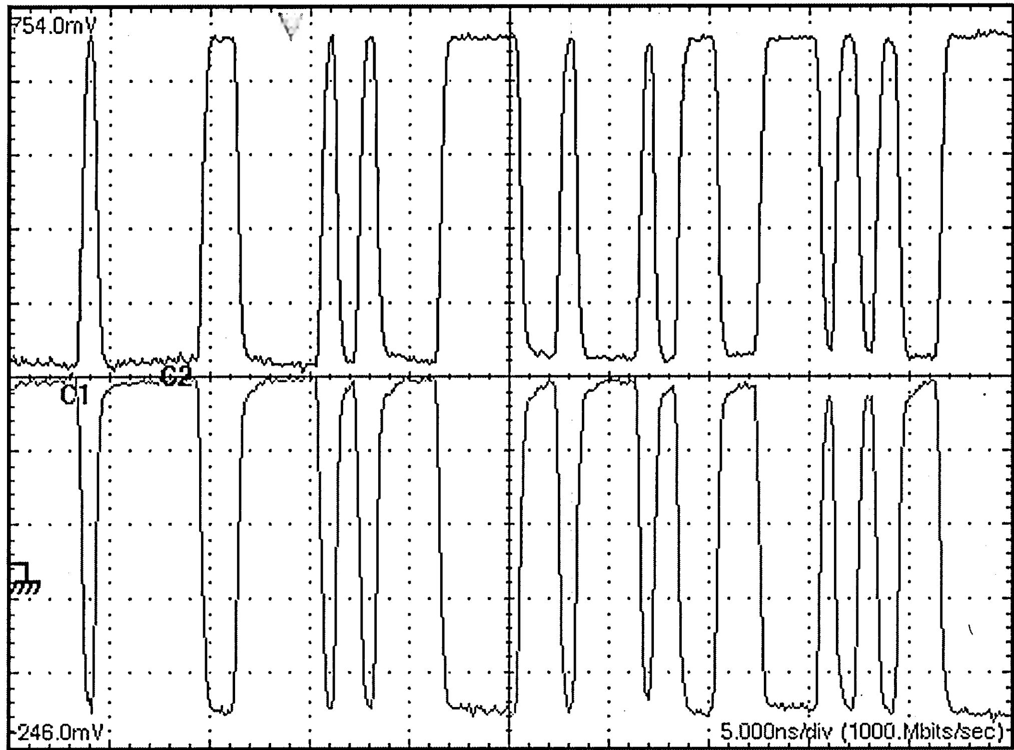

Figure 56: I-MSM photoreceiver output signal at 1Gbps.

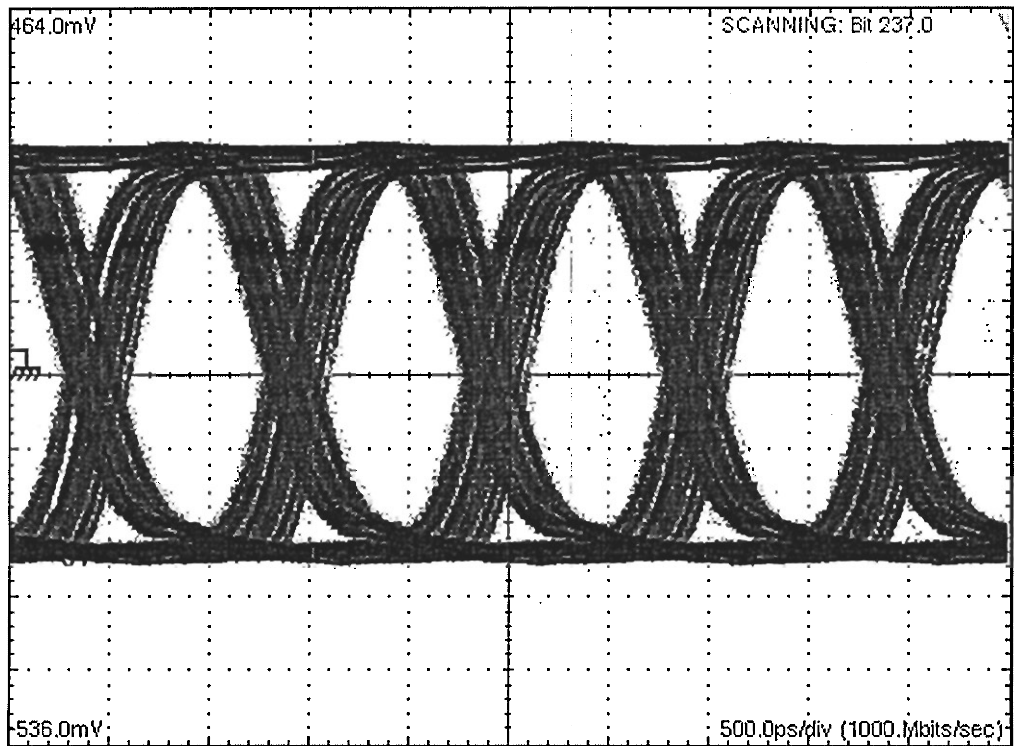

Figure 57: I-MSM photoreceiver eye diagram at 1Gbps.

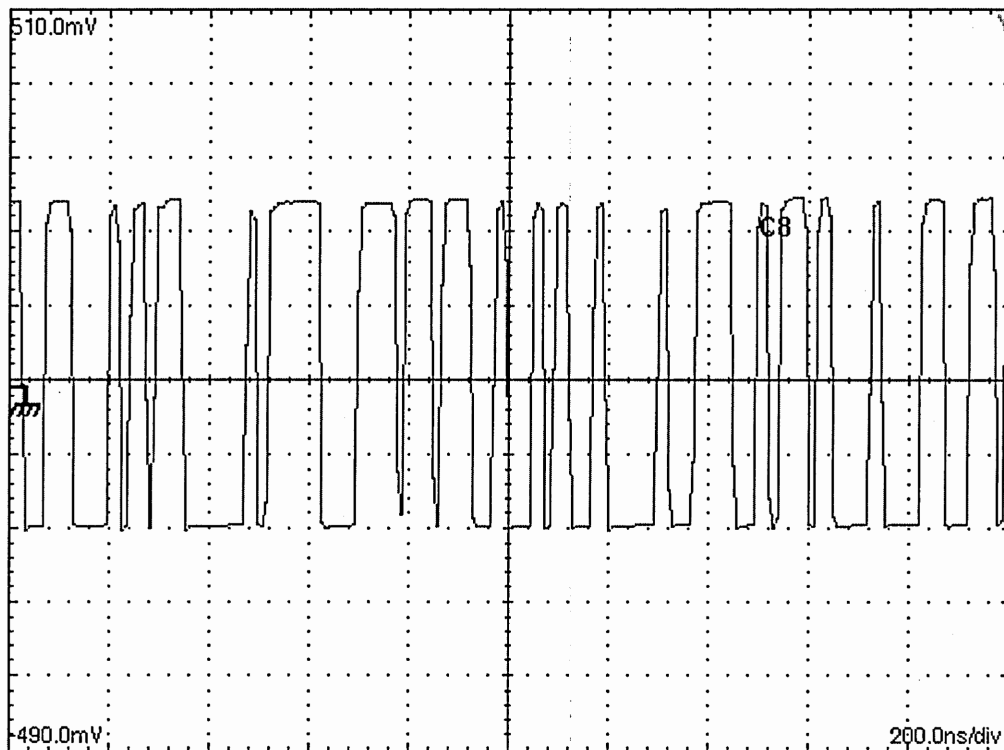

Figure 58: RCE LED optical transmitter signal at 40 Mbps.

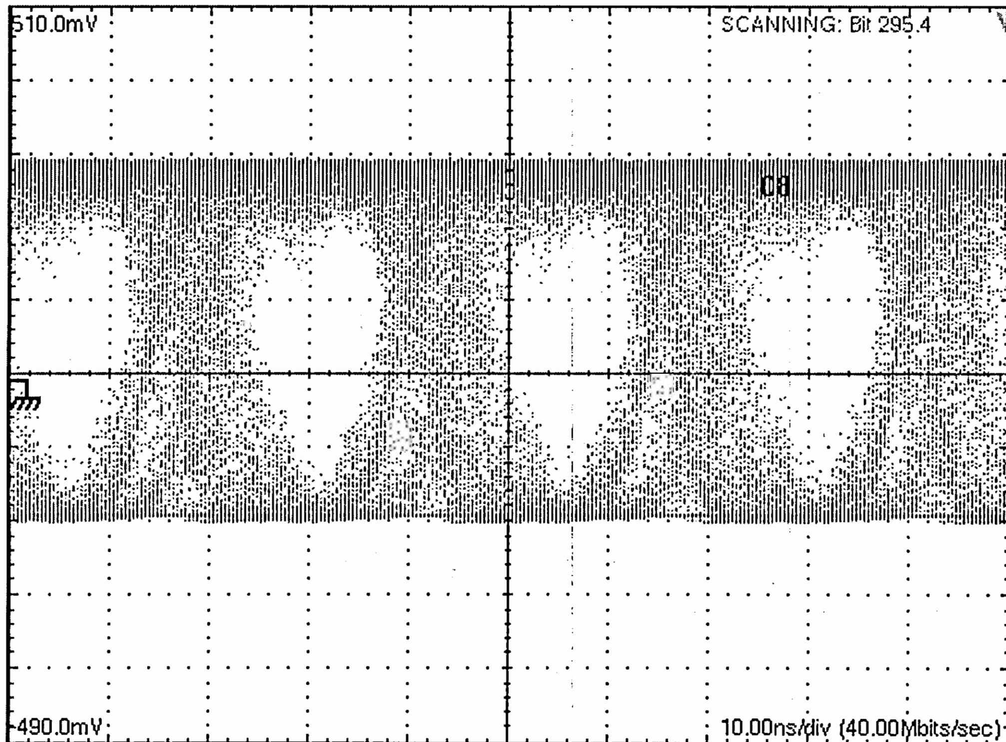

Figure 59: RCE LED optical transmitter eye-diagram at 40 Mbps.

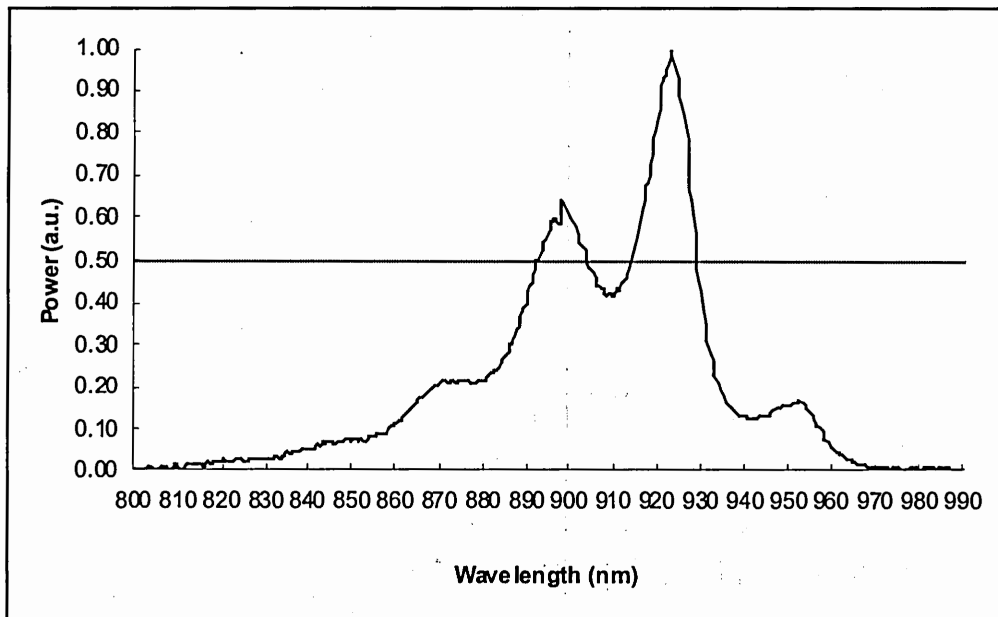

Figure 60: RCE LED spectral output.

To integrate the 3D stacked thin film devices onto silicon CMOS circuits, modifications to the 3D stacked device process was necessary. For example, photodefinable BCB was used instead of dry etch BCB to reduce the amount of RIE redeposition. The OEICs were wirebonded to testboards and tested. The integrated optical receiver operated at 1 Gbps. Theoretically, an I-MSM PD with a 150 μm detection diameter can operate at 9 GHz. However, the receiver circuit that was used for this research was designed to operate at 1 Gbps. The integrated optical transmitter operated at 40 Mbps. This speed was slower than what was expected. LEDs have been shown to operate at speeds greater than 100 Mbps. The integrated LED speed was limited by the size and length of the electrical interconnects between the LED and the circuit pads. The speed was also limited by the current injection.

CHAPTER 4

THEORETICAL CALCULATIONS OF ALIGNMENT TOLERANCE USING GEOMETRICAL OPTICS

To model and analyze the coupling between a 3D stacked device and a multimode optical fiber, a geometrical optics approach was selected. This approach is appropriate for evaluating the coupling between an LED and a multimode fiber since the chosen emitter and fiber dimensions are much greater than the wavelength of the radiation [92]. The choice of multimode fiber over single mode fiber is suitable for low cost optical communication systems that involve LEDs. However, the output power distribution of multimode fibers is very difficult to model because of the large number of modes that are excited [43], [44], [45]. Over long lengths of fiber, steady-state modal equilibrium is generally established. In order to use geometrical optics to analyze the coupling between the fiber and I-MSM PD, the output power distribution is assumed to be uniform. As will be seen in the analysis, this assumption can be too pessimistic when a portion of the power is incident onto the LED, but it enables an estimate of the relative effects of longitudinal and lateral displacement [22].

There are a number of factors that govern the coupling between an LED and a fiber, and the coupling between a fiber and center-shadowed photodetector. The analysis that follows uses a reasonable approach that gives estimations that are useful in understanding the effects of alignment tolerance on coupling between a fiber and 3D stacked device.

4.1 LED Longitudinal Alignment Tolerance

As stated in chapter 2, the power distribution of a surface emitting LED is Lambertian. With this type of radiation, only a small fraction of the radiation emitted by the LED can be coupled into the fiber [92]. The power delivered from an LED at an angle θ measured relative to a normal to the emitting surface varies with *cos* (θ), where the brightness function is given as [22]

$$B(\theta,\phi) = B_o \cos\theta \qquad \textbf{Equation 70}$$

The total optical power emitted from a surface emitting LED of area, A_{LED}, and aperture radius, r_{LED}, is given by [22],

$$P_{LED} = A_{LED} \int_0^{2\pi} \int_0^{\pi/2} B(\theta,\phi) \sin\theta \, d\theta \, d\phi \qquad \textbf{Equation 71}$$

When the radius of the fiber core is larger than the radius of the LED, the power coupled into a step-index fiber is given by [22],

$$P_{Step} = \int_0^{r_{LED}} \int_0^{2\pi} \left(2\pi B_o \int_0^{\theta_{o,max}} \cos\theta \sin\theta \, d\theta \right) d\phi \; r dr \qquad \textbf{Equation 72}$$

The maximum coupling efficiency between an LED and a step index fiber with a core diameter that is larger than the LED diameter is given by [22],

$$\eta_{Step} = \frac{P_{Step}}{P_{LED}} = (NA)^2 \qquad \textbf{Equation 73}$$

When the LED diameter is larger than the fiber core diameter the coupling efficiency is given by [22],

$$\eta_{Step} = \left(\frac{r_{core}}{r_{LED}} \right)^2 (NA)^2 \qquad \textbf{Equation 74}$$

As the fiber is displaced longitudinally away from the 3D stack, the effective radius of the LED increases and is given by,

$$r_{beam} = r_{LED} + Z \times \tan\theta_{max} \qquad \textbf{Equation 75}$$

where Z is the longitudinal displacement as shown in Figure 61 and the optical output angle, θ_{max}, is the fiber acceptance angle,

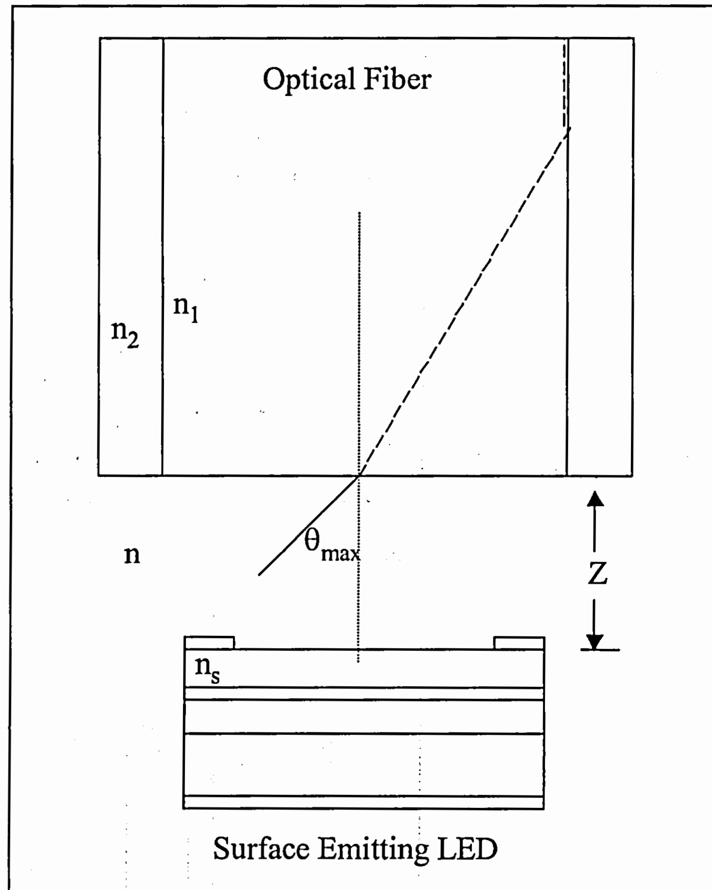

Figure 61: Schematic of RCE LED and fiber

with $(NA)^2$ as the maximum coupling efficiency, the normalized coupling efficiency is given by,

$$\eta = \left(\frac{r_{core}}{r_{LED} + Z \times \tan\theta_{max}} \right)^2 \qquad \textbf{Equation 76}$$

A plot of the efficiency versus longitudinal displacement is shown in Figure 62. In this plot, the fiber core radius is 31.25 μm, which is the standard core size for multimode fiber. The aperture radius of the LED is 15 μm.

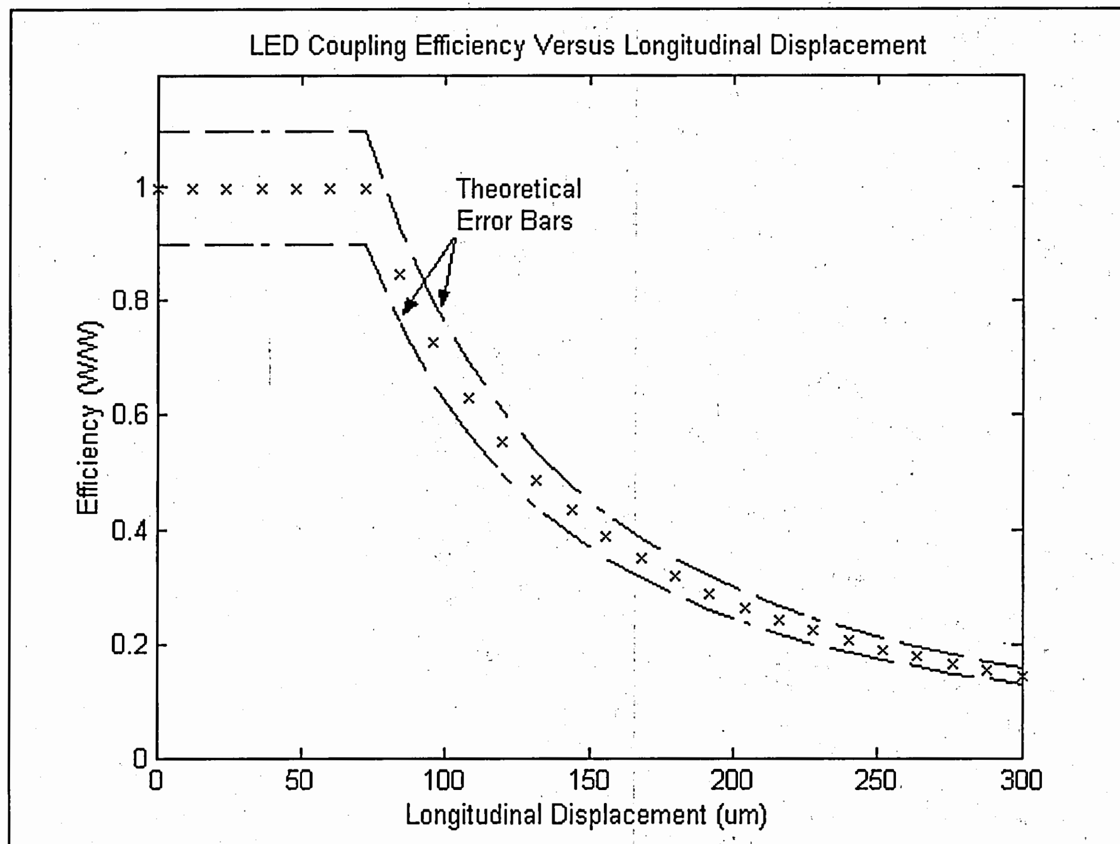

Figure 62: Normalized efficiency versus longitudinal displacement.

In conclusion, a theoretical model has been developed to calculate the coupling efficiency between an LED and a step index multimode fiber as a function of longitudinal displacement. This model assumes that the LED beam profile is Lambertian and uses a geometrical optics approach.

4.2 Stacked I-MSM PD Longitudinal Alignment Tolerance

In the case of the LED, the numerical aperture, which is related to the acceptance angle, limited the amount of light coupled into the fiber. In turn, as the optical signal exits the fiber, the output angle is equal to the critical acceptance angle,[22] as shown in Figure 63. As stated in the introduction of this chapter the output power of the multimode fiber is assumed to be uniform. Therefore, as the longitudinal displacement increases, so will the effective incident beam radius. The incident radius is given by,

$$r_{inc} = r_{core} + Z \times \tan\theta_{max} \qquad \textbf{Equation 77}$$

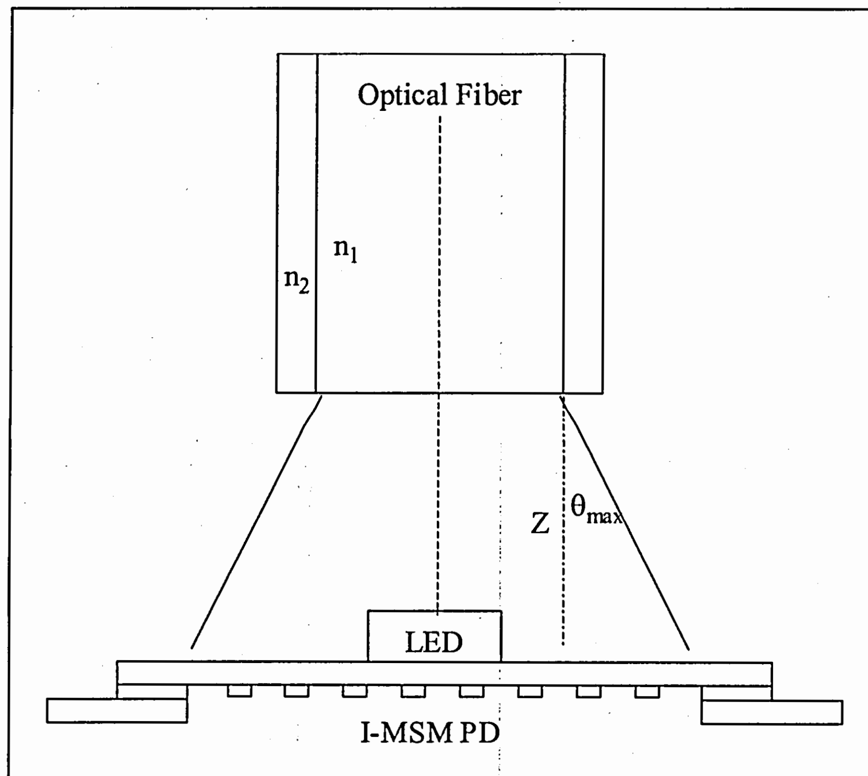

Figure 63: Schematic of LED shadowed I-MSM PD and fiber

To calculate the photocurrent generated from the incident beam, the following information must be know:

1. The total power of the beam
2. The area of the LED
3. The responsivity of the I-MSM PD.

There are two regions to consider when calculating the photocurrent:

1. The under-filled region (when the optical input signal does not fill the PD);
2. The over-filled region (when the optical input signal overfills the PD).

In the under-filled region, reduction in photocurrent is due to the LED shadowing. In this region the photocurrent is given by

$$I_p = P \times R \times \left(\frac{A_{Inc} - A_{LED}}{A_{Inc}} \right) \qquad \textbf{Equation 78}$$

where P is the incident power, R is the responsivity of the detector, and A_{inc} and A_{LED} are the areas of the incident beam and LED, respectively.

In the over-filled region, reductions in the photocurrent are not only due to LED shadowing, but also due to the power that falls outside the perimeter of the detector. In the over-filled region the photocurrent is given by

$$I_p = P \times R \times \left(\frac{A_{MSM} - A_{LED}}{A_{Inc}} \right) \qquad \textbf{Equation 79}$$

where A_{MSM} is the area of the photodetector. A theoretical plot of the I-MSM PD photocurrent versus longitudinal displacement is shown in Figure 65. The power was set to 27 μW. The responsivity was set to 0.36 A/W, which is consistent with measured

data. The radius of the LED was set to 25 μm, which is the LED mesa radius as shown in Figure 64, the radius of the fiber core was set 31.25 μm, and the radius of I-MSM PD was set to 100 μm, all values which are consistent with experimental values.

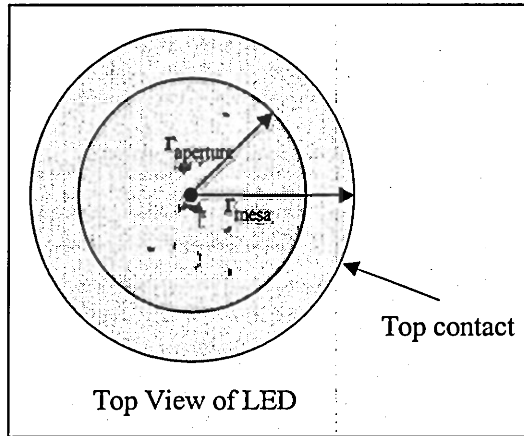

Figure 64: Top View of LED

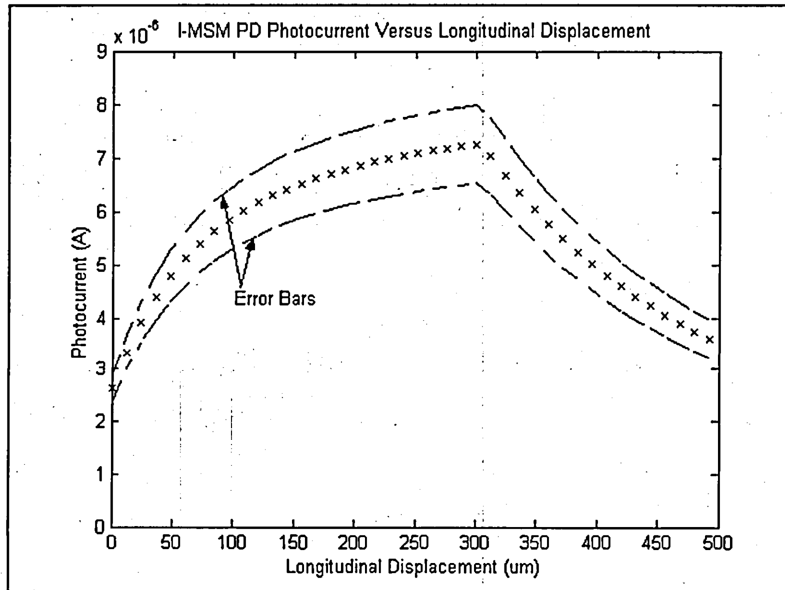

Figure 65: I-MSM PD photocurrent versus longitudinal displacement.

In conclusion, a theoretical model for calculating the integrated I-MSM PD photocurrent as a function of longitudinal displacement has been developed. The model assumes that the power distribution of the light exiting the fiber is uniform.

4.3 LED Lateral Alignment Tolerance

The coupling integral from section 4.1 is helpful in understanding the approach taken for calculating the coupling efficiency as a function of lateral displacement, which can be expressed as:

$$P_{Step} = \int_0^{r_{LED}} \int_0^{2\pi} \left(2\pi B_o \int_0^{\theta_{o,max}} \cos\theta \sin\theta \, d\theta \right) d\phi \; r dr \qquad \textbf{Equation 80}$$

Within the parenthesis are the integration terms for the acceptance cone. The outside integral sums up the contribution of each individual emitting point source of incremental area emitting from the LED. With lateral displacement, the overlapping area formed by the intersection of the circular LED output aperture and the optical fiber apparent aperture, as shown in Figure 66, defines the amount of optical power coupled from the LED into the fiber.

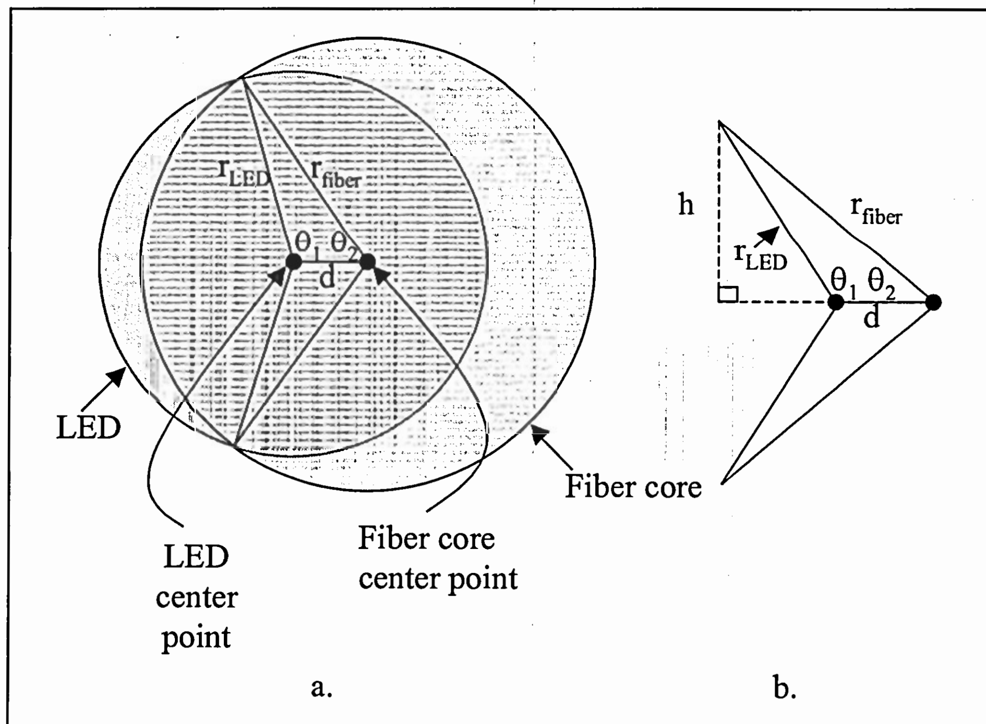

Figure 66: Lateral displacement between LED and fiber.

Once the overlapping area is established the coupling efficiency as a function of lateral displacement can be calculated as in the longitudinal case. When the fiber core covers the entire LED, the efficiency is equal to the square of the numerical aperture for the butt-coupled approximation. But, as the displacement, *d,* continue to increase such that the circles do not fully overlap, but only intersect, the efficiency becomes

$$\eta = \left(\frac{A_{over}}{A_{LED}}\right)(NA)^2 \qquad \textbf{Equation 81}$$

where A_{over} is the overlapping area. A helpful formula for calculating the overlapping area is the area of a sector [94],

$$A_{\sec tor} = \frac{1}{2} r^2 \theta \qquad \textbf{Equation 82}$$

where r is the radius of the sector with central angle, θ in radians as shown in Figure 67.

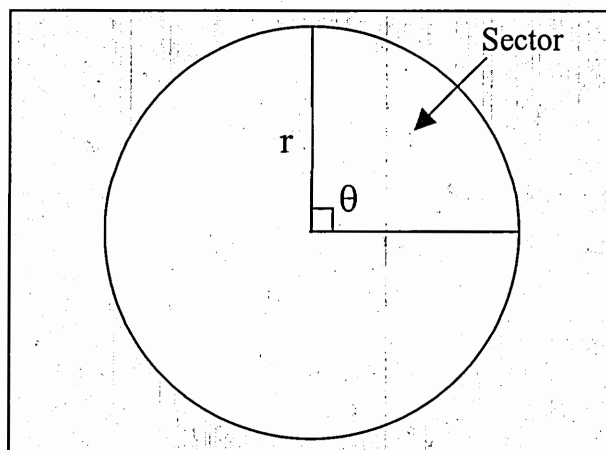

Figure 67: Diagram used to illustrate the area of a sector.

When $\theta = \pi/2$, the area of the sector is one-fourth the area of the circle. To illustrate this point, $\theta = \pi/2$ is substituted into Equation 83, and the resulting area of the sector is

$$A_{sector} = \frac{1}{2} r^2 \frac{\pi}{2} = \frac{\pi r^2}{4}$$ **Equation 83**

As seen in Figure 66, the radius of the LED forms a sector with central angle θ_1, as does the radius of the fiber with central angle θ_2. To find the overlapping area, the area of the two sectors must be added together. However, to avoid adding the triangle areas in the center twice, these areas have to be subtracted from the sum of the two sectors. The area of a triangle is given by [94]

$$A_{triangle} = \frac{1}{2} bh$$ **Equation 84**

where b is the base of the triangle and h is the height of the triangle. From Figure 66, the base of the triangles is d, the distance between the center of the LED and the center of the fiber core. The height of the triangles can be derived using the Pythagorean Theorem, which states that [95]

$$r^2 = h^2 + d^2$$ **Equation 85**

where r is the hypotenuse, h is the height and d the base of a right triangle. In Figure 68, there are two right triangles, where h is the height of both triangles, x and $x + d$ are the

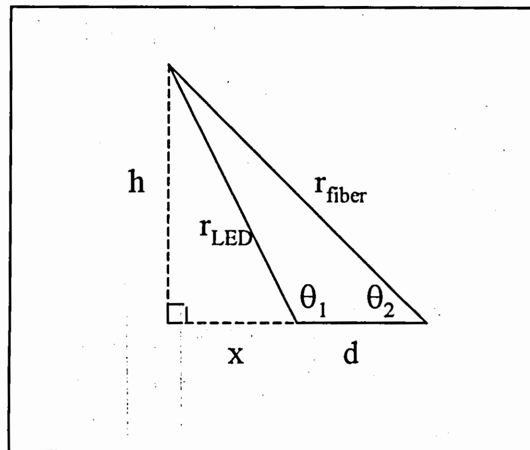

Figure 68: Triangle from Figure 66

bases, and r_{LED} and r_{fiber} are the hypotenuses of the smaller and larger triangles, respectively. From the larger triangle, r^2_{fiber} is given by,

$$r_{fiber}^2 = h^2 + (x+d)^2 = h^2 + x^2 + 2xd + d^2 \quad \textbf{Equation 86}$$

and from the smaller triangle, r^2_{LED} is given by,

$$r_{LED}^2 = h^2 + x^2 \quad \textbf{Equation 87}$$

After solving Equation 88 for x, x is substituted into Equation 87 and r^2_{fiber} is given by

$$r_{fiber}^2 = r_{LED}^2 + 2d\sqrt{r_{LED}^2 - h^2} + d^2 \quad \textbf{Equation 88}$$

The height of the two triangles is found by solving for h in Equation 89 and is given as

$$h = \left(r_{LED}^2 - \frac{\left(r_{fiber}^2 - r_{LED}^2 - d^2\right)^2}{4d^2} \right)^{1/2} \quad \textbf{Equation 89}$$

Therefore, the area of the two triangles is given by

$$A_{tri} = d\left(r_{LED}^2 - \frac{\left(r_{fiber}^2 - r_{LED}^2 - d^2\right)^2}{4d^2} \right)^{1/2} \quad \textbf{Equation 90}$$

Using the law of cosines, the two angles are [96],

$$\theta_1 = \cos^{-1}\left(\frac{r_{LED}^2 - r_{fiber}^2 + d^2}{2dr_{LED}} \right) \quad \textbf{Equation 91}$$

and

$$\theta_2 = \cos^{-1}\left(\frac{r_{fiber}^2 - r_{LED}^2 + d^2}{2dr_{fiber}} \right) \quad \textbf{Equation 92}$$

The total overlapping area is given by,

$$A_{over} = r_{LED}^2\theta_2 + r_{fiber}^2\theta_1 - dh \quad \textbf{Equation 93}$$

The lateral normalized coupling with lateral displacement is shown in Figure 69.

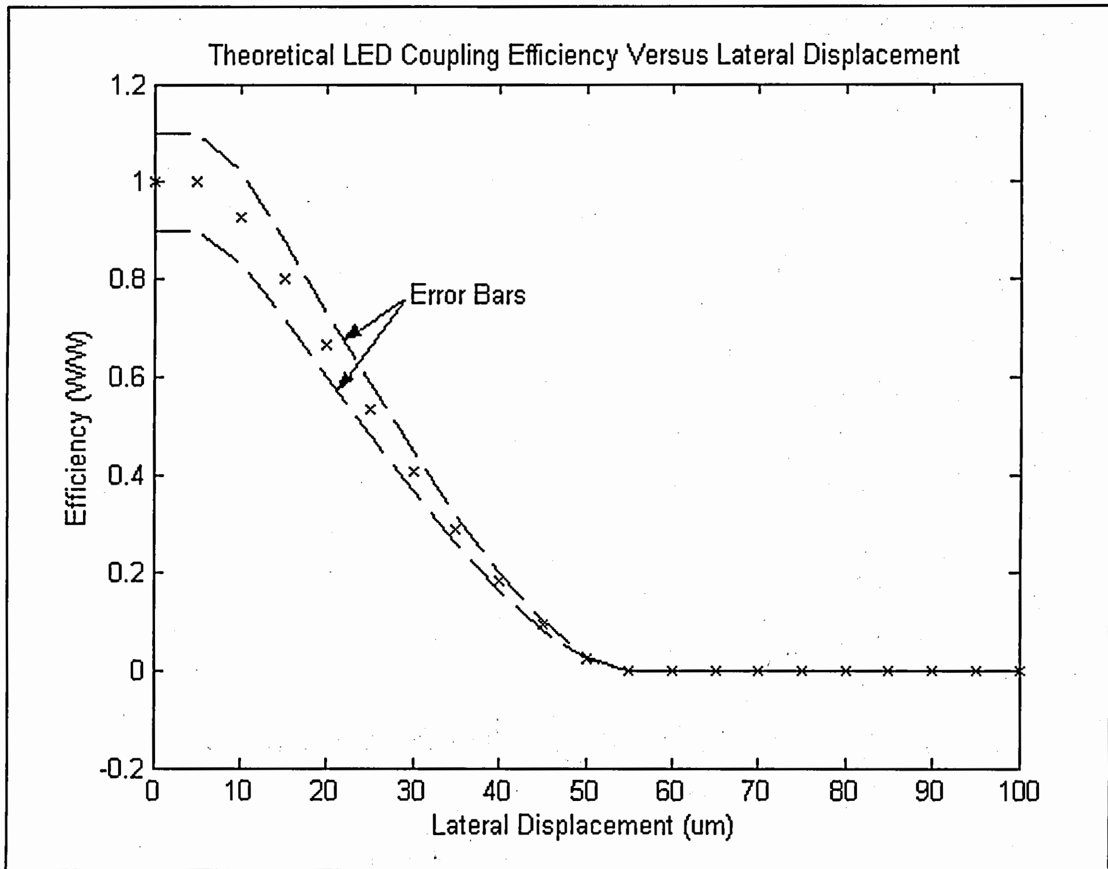

Figure 69: LED normalized coupling efficiency versus lateral displacement

In conclusion, a theoretical model has been developed to calculate the coupling efficiency between an LED and a step index multimode fiber as a function of lateral displacement. A geometrical optics approach has been taken to develop this model.

4.4 Stacked I-MSM PD Lateral Alignment Tolerance

As in the previous section, the overlapping area has to be calculated in order to derive the photocurrent as a function lateral displacement. In this section, however, the overlapping area of the LED and fiber is needed as well as the overlapping area of the fiber and detector. This point is illustrated in Figure 70.

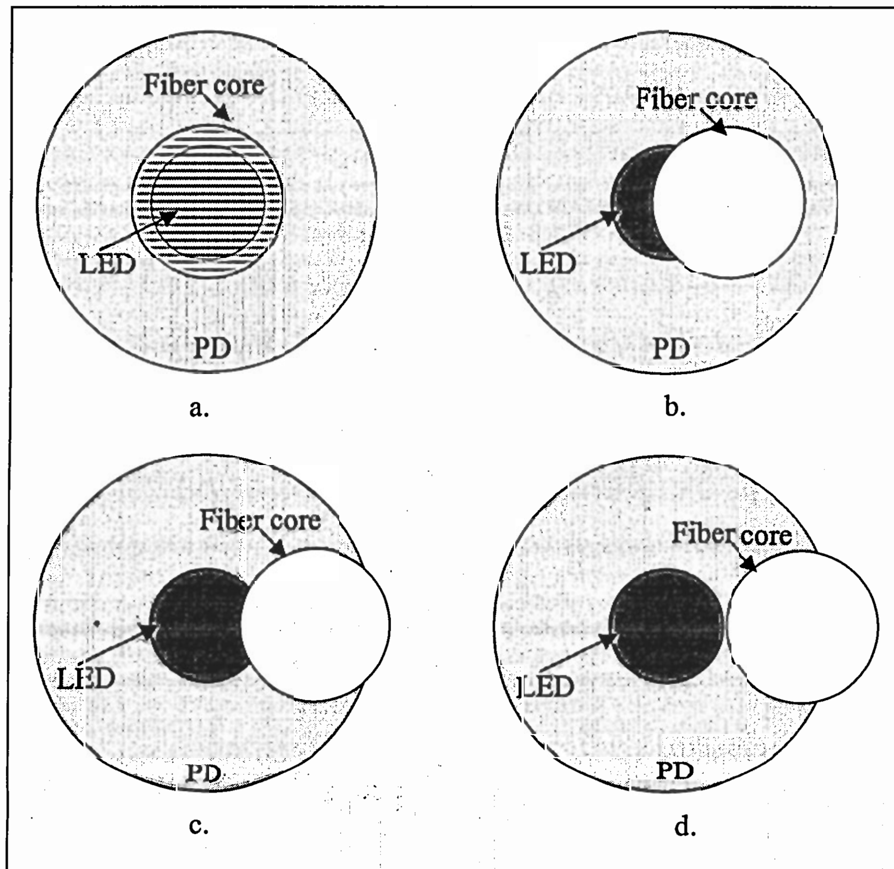

Figure 70: I-MSM PD lateral alignment tolerance in a) region 1, b) region 2, c) region 3, d) region 4.

There are four main regions to consider in identifying the area of detection:

1. The LED is within the fiber core area of illumination;
2. The LED and the fiber core illumination intersect;
3. The fiber core illumination intersect the LED and detector;

4. The fiber core illumination and the detector intersect, but the fiber core illumination does not intersect the LED area.

Within region 1 the LED shadows a portion of the detection area. In region 2, the photocurrent starts to increase because the LED is blocking less light. In region 3, the light beam is incident onto the emitter area, but is overfilling the detector, and as overfilling occurs, the photocurrent begins to decrease. In region 4, the LED no longer blocks a portion of the incident light, but the overfilling of the detector continues, as does the decrease in photocurrent. The photocurrent in region 1 can be expressed as

$$I_p = P \times R \times \left(\frac{A_{inc} - A_{LED}}{A_{Inc}} \right), \qquad \textbf{Equation 94}$$

the photocurrent in region 2 can be expressed as

$$I_p = P \times R \times \left(\frac{A_{inc} - A_{over}}{A_{Inc}} \right), \qquad \textbf{Equation 95}$$

the photocurrent in region 3 can be expressed as

$$I_p = P \times R \times \left(\frac{A_{fd} - A_{over}}{A_{Inc}} \right), \qquad \textbf{Equation 96}$$

and the photocurrent in region 4 can be expressed as

$$I_p = P \times R \times \left(\frac{A_{fd}}{A_{Inc}} \right), \qquad \textbf{Equation 97}$$

where A_{fd} is the overlapping of the fiber core and detector and is given by,

$$A_{fd} = r_{MSM}^2 \theta_3 + r_{fiber}^2 \theta_5 - 2A_s - 2A_3 \qquad \textbf{Equation 98}$$

where r_{MSM} is the radius of the photodetector, r_{fiber} is the radius of the fiber core, θ_3 and θ_5 are the angles opposite of and adjacent to r_{fiber}, respectively, A_s is the area of the sector with central angle θ_3 that is not included in the overlapping area, and A_3 is the area of the

third triangle that is included in two sectors: the sector with radius r_{MSM} and central angle θ_3, and the sector with radius r_{fiber} and central angle θ_5, as shown in Figure 71.

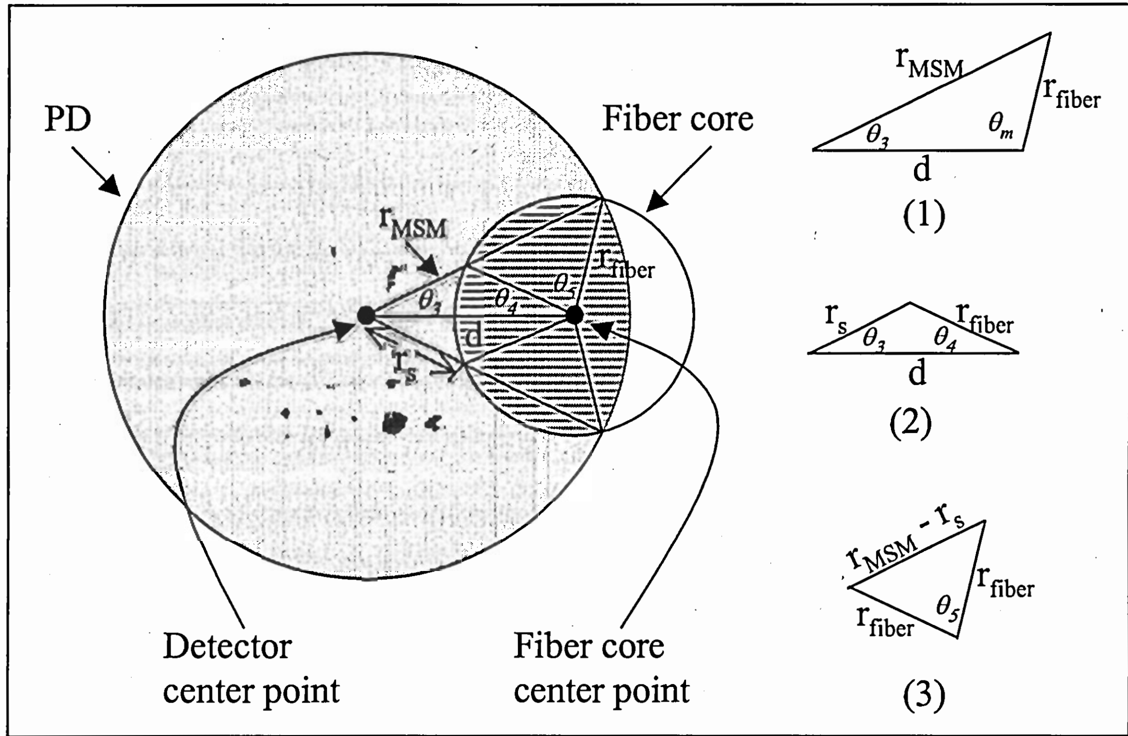

Figure 71: I-MSM PD lateral displacement in region 4.

Using the law of cosines, the angles in Figure 71 can be expressed as

$$\theta_3 = \cos^{-1}\left(\frac{r_{MSM}^2 - r_{fiber}^2 + d^2}{2dr_{MSM}}\right), \quad \textbf{Equation 99}$$

$$\theta_m = \cos^{-1}\left(\frac{r_{fiber}^2 - r_{MSM}^2 + d^2}{2dr_{fiber}}\right), \quad \textbf{Equation 100}$$

$$\theta_4 = \cos^{-1}\left(\frac{r_{fiber}^2 - r_s^2 + d^2}{2dr_{fiber}}\right), \quad \textbf{Equation 101}$$

and

$$\theta_5 = \theta_m - \theta_4 \quad \textbf{Equation 102}$$

where r_s can be derived using the law of cosines and expressed as

$$r_s = d\cos\theta_3 - \sqrt{d^2\cos^2\theta_3 - d^2 + r_{fiber}} \; . \qquad \textbf{Equation 103}$$

To calculate the area, A_s, the area of the sector with central angle θ_4 is subtracted from the area of triangle 2 and given as

$$A_s = \frac{1}{2}\left(dh_2 - r_{fiber}^2\theta_4\right) \qquad \textbf{Equation 104}$$

where d is the base and h_2 is the height of triangle 2.

The height h_2 can be expressed as

$$h_2 = \left(r_{fiber}^2 - \frac{\left(r_s^2 - r_{fiber}^2 - d^2\right)^2}{4d^2}\right)^{1/2} . \qquad \textbf{Equation 105}$$

The area A_3, can be expressed as

$$A_3 = \frac{1}{2}\left(r_{MSM} - r_s\right)h_3 \qquad \textbf{Equation 106}$$

where h_3 is the height of triangle 3 and can be expressed as

$$h_3 = \left(r_{fiber}^2 - \frac{\left(r_{MSM}^2 - r_s^2\right)^2}{4}\right)^{1/2} . \qquad \textbf{Equation 107}$$

Using these equations, a theoretical plot of the photocurrent as a function of lateral displacement is shown in Figure 72.

In conclusion, a theoretical model for calculating the integrated I-MSM PD photocurrent as a function of lateral displacement has been developed using geometrical optics. The model assumes that the power distribution of the light exiting the fiber is uniform. This assumption is valid for optical signals exiting multimode fibers after propagating long distances.

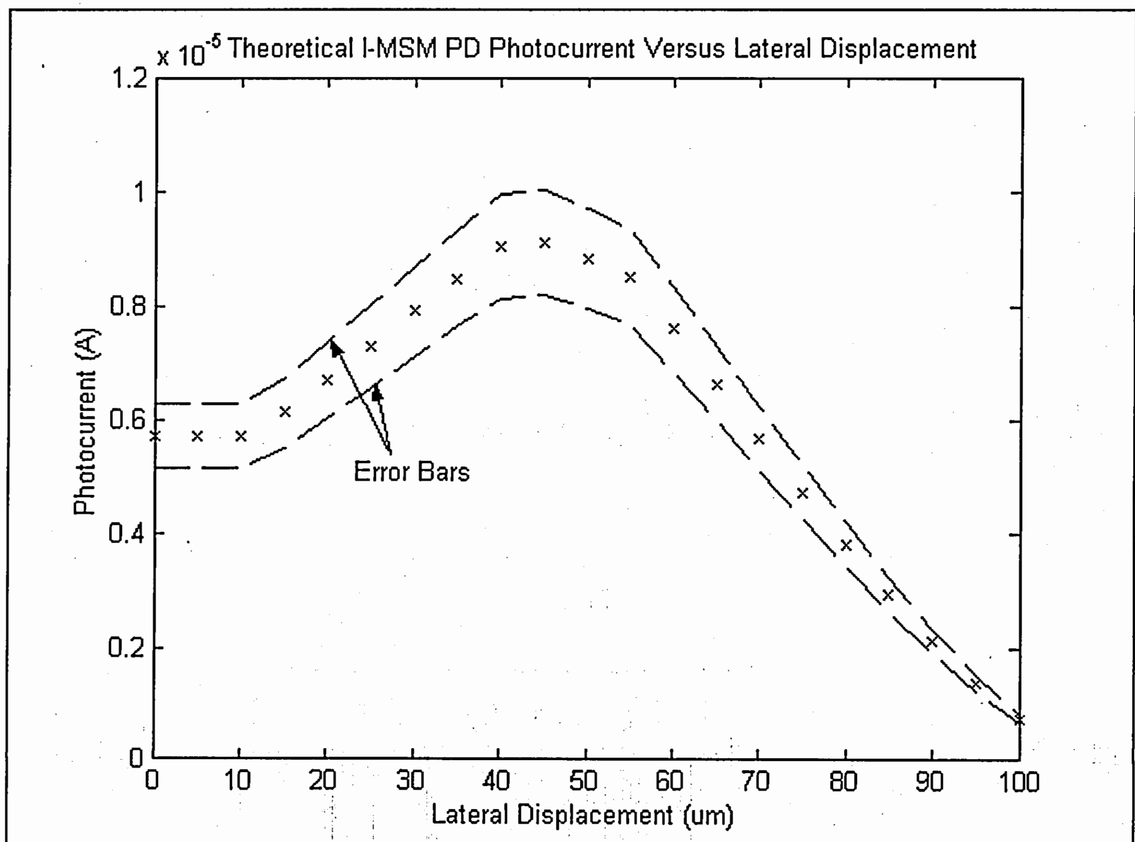

Figure 72: I-MSM PD photocurrent versus lateral displacement

CHAPTER 5

THEORY VERSUS EXPERIMENT

In this chapter, the theoretical models that were developed to predict the alignment tolerance of a 3D stacked emitter/detector device is compared to experimental results obtained from 3D stacked devices integrated on SiO_2-coated silicon substrates and silicon CMOS transceiver circuits. The I-MSM PD theoretical photocurrent as a function of longitudinal and lateral displacement is compared to measured results. In addition, the theoretical coupling efficiency as a function of longitudinal and lateral displacement between a step-index multimode fiber and an RCE LED is compared to measured results.

To measure the alignment tolerance of the 3D stacked thin-film emitter/detector, the device was mounted to a probe station with DC probes to provide the biasing of the individual devices. A lightwave fiber holder with a 62.5 μm core diameter step index multimode fiber with a numerical aperture of 0.22 was used to collect the optical signal to and from the stacked device. The positioner, which was used to translate the fiber, longitudinal displacement was approximately 407 μm per revolution. The Z-motion knob had a 12 μm minimum step size for the longitudinal displacement measurement. The lateral displacement was approximately 20 μm per step. To measure the photocurrent, a Hewlett Packard 8153A Lightwave Multimeter was used as a CW lightsource with λ = 1321-nm. A mode scrambler was inserted into the light path to make the fiber output more uniform. A source measurement unit (SMU) was used to reverse bias the I-MSM PDs and measure the photocurrents. An additional SMU was used to forward bias the RCE LEDs. The optical power from the RCE LEDs was measured using a Hewlett Packard 8153A Lightwave Multimeter.

The first comparison was between the theoretical photocurrent and the measured photocurrent as a function of longitudinal displacement of a GaAs RCE LED/InGaAs I-MSM PD 3D stacked device integrated onto a SiN_x-coated silicon substrate. The RCE LED had a 50 μm diameter and the I-MSM PD had a 200 μm diameter. In the case of the 3D stacked I-MSM PD alignment tolerance test, the main assumption made was that the power distribution out of the fiber was uniform. Normally, the output power distribution is speckled, which makes it difficult to model. To increase the uniformity of the fiber output, a mode scrambler was used. To illustrate the effect of the mode scrambler, the relative output power distribution of the fiber was captured with and without a mode scrambler using an infrared imaging system. The pictures are shown in Figure 73.

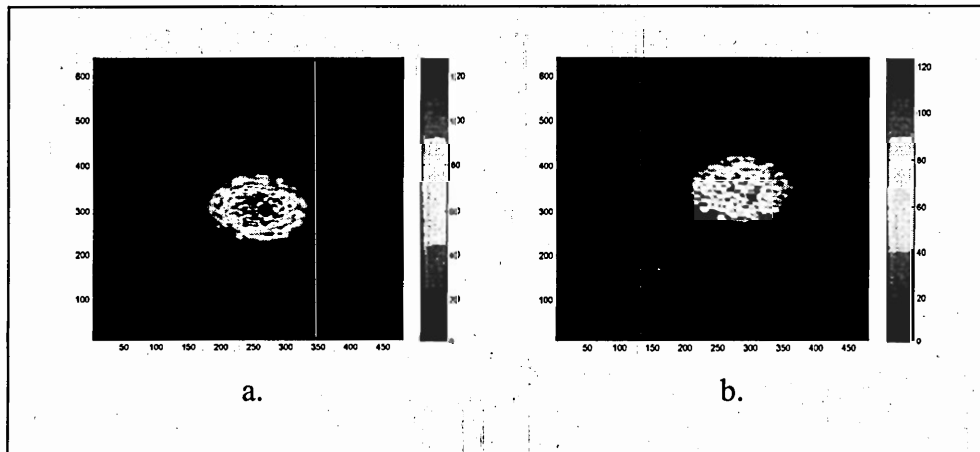

Figure 73: Fiber output a) without mode scrambler and b) with mode scrambler

Using the mode scrambler makes the fiber output more uniform in intensity, and, using a theoretical model, which assumes uniform fiber output, the theoretical photocurrent of the integrated I-MSM in the I-MSM PD/LED stack is shown in Figure 43, which agrees well with the experimental measurements for longitudinal displacements larger than 100 μm. The maximum responsivity of the I-MSM in the integrated I-MSM/PD stack was

0.31 A/W, which was as predicted, 88% of the responsivity of an I-MSM PD without an LED integrated in the center.

The second comparison was between the theoretical photocurrent and the measured photocurrent as a function of longitudinal displacement of a GaAs RCE LED/InGaAs I-MSM PD 3D stacked device integrated onto a silicon CMOS circuit. The RCE LED had a 50 μm diameter and the I-MSM PD had a 150 μm diameter. The result of the longitudinal alignment tolerance testing is shown in Figure 74. Theory and experiment match well with in the limitations of measurement and theoretical error. Sources of error for this test include the translation stage tolerance, fiber core size and numerical aperture accuracy, SMU precision, and optical output uniformity. Even with the mode scrambler as can be seen from Figure 73, a higher power density appears to exist in the center of the optical input signal, resulting in a lower photogenerated current, when the fiber core is overlapping the LED. To account for the power distribution nonuniformity in the theoretical model, the apparent radius of the LED was set to 20% more than its actual length of 25 μm. With 200 μm diameter PD mesas, the detector fill point at 300 μm matches well with the theoretical calculation. Since power is not completely uniform, the photocurrent does not drop off as fast from overfilling.

The result of the stacked I-MSM PD lateral alignment tolerance is shown in Figure 75. The longitudinal displacement is approximately 16 μm. In region 1, before the fiber core illumination intersects the LED, the photocurrent is constant. As predicted in region 2, the photocurrent increases until the fiber core intersects the detector. Then, the photocurrent drops off as the P is overfilled. Once again, if there is more power in he

center of the optical input distribution, the photocurrent does not drop off as fast as in the uniform power distribution theoretical case.

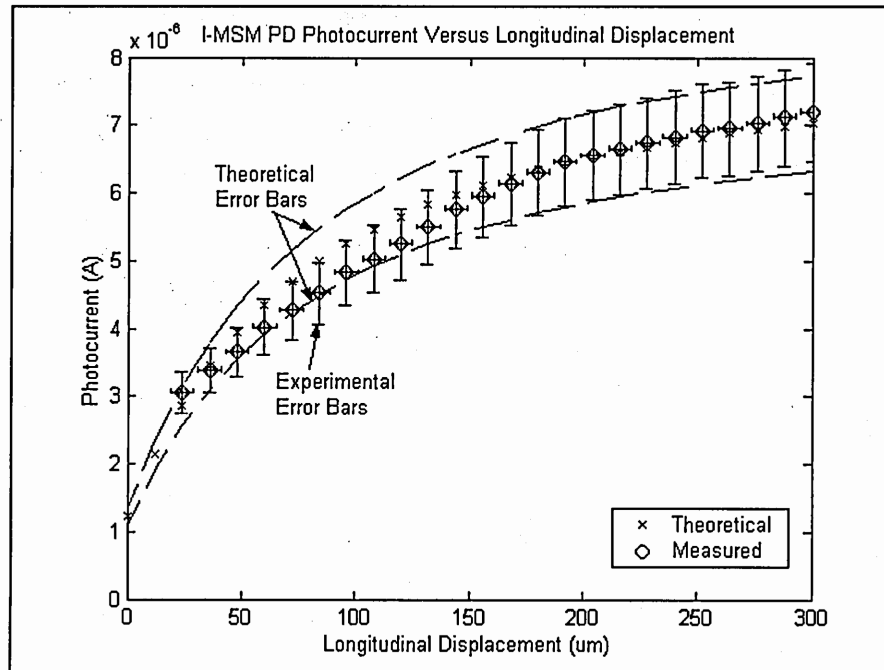

Figure 74: I-MSM PD longitudinal theory versus experiment

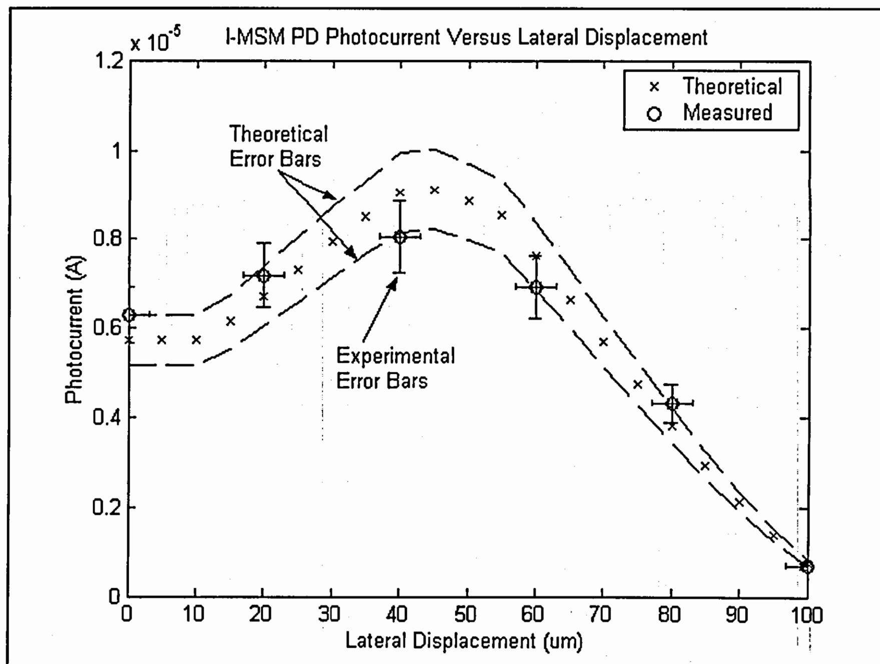

Figure 75: I-MSM PD lateral theory versus experiment

The theoretical coupling efficiency of an LED and a step index multimode fiber as a function of longitudinal displacement was compared to measured data from an LED integrated onto a silicon CMOS circuit. The results are shown in Figure 76. The measured data agrees well with the theoretical calculations. The RCE LED was assumed to be Lambertian in the theoretical analysis, which is a good assumption for surface emitting LEDs. However, the divergence angle of an RCE LED is smaller than the divergence angle of a surface emitting LED without mirrors.

The result from the LED lateral displacement test is shown in Figure 77. The measured data agrees well with that of the theoretical calculation. All of the data fit within the 10% error bars, which was set by the tolerance of the translation stage, fiber core, and the beam profile of the LED. Finally, the optimal longitudinal displacement results for the theoretical and measured case are shown in Figure 78. The optimal displacement in each case was approximately 125-μm.

In conclusion, the theory derived in chapter 4 to predict the alignment tolerance of 3D stacked thin film emitter/detector devices has been compared to experimental results. Data from devices integrated onto SiO_2-coated silicon substrates and silicon CMOS circuits have been compared to theory. The results from longitudinal and lateral displacement test agree well with the theoretical calculations.

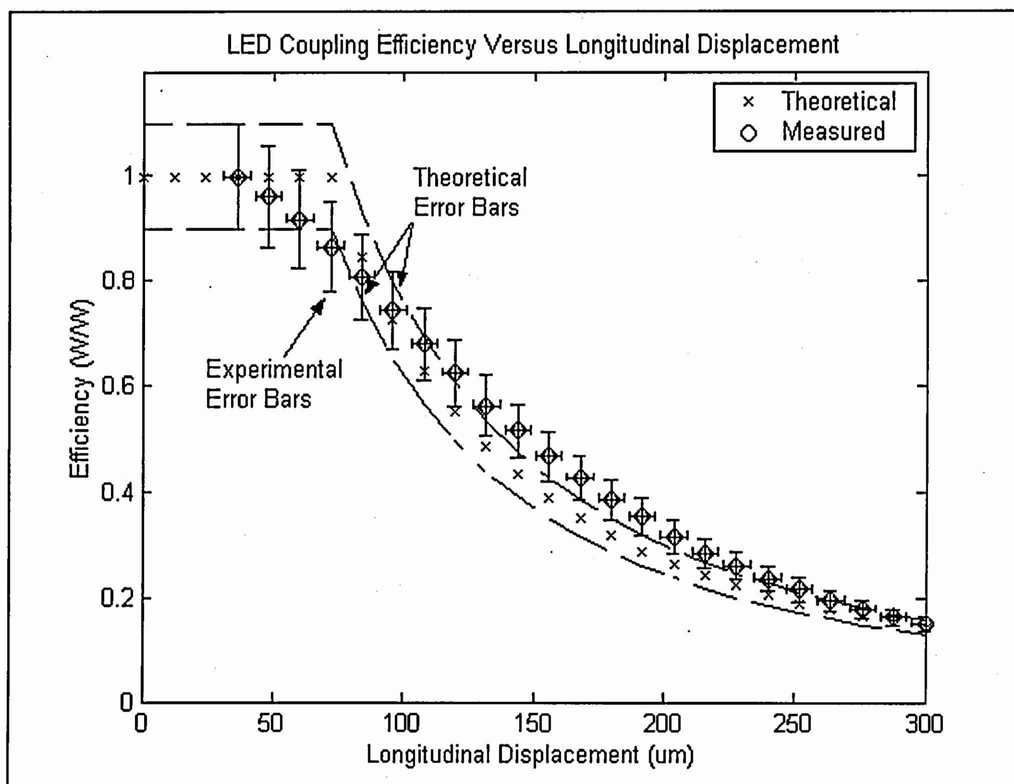

Figure 76: LED longitudinal theory versus experiment.

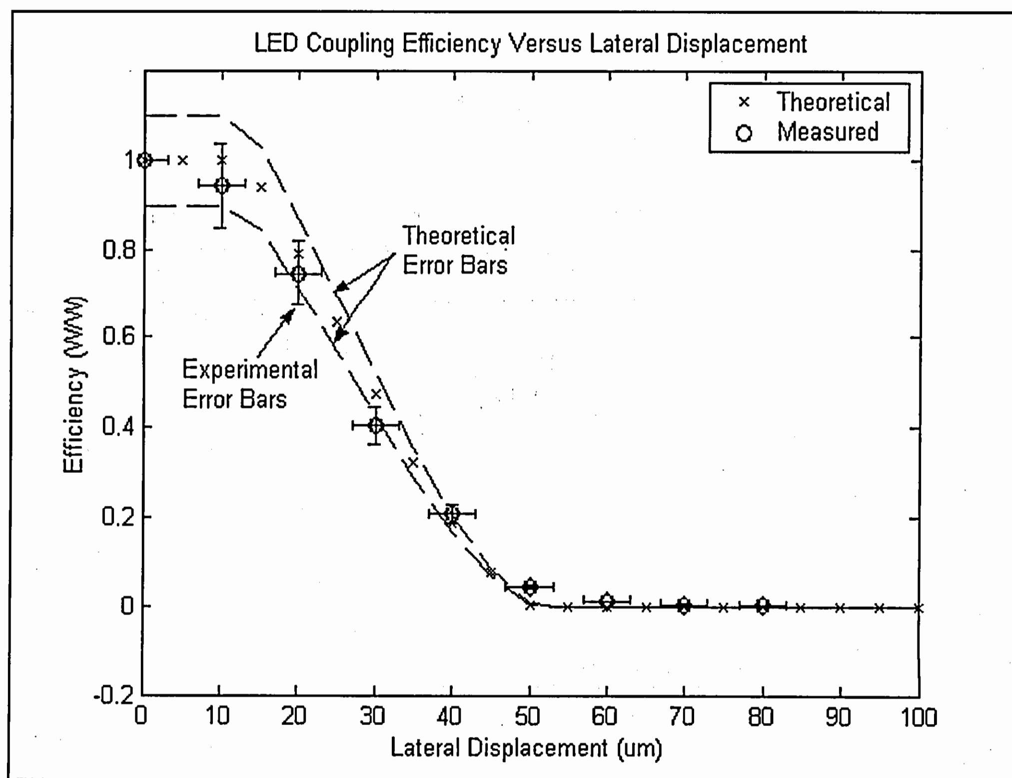

Figure 77: LED lateral theory versus experiment

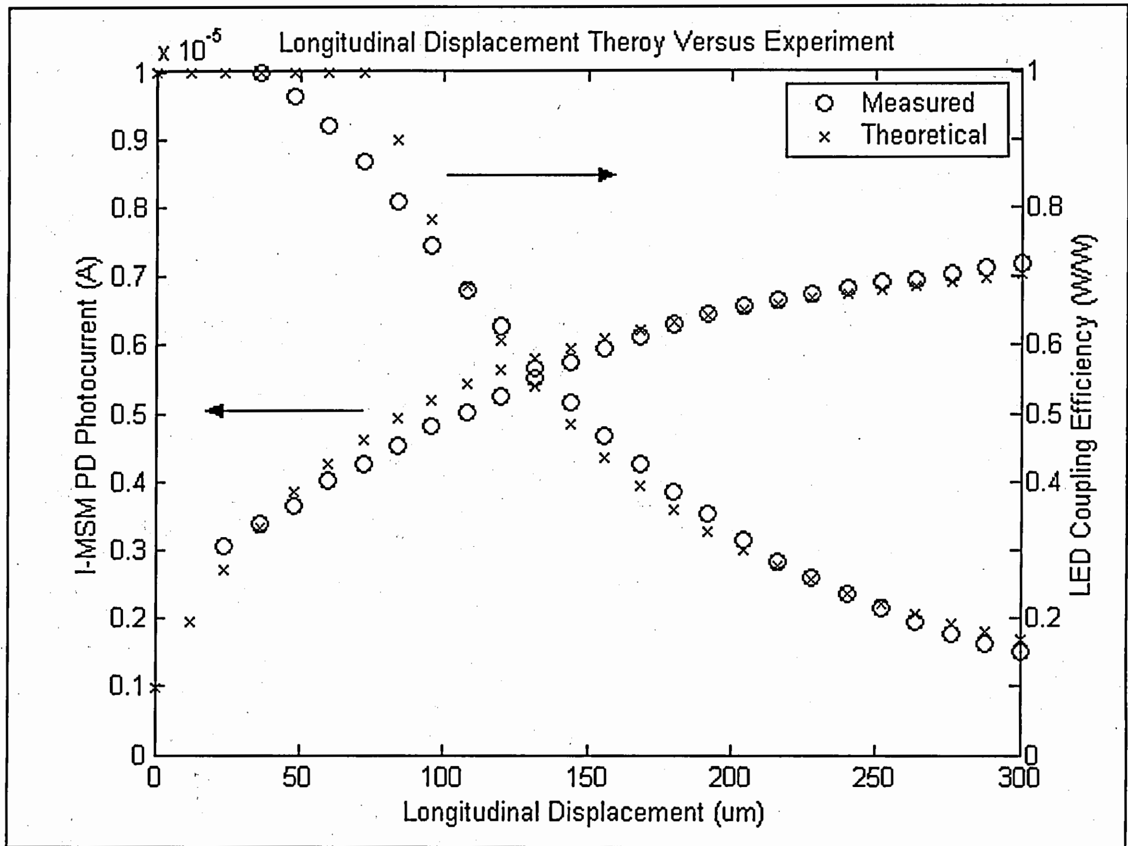

Figure 78: Longitudinal theory versus experiment

CHAPTER 6

CONCLUSION AND RECOMMENDATIONS

This dissertation has demonstrated the ability to build 3D stacked bi-directional single fiber optoelectronic transceivers. The heterogeneous integration approach used in this research illustrated the ability to independently design, optimize, and fabricate each component in an optical transceiver, then for the emitter and detector, separate them from their growth substrate, and stack them in a 3D format to provide a bi-directional single fiber transceiver. This capability was highlighted by the fabrication of different size and shaped 3D stacked devices integrated onto silicon. Also demonstrated was the ability to mix and match material systems without concern for lattice mismatch by the fabrication of a 3D stacked GaAs RCE LED/InGaAs I-MSM PD device. In addition, the 3D stacked device was integrated onto a silicon CMOS transceiver circuit to show that not only can the photonics be independently optimized, but integrated with separately optimized circuitry, as well. Finally, theoretical calculations of alignment tolerance matched well to the experiment results. The –3 dB point for the coupling efficiency of the RCE LED occurs at a longitudinal displacement of approximately 125 μm, which is the optimal position for the 3D stacked emitter/detector device. However, in the case of lateral displacement, the –3 dB point for the coupling efficiency occurs at approximately 25 μm. When compared to the bi-functional devices presented in chapter 2, this alignment tolerance is equal to the bi-functional LEDs of similar sizes and more tolerant than the VCSELs and edge-emitting lasers due to the directionality of the laser sources. The photonic integrated circuits were coupled into single mode fiber and had a 1-dB loss with

2.2 μm of longitudinal displacement and 3.2 μm of lateral displacement [12]. The results of this dissertation is important because it gives commercial and government sectors the ability to build a low cost and high-speed optoelectronic transceiver that can be employed in bi-directional single fiber optical links for fiber-to-the-curb/home/building/desktop (FTTX) and in military and aerospace fiber link (MAFA) applications. As the demand for FTTX and MAFA continue to increase, there will be an increasing demand for affordable optical network units (ONUs). The main component of ONUs is the optoelectronic transceiver, and the cost of the ONUs is critical.

To improve upon the work that has been done for this thesis, other emitters such as VCSELs could be used for higher speed emission. In addition, the order and position in which the devices are stacked could be investigated in an effort to improve the alignment tolerance and speed of the system. Moreover, to improve the directionality of the LED a lens could be integrated on top of the LED. Finally, to make the 3D stack more manufacturable, organic thin-film devices could be studied

REFERENCE

[1] G. Kramer and G. Pesavento, "Ethernet Passive Optical Network (EPON): Building a Next-Generation Optical Access Network," IEEE Communications Magazine, 2002, vol. 40, no.2. pp. 66-73.

[2] D. Kettler, H. Kafka, and D. Spears, "Driving Fiber to the Home," IEEE Communications Magazine, 2000, vol.38, no. 11, pp. 106-110.

[3] T. Shan, J. Yang, and, C. Sheng, "EPON UpstreamMultiple Access Scheme," Proceedings. ICII 2001 - Beijing. 2001 International Conferences, vol. 2, 2001 pp. 273 –278.

[4] A. Tan, "Super PON-A Fiber to the Home Cable Network for CATV and POTS/ISDN/VOD as Economical as a Coaxial Cable Network," J. Lightwave Technol., 1997, vol. 15, no. 2, pp. 213-218.

[5] D. Horwitz, "COTS Fiber Optic Applications in Military and Aerospace," Optical Fiber Communication Conference, 2000 , vol.4, pp. 12 –14.

[6] D. Horwitz, "C.O.T.S. Fiber Optic Interconnect Solutions for Mobile Platforms," Electronic Components and Technology, 1998, pp. 395-403.

[7] B.S. Kawasaki, K.O. Hill, D.C. Johnson, and A.U. Tenne-Sens, "Full duplex transmission link over single-strand optical fiber," Opt. Lett., 1977, vol. 1, no. 3, pp.107-108.

[8] T. Ozeki, T. Uematsu, T. Ito, M. Yamamoto, and Y. Unno, "Half-duplex optical transmission link using an LED source-detector scheme," Opt. Lett., 1978, vol. 2, no. 4, pp.103-105.

[9] A. Alping and R. Tell, "100Mb/s Semiduplex Optical Fiber Transmission Experiment Using GaAs/GaAlAs Laser Transceivers," J. Lightwave Technol., 1984, vol. 2, no. 5, pp. 663-667.

[10] M. Dragas, I. White, R. Penty, J. Rorison, P. Heard, and G. Parry, "Dual-Purpose VCSEL's for Short-Haul Bi-directional Communication Links," IEEE Photon. Technol. Lett., 1999, vol. 11, no. 12, pp. 1548-1550.

[11] M. Takeuchi, F. Satoh, and S. Yamashita, "A New Structure GaAlAs-GaAs Device Uniting LED and Phototransistor," Jpn. J. Appl. Phys., 1982, vol. 21, no. 12, pp. 1785

[12] R. Ben –Michael, U. Koren, B. Miller, M. Young, T. Koch, M. Chien, R. Capik,

G. Raybon, and K. Dreyer, "A Bi-directional Transceiver PIC for Ping-Pong Local Loop Configurations Operating at 1.3-μm Wavelength," IEEE Photon. Technol. Lett., 1995, vol. 7, no. 12, pp. 1424-1426.

[13] K. Liou, B. Glance, U. Koren, E. Burrows, G. Raybon, C. Burrus, and K. Dreyer, "Monolithically Integrated Semiconductor LED-Amplifier for Applications as Transceivers in Fiber Access Systems," IEEE Photonics Technol. Lett. 1996,vol. 8, no. 6, pp. 800-802.

[14] J.Cross, A. Lopez-Lagunas, B. Buchanan, L. Carastro, S. Wang, N. Jokerst, S.Wills, M. Brooke, and M. Ingram, "A Single-Fiber Bidirectional Optical Link Using Colocated Emitters and Detectors," IEEE Photon. Technol. Lett., 1996, vol. 8, no.10, pp. 1385-1387.

[15] P. Bhattacharya, Semiconductor Optoelectronic Devices. Upper Saddle River, NJ: Prentice Hall.,1997.

[16] J. Geddes, P. Petersen, D. Chen, K. Koeneman, "Semiconductor Junction Transceiver For Fibre Optic Communication," Electronics Letters, 1978, vol. 14, no.7, pp. 214-216.

[17] W. Hubbard and H. Kkehlenbeck, "Light-Emitting Diodes (L.E.D.S) As Receivers with Avalanche Gain," Electronics Letters, 1978, vol. 14, no. 17, pp. 553-554.

[18] J.T. Verdeyen, Laser Electronics. Englewood Cliffs, NJ: Prentice Hall, 1995

[19] B.G. Streetman, Solid State Electronic Devices. Upper Saddle River, NJ: Prentice Hall, 1995.

[20] J. Singh, Semiconductor Devices: Basic Principles. New York: John Wiley & Sons, 2001.

[21] K. F. Brennan, The Physics of Semiconductors with applications to Optoelectronic Devices. New York: Cambridge University Press, 1999.

[22] G. Keiser, Optical Fiber Communications. New York: McGraw-Hill, 1991.

[23] R.J. Hoss, Fiber Optic Communications: Design Handbook. Englewood Cliffs, NJ: Prentice Hall, 1990.

[24] F.C. Allard, Fiber Optics Handbook for Engineers and Scientists. New York: McGraw-Hill, 1990.

[25] R.M. Gagliardi and S. Karp, Optical Communications. New York: John Wiley & Sons, 1995.

[26] R.J Hoss and E. A. Lacy, Fiber Optics. Englewood Cliffs, NJ: Prentice Hall, 1993.

[27] H.B. Killen, Fiber Optic Communications. Englewood Cliffs, NJ: Prentice Hall, 1991.

[28] K. Tai, R.J. Fischer, C.W. Seabury, N. A. Olsson, T-C.D. Huo, Y. Ota, and A.Y. Cho, "Room-temperature continuous-wave vertical –cavity surface-emitting GaAs injection lasers," Appl. Phys. Lett., 1989, vol. 55, no. 24, pp. 2473-2475.

[29] T. Sakaguchi, F. Koyama, and K. Iga, "Vertical Cavity Surface-Emitting Laser with an AlGaAs/AlAs Bragg Reflector," Electronics Letters, 1988, vol. 24, no. 15, pp. 928-929.

[30] E.F. Schubert, Y. -H. Wang, A.Y Cho, L. -W. Tu, and G.J. Zydzik, "Resonant cavity light emitting diode," Appl. Phys. Lett., 1992, vol. 60, no. 8, pp. 921-923.

[31] S. T. Wilkinson, N. M. Jokerst, and R.P. Leavitt, "Resonant-cavity-enhanced thin-film AlGaAs/GaAs/AlGaAs LED's with metal mirrors," Applied Optics, 1995, vol. 34, no. 36, pp. 8298-8302.

[32] B. Corbett, L. Considine, S. Walsh, and W. Kelly, "Resonant Cavity Light Emitting Diode and Detector Using Epitaxial Liftoff," IEEE Photon. Technol. Lett, 1993, vol. 5, no. 9, pp. 1041-1043.

[33] T.J. Rogers, D.G. Deppe, and B.G. Streetman, "Effect of an AlAs/GaAs mirror on the spontaneous emission of an InGaAs-GaAs quantum well," Appl. Phys. Lett., 1990, vol. 57, no. 18, pp. 1858-1860.

[34] N.E.J. Hunt, E.F. Schubert, R.F. Kopf, D.L. Sivco, A.Y. Cho, and G.J. Zydzik, "Increase fiber communication bandwidth from a resonant cavity light emitting diode emitting at λ=940 nm," Appl. Phys. Lett., 1993, vol. 63, no. 19, pp. 2600-2602.

[35] V. Diadiuk and S.H. Groves, "Double-Heterostructure InGaAs/InP PIN Photodetectors," Solid-State Electronics, 1986, vol. 29, no. 2, pp. 229-233.

[36] G. Hasnain, K. Tai, Y.H. Wang, J.D. Wynn, K.D. Choquette, B.E. Weir, N.K. Dutta, and A.Y. Cho, " Monolithic Integration of Photodetector with Vertical Cavity Surface Emitting Laser," Electronics Letters, 1991, vol. 27, no. 18, pp. 1630-1632.

[37] A.C. Alduino, S.Q. Luong, Y. Zhou, C.P. Hains, and J. Cheng, "Quasi-Planar Monolithic Integration of High-Speed VCSEL and Resonant Enhanced Photodetector Arrays," IEEE Photon. Technol. Lett., 1999, vol. 11, no. 5, pp. 512-514.

[38] M.A. Matin, K.C. Song, B.J. Robinson, J.G. Simmons, D.A. Thompson, and F. Gouin, "Very low dark current InGaP/GaAs MSM-photodetector using semi-transparent and opaque contacts," Electronics Letters, 1996, vol. 32, no. 8, pp. 766-767.

[39] S. Matsuo, T. Nakahara, K. Tateno, and T. Kurokawa, "Novel Technology for Hybrid Integration of Photonic and Electronic Circuits," IEEE Photon. Technol. Lett., 1996, vol. 8, no. 11, pp. 1507-1509.

[40] N.M. Jokerst, M.A. Brooke, O. Vendier, S. Wilkinson, S. Fike, M. Lee, E. Twyford, J. Cross, B. Buchanan, and S. Wills, "Thin-Film Multimaterial Optoelectronic Integrated Circuits," IEEE Trans. Components, Packaging, and Manufacturing Technol. Part B, 1996, vol. 19, no.1, pp. 97-106.

[41] N.M. Jokerst, "Hybrid Integrated Optoelectronics: Thin Film Devices Bonded to Host Substrates," Intl. J. High Speed Electron. Sys., 1997, vol.8, no. 2, pp. 325-356.

[42] E. Yablonovitch, T. Gmitter, J.P. Harbison, and R. Bhat, "Extreme selectivity in the lift-off of epitaxial GaAs films," Appl. Phys. Lett., 1987, vol. 51, no. 26, pp. 2222-2224.

[43] M. Ikeda, Y. Murakami, and K. Kitayama, "Mode scrambler for optical fibers," Applied Optics, 1977, vol. 16, no. 4, pp. 1045-1049.

[44] M. Imai and T. Asakura, "Evaluation of the Mode Scrambler Characteristics in Terms of the Speckle Contrast," Optics Communications, 1979, vol. 30, no. 3, 299-303

[45] A. Agarwal and U. Unrau, "Comparative Study of Methods to Produce Stationary Mode Power Distribution for Optical Fiber Measurements," J. Opt. Commun., 1983, vol. 4, pp. 126-133.

[46] C. Camperi-Ginestet, M. Hargis, N.M. Jokerst, and M. Allen, "Alignable epitaxial liftoff of GaAs materials with selective deposition using polyimide diaphragms," IEEE Photon. Technol. Lett., 1991, vol. 3, pp. 1123-1126.

[47] E. Philofsky and E. Hall, "A review of the Limitations of Aluminum Thin Films on Semiconductor Devices," IEEE Trans. On Parts, Hybrids, and Packaging, 1975, vol.11, no.4, pp. 281-290.

[48] J. Barnard, H. Ohno, C. Wood, and L. Eastman, "Double Heterostructure $Ga_{0.47}In_{0.53}As$ MESFETs with Submicron Gates," IEEE Electron Device Letters, 1980, vol. EDL-1, no. 9, pp. 174-176.

[49] M. Ito and O. Wada, "Low Dark Current GaAs Metal-Semiconductor-Metal (MSM) Photodiodes using Wsi_x contacts," J. Quantum Electron., 1986, vol. 22, no. 7, pp. 1073-1077.

[50] O. Vendier, N.M. Jokerst, and R.P. Leavitt, "High efficiency thin-film GaAs-based MSM photodetectors," Electronics Letters, 1996, vol. 32, no. 4, pp. 394-395.

[51] S.C. Wang, J. Cross, S.M. Chai, A. Lopez, J. Park, M.A. Ingram, N.M. Jokerst, D.S. Wills, M.A. Brooke, and A. Brown, "Coupling Efficiency of an Alignment-Tolerant, Single Fiber, Bi-directional Link," Electronic Components and Technology Conference, 1997, pp. 30-36.

[52] R. Bockstaele, C. Sys, J. Blondelle, B. Dhoedt, I. Moerman, P.V. Daele, P. Demeester, and R. Baets, " Resonant Cavity LED's Optimized for Coupling to Polymer Optical Fiber," IEEE Photon. Technol. Lett., 1999, vol. 11, no.2, pp. 158-160.

[53] F.L. Pedrotti and L.S. Pedrotti, Introduction to Optics. Englewood Cliffs, NJ: Prentice Hall, 1993.

[54] K. Streubel and R. Stevens, "250Mbit/s plastic fiber transmission using 660nm resonant cavity light emitting diode," Electronics Letters, 1998, vol. 34, no. 19, pp. 1862-1863.

[55] D. Delbeke, R. Bockstaele, P. Bienstman, R. Baets, and H. Benisty, "High-Efficiency Semiconductor Resonant-Cavity Light-Emitting Diodes: A Review," IEEE J. Select. Topics Quantum Electron., 2002, vol. 8, no. 2, pp. 189-206.

[56] R. Bockstaele, T. Coosemans, C. Sys, L. Vanwassenhove, A.V. Hove, B. Dhoedt, I. Moerman, P.V. Daele, R.G. Baets, R. Annen, H. Melchior, J. Hall, P.L. Heremans, M. Brunfaut, and J.V. Campenhout, "Realization and Characterization of 8 x 8 Resonant Cavity LED Arrays Mounted onto CMOS Drivers for POF-Based Interchip Interconnections," IEEE J. Select. Topics Quantum Electron., 1999, vol. 5, no. 2, pp. 224-235.

[57] A. Sarto and B. Zeghbroeck, "Photocurrent in a Metal-Semiconductor-Metal Photodetector," IEEE J. Quantum Electron., 1991, vol. 33, no. 12, pp. 2188-2194.

[58] S.M. Sze, D.J. Coleman, and A. Loya, "Current Transport in Metal-Semiconductor-Metal Structures," Solid State Electronics, 1971, vol. 14, pp. 1209-1218.

[59] J. Soole and H. Schumacher, "Transit-Time Limited Frequency Response of InGaAs MSM Photodetectors," IEEE Tran. Electron Devices, 1990, vol. 37, no. 11, pp. 2285-2290.

[60] J. Soole and H. Schumacher, "InGaAs Metal-Semiconductor-Metal Photodetectors for Long Wavelength Optical Communications," IEEE J. Quantum Electron., 1991, vol. 27, no. 3, pp. 737-752.

[61] W. C. Koscielniak, J. Pelouard, R. Kolbas, and M. Littlejohn, "Dark Current Characteristics of GaAs Metal-Semiconductor-Metal (MSM) Photodetectors," IEEE Trans. Electron Devices, 1990, vol. 37, no. 7, pp. 1623-1628.

[62] J. Burm, K. Litvin, W. Schaff, and L. Eastman, "Optimization of High-Speed Metal-Semiconductor-Metal Photodetectors," IEEE Photonics Technol. Lett., 1994, vol. 6, no. 6, pp. 722-724.

[63] J. H. Kim, H.T. Griem, R. A. Friedman, E. Y. Chan, and S. Ray, "High Performance Back-Illuminated InGaAs/InAlAs MSM Photodetector with a Record Responsivity of 0.96 A/W," IEEE Photonics Technol. Lett., 1992, vol. 4, no. 11, pp. 1241-1244.

[64] D.L. Rogers, "Integrated Optical Receivers using MSM Detectors," J. Lightwave Technol., 1991, vol. 9, no. 12, pp. 1635-1638.

[65] O. Wada, H. Nobuhara, H. Hamaguchi, T. Mikawa, A. Tackeuchi, and T. Fujii, "Very high speed GaInAs metal-semiconductor-metal photodiode incorporating an AlInAs/GaInAs graded superlattice," Appl. Phys. Lett., 1989, vol. 54, no. 1, pp. 16-17.

[66] M.V. Rao, S.M. Gulwadi, W. -P. Hong, C. Caneau, G.K. Chang, and N. Papanicolaou, "Metal-Semiconductor-Metal Photodetector Using Fe-Implanted $In_{0.53}Ga_{0.47}As$," Electronics Letters, 1992, vol. 28, no. 1, pp. 46-47.

[67] W.P. Hong, G.K. Chang, R. Bhat, J.L. Gimlett, C.K. Nguyen, G. Sasaki, and M. Koza, "High-Performance $Al_{0.48}In_{0.52}As/Ga_{0.47}In_{0.53}As$ MSM-HEMT Receiver OEIC Grown by MOCVD on Patterned InP Substrates," Electronics Letters, 1989, vol. 25, no. 23, pp. 1561-1563.

[68] R.H. Yuang and J.I Chyi, "Effects of finger Width on large-area InGaAs MSM Photodetectors," Electronics Letters, 1996, vol. 32, no.2, pp. 131-132.

[69] Y.C. Lim and R.A. Moore, "Properties of Alternatively Charged Coplanar Parallel Strips by Conformal Mapping," IEEE Trans. Electron Devices, 1968, vol. 15, no. 3, pp. 173-180.

[70] F. Hieronymi, E.H. Böttcher, E. Dröge, D. Kuhl, St. Kollakowski, and D. Bimberg, "Large-area low –capacitance InP/InGaAs MSM Photodetectors for high-speed operation under front and rear illumination," Electronics Letters, 1994, vol. 30, no. 15, pp. 1247-1248.

[71] W. Hilberg, "From Approximations to Exact Relations of Characteristic Impedances," IEEE Trans. on Microwave Theory and Techniques, 1969, vol. MTT-17, no. 5, pp. 259-265.

[72] J. W. Seo, A. A. Ketterson, D. G. Ballegeer, K.Y. Cheng, I. Adesida, X. Li, and T. Gessert, "A Comparative Study of Metal-Semiconductor-Metal Photodetectors on GaAs with Indium-Tin-Oxide and Ti/Au electrodes," IEEE Photonics Technol. Lett., 1992, vol. 4, no. 8, pp. 888-890.

[73] P. Fay, W. Wohlmuth, A. Mahajan, C. Caneau, S. Chandrasekhar, and I. Adesida, "A Comparative Study of Integrated Photoreceivers Using MSM/HEMT and PIN/HEMT Technologies," IEEE Photonics Technol. Lett., 1998, vol. 10, no. 4, pp. 582-584.

[74] J.B. Kim, M.J. Kim, S.J. Kim, W.Y. Hwang, D.L. Miller, M.B. Das, J. M. Rios, L.M. Lunardi, "Large area InAlAs/InGaAs metal semiconductor metal photodiode with very low dark current and its frequency response," Optical and Quantum Electronics, 1997, vol. 29, 953-959.

[75] M. Makiuchi, H. Hamaguchi, T. Kumai, O. Aoki, Y. Oikawa, and O. Wada, "GaInAs *pin* Photoreceiver for Gigabit-rate Communications using Flip-chip Bonding Techniques," Electronics Letters, 1988, vol. 24, no. 16, pp. 995-996.

[76] M. Conti, G. Corda, and M. De Padova, "PIN Photodetector Under Transient Conditions: Simulation and Experiments," Solid-State Electronics, 1979, vol. 22, pp. 151-155.

[77] R.P. Bryan, W.S. Fu, and G. R. Olbright, "Hybrid Integration of bipolar transistors and microlasers: Current-controlled microlaser smart pixels," Appl. Phys. Lett., 1993, vol.62, no.11, pp. 1230-1232.

[78] G.G. Ortiz, C.P. Hains, J. Cheng, H.Q. Hou, J.C. Zolper, "Monolithic Integration of $In_{0.2}Ga_{0.8}As$ Vertical-Cavity Surface Emitting Lasers with Resonance-Enhanced Quantum-Well Photodetector," Electronics Letters, 1996, vol. 32, no. 13, pp. 1205-1207.

[79] D.L. Mathine, R. Droopad, and G.N. Maracas, "A Vertical-Cavity Surface-Emitting Laser Appliquéd to a 0.8-μm NMOS Driver," IEEE Photon. Technol. Lett., 1997, vol. 9, no. 7, pp. 869-871.

[80] T. Nakahara, H. Tsuda, K. Tateno, S. Matsuo, and T. Kurokawa, "Hybrid Integration of Smart Pixels by Using Polyimide Bonding: Demonstration of GaAs p-I-n Photodiode/CMOS Receiver," IEEE J. Select. Topics Quantum Electron., 1999, vol. 5, no. 2, pp. 209-216.

[81] R. Pu, C. Duan, and C. Wilmsen, "Hybrid Integration of VCSEL's to CMOS Integrated Circuits," IEEE J. Select. Topics Quantum Electron., 1999, vol. 5, no. 2, pp. 201-208.

[82] D.L. Mathine, "The Integration of III-V Optoelectronics with Silicon Circuitry," IEEE J. Select. Topics Quantum Electron., 1997, vol. 3, no. 3, pp. 952-959.

[83] E. Yablonovitch, D.M. Hwang, T.J. Gmitter, L.T. Florez, and J.P. Harbison, "Van der Wall bonding of GaAs epitaxial liftoff films onto arbitrary substrates," Appl. Phys. Lett., 1990, vol. 56, no. 24, pp. 2419-2421.

[84] P. Demeester, I. Pollentier, P. Dobbelaere, C. Brys, and P. Daele, "Epitaxial lift-off and its applications," Semicond. Sci. Technol., 1993, vol. 8, pp. 1124-1135.

[85] J.J. Talghader, J.K. Tu, and J.S. Smith, "Integration Fludically Self-Assembled Optoelectronic Devices Using a Silicon Based Process," IEEE Photonics Technol. Lett., 1995, vol. 7, no. 11, pp. 1321-1323.

[86] J.K. Tu, J.J Talghader, M.A. Hadley, and J.S. Smith, "Fluidic self-assembly of InGaAs vertical cavity surface emitting lasers onto silicon," Electronics Letters, 1995, vol. 31, no. 17, pp. 1448-1449.

[87] J.J. Talghader, "Integration of LEDs and VCSELS using Fludic Self Assembly," SPIE, 1998, vol. 3286, pp. 86-95.

[88] W.A. Wohlmuth, M. Arafa, A. Mahajan, P. Fay, and I. Adesida, "InGaAs metal-semiconductor-metal photodetectors with engineered Schottky barrier heights," Appl. Phys. Lett., 1996, vol. 69, no. 23, pp. 3578-3580.

[89] J.J. Chang, CMOS Differential Analog Optical Receivers with Hybrid Integrated I-MSM Detector, Ph.D. Thesis, June 2000.

[90] S.Y. Jung, A High dI/dt CMOS Differential Optical Transmitter for a Laser Diode, Ph.D. Thesis, March 2002.

[91] Discussion with Dr. Martin Brooke, June 2003.

[92] K.H. Yang and J.D. Kingsley, "Calculation of Coupling Losses Between Light Emitting Diodes and Low-Loss Optical Fibers," Applied Optics, 1975, vol. 14, no. 2, pp. 288-293.

[93] A.K. Dutta, "Prospects of Highly Efficient AlGaInP Based Surface Emitting Type Ring-LED for 50 and 156 Mb/s POF Data Link Systems," J. Lightwave Technol., 1998, vol. 16, no. 1, pp. 106-113.

[94] H. Anton, Calculus: with Analytic Geometry. New York: John Wiley & Sons, 1992.

[95] R. Larson, R. Hostetler, and B. Edwards, College Algebra: A Graphing Approach. Boston, MA: Houghton Mifflin Company, 2001.

[96] J. Stewart, L. Redlin, and S. Watson, Precalculus: Mathematics for Calculus. Pacific Grove, CA: Brooks/Cole Publishing Company, 1998.

[97] S.T. Wilkinson, Resonant Cavity Photonic Devices For Optical Interconnects, Ph.D. Thesis, August 1996.